

Dynamic response phenotypes and model discrimination in systems and synthetic biology

Eduardo D. Sontag
Northeastern University

Abstract

Many biological systems encode function not primarily in steady states, but in the structure of transient responses elicited by time-varying stimuli. Overshoots, biphasic dynamics, adaptation kinetics, fold-change detection, entrainment, and cumulative exposure effects often determine phenotypic outcomes, yet are poorly captured by classical steady-state or dose–response analyses. This paper develops an input–output perspective on such *dynamic phenotypes*, emphasizing how qualitative features of transient behavior constrain underlying network architectures independently of detailed parameter values.

A central theme is the role of sign structure and interconnection logic, particularly the contrast between monotone systems and architectures containing antagonistic pathways. We show how incoherent feed-forward (IFF) motifs, operating across distinct time scales, provide a simple and recurrent mechanism for generating non-monotonic and adaptive responses across multiple levels of biological organization, from molecular signaling to immune regulation and population dynamics. Conversely, monotonicity imposes sharp impossibility results that can be used to falsify entire classes of models from transient data alone.

Beyond step inputs, we highlight how periodic forcing, ramps, and integral-type readouts such as cumulative dose responses offer powerful experimental probes that reveal otherwise hidden structure, separate competing motifs, and expose invariances such as fold-change detection. Throughout, we illustrate how control-theoretic concepts, including monotonicity, equivariance, and input–output analysis, can be used not as engineering metaphors, but as precise mathematical tools for biological model discrimination.

Taken together, the examples surveyed here argue for a shift in emphasis from asymptotic behavior to transient and input-driven dynamics as a primary lens for understanding, testing, and reverse-engineering biological networks.

1 Introduction

Understanding how network structure shapes dynamics is a central challenge in systems and synthetic biology. Signal-transduction pathways and feedback loops govern how biological systems, from molecular circuits involving ligands, transcription factors, and genes, to interacting cell populations in immunology or oncology, to large-scale social and epidemiological networks, process information and respond to stimuli. A key question is how the architecture of these networks constrains their possible dynamical behaviors, particularly the transient responses that arise before steady-state behavior manifests. In this work, we investigate what qualitative features of a network’s structure, meaning its interconnection pattern, graph-theoretic

This version compiled: 2026-01-05 at 01:47:44

Departments of BioEngineering and Electrical and Computer Engineering, and associate member of Departments of Chemical Engineering and Mathematics. Email: e.sontag@northeastern.edu

properties, and feedback organization, can be inferred from “dynamic phenotypes,” understood here as the time-dependent characteristics of responses to rich families of probing inputs beyond simple step changes.

This article offers a highly selective perspective, focusing largely on the author’s own experiences. It should not be taken as a comprehensive account of the field, to which many researchers have made foundational and influential contributions. Our aim is to illustrate, through a few representative examples, how network structure can impose sharp constraints on nonlinear system behavior and give rise to qualitative dynamical phenomena not present in linear systems. We highlight three classes of behavior: adaptation, fold-change detection (or scale invariance), and non-monotonic or subharmonic responses, sketching both the underlying mathematical principles and their relevance across biological scales. Detailed proofs and full mathematical developments are not presented here; instead, we point readers to the cited literature for complete treatments.

A remark on mathematics as a universal language. A recurring question that is often asked about quantitative life sciences is how mathematical methods can be applied across diverse biological contexts, and why systems that appear unrelated at first glance can nevertheless be described using similar mathematical structures. One illustrative example of this universality arises when comparing immune-tumor interactions with ecological predator-prey systems, Figure 1. Mathematics provides a common language for understanding interacting populations, whether in the tumor microenvironment or in ecosystems such as lynx and hares. In both settings, one population expands in response to the other: predators proliferate when prey are abundant, and immune effector cells activate and grow in number when tumor cells present recognizable antigens. Conversely, both systems exhibit suppressive dynamics in which predators reduce prey levels and immune responses constrain tumor growth. These reciprocal interactions generate rich transient and oscillatory behaviors shaped by nonlinear feedbacks, time delays, and resource limitations. At the same time, the analogy clarifies important difference: tumors can evolve escape mechanisms not found in ecological prey, and the immune system includes regulatory pathways with no direct ecological counterpart. Nevertheless, viewing immune-tumor and predator-prey interactions through a shared mathematical framework reveals how similar structural motifs can govern dynamics across biological scales.

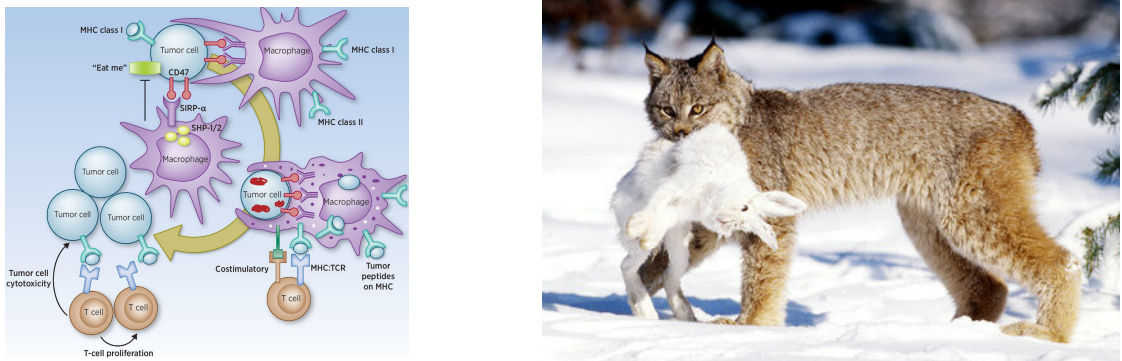


Figure 1: Predator-prey dynamics can model biological phenomena as varied as immune-tumor interactions or ecological behaviors.

Organization of the paper. In the remainder of this introduction, we highlight the importance of transient behaviors, drawing illustrative examples from multiple levels of biological organization, and introduce the mathematical framework used throughout the paper. The main body of the article is organized as a sequence of thematic “vignettes,” each anchored in concrete biological case studies. These vignettes address: (1) the role of monotonicity in shaping transient, as well as asymptotic, system behavior, with particular emphasis

on motifs such as incoherent feedforward structures and nonlinear feedback mechanisms; (2) the use of these concepts for the reverse engineering of signaling pathways from measured responses; (3) mechanisms of adaptation; (4) the use of periodic inputs to achieve finer discrimination among adapting motifs; (5) Weber’s law and scale invariance, together with their implications for bacterial chemotaxis; and (6) cumulative dose responses as an additional experimentally accessible “dynamic phenotype.” Appendices collect several mathematical details and technical arguments that are not readily available in the cited literature.

1.1 It’s not all in the asymptotics: transients matter!

This article emphasizes *transient responses* and dynamical behaviors induced by *time-varying inputs*, including periodic, pulsed, and otherwise nonstationary signals, rather than focusing exclusively on asymptotic stability properties. In this respect, our perspective departs from the traditional emphasis in control theory on equilibrium stabilization and long-term convergence.

That said, the systematic study of transient behavior is well established in classical control. Canonical examples include overshoot, rise time, settling time, and transient amplification in linear systems; input-output gain bounds and induced norms in robust control; and the use of lead-lag compensation to shape transient responses without altering steady-state behavior. More recently, transient performance has been a central concern in safety-critical control: control-barrier functions are routinely combined with control-Lyapunov functions to enforce state and output constraints while still guaranteeing stabilization, effectively providing dynamical “guardrails” that regulate trajectories during transients rather than only at equilibrium. Other examples include model predictive control, where finite-horizon performance criteria explicitly prioritize transient behavior, and adaptive or gain-scheduled controllers, where responses are shaped differently across operating regimes.

What distinguishes the biological setting is not the absence of such questions, but rather their centrality. In many biological systems, function is encoded not in steady states but in the temporal profiles of responses: pulse timing, pulse amplitude, adaptation kinetics, fold changes, cumulative exposure, and entrainment to rhythmic inputs. Moreover, biological systems are intrinsically nonlinear, stochastic, and subject to significant parameter variability, and their transient behaviors often carry semantic meaning, for example, distinguishing cell fates, triggering developmental decisions, or coordinating collective motion. These phenomena cannot be adequately understood by linearization around equilibria alone, nor by appealing solely to familiar nonlinear behaviors such as hysteresis, limit cycles, or chaos.

The focus on transient and input-driven dynamics therefore highlights a broader role for nonlinearity: not merely as a source of complex asymptotic behavior, but as a structural mechanism for robustness, invariance, and information processing under time-varying stimulation. In this sense, the biological questions addressed here align naturally with, but also extend beyond, classical control-theoretic paradigms.

Example: cell fate upon stress. In mammalian cells, one striking example of the role of transient dynamics is provided by their responses to certain types of stresses. The tumor suppressor gene *p53* is often referred to as the “guardian of the genome” and is mutated or functionally inactivated in more than 50% of human cancers. *p53* functions primarily as a stress-responsive transcription factor that is rapidly activated in response to diverse cellular insults, including DNA damage, oncogene activation, hypoxia, and metabolic stress. Once activated, *p53* regulates the expression of hundreds of target genes involved in DNA repair, cell-cycle checkpoints, apoptosis, senescence, and cellular metabolism, thereby acting as a central integrator of stress signals that determine cell fate [98, 99].

The review [81] surveys experimental and theoretical work demonstrating that distinct *dynamic phenotypes* of *p53* activation, rather than simply its absolute abundance, are closely linked to different cellular outcomes

following stress, such as DNA damage. In particular, (i) sustained trains of p53 pulses are commonly associated with the activation of apoptotic programs leading to programmed cell death; (ii) isolated or transient p53 pulses tend to trigger reversible cell-cycle arrest, during which DNA repair pathways are engaged and, if repair is successful, cells may re-enter the cell cycle and resume proliferation; and (iii) convergence of p53 activity to a persistently elevated steady state correlates with the induction of cellular senescence, a stable and largely irreversible fate characterized by permanent cell-cycle arrest while maintaining metabolic and secretory activity. These distinct temporal patterns are illustrated schematically in Figure 2.

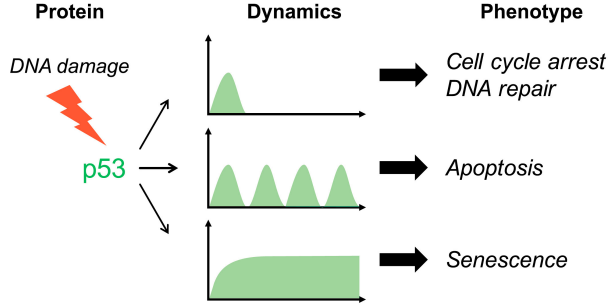


Figure 2: Phenotypical consequences of distinct p53 activation dynamics. Figure from [81].

Taken together, these observations underscore the critical role of p53 *dynamics*, including pulse frequency, duration, and temporal structure, in encoding information that directs cell fate decisions. They provide a paradigmatic example of how biological systems use transient and time-varying signaling behaviors, rather than static signal levels alone, to implement robust and context-dependent decision-making processes.

We next highlight the central importance of transient dynamics through a small set of additional motivating examples drawn from diverse areas of biology. A recurring theme across these examples is the appearance of non-monotonic responses. These often arise from the presence of *incoherent feedforward (IFF) motifs*. Such motifs consist of two distinct pathways linking an input to an output: a typically fast, activating pathway and a slower pathway that acts in opposition. The interplay between these competing influences naturally produces transient overshoots, delayed suppression, and other non-steady behaviors that cannot be inferred from asymptotic analysis alone. Despite their structural simplicity, IFF motifs provide a powerful and widely recurring mechanism for shaping time-dependent responses in biological systems. As we illustrate throughout the article, they, together with more classical negative feedback loops, offer a systems-level explanation for many seemingly disparate transient phenomena encountered in cellular signaling, immunology, and population dynamics.

Transients in infective population in an epidemic. Epidemic dynamics provide a particularly clear illustration of why *transient behavior*, rather than asymptotic stability, is often the dominant object of interest. A classical starting point is the SIR model, in which a population is divided into *susceptible* (S), *infectious* (I), and *removed* (R) individuals. Infectious individuals transmit the disease to susceptibles, who then become infectious themselves, while infectious individuals eventually recover or are removed (through immunity or death). On the time scales of interest here, we assume no return flow from the removed class back to the susceptible class. See Figure 3(left).

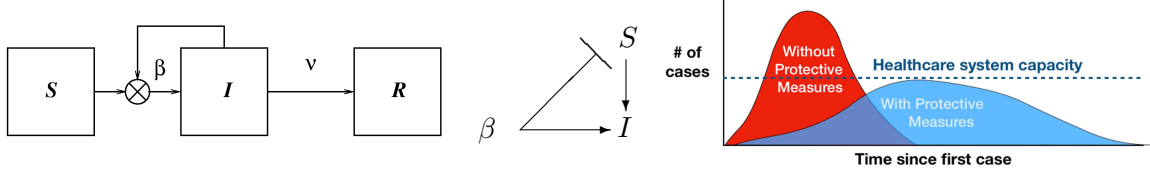


Figure 3: SIR model of epidemics. Left: Block diagram representation of the SIR model. Center: Incoherent feedforward structure implicit in the SIR model. Right: Flattening the curve in epidemics: the objective is to reduce the maximum number of infected individuals so that demand remains below healthcare capacity. Figure from [101].

Under the standard mass-action assumption in a well-mixed population, the dynamics are

$$\begin{aligned}\dot{S} &= -\beta SI, \\ \dot{I} &= \beta SI - \nu I, \\ \dot{R} &= \nu I,\end{aligned}$$

where $\beta > 0$ denotes the transmission (or contact) rate and $\nu > 0$ the recovery rate. Since $R(t)$ can be obtained by integrating $I(t)$, the essential dynamics are captured by the (S, I) subsystem.

From the standpoint of asymptotic behavior, the SIR model is mathematically unremarkable: regardless of parameter values, one always has

$$I(t) \rightarrow 0, \quad S(t) \searrow S_\infty > 0 \quad \text{as } t \rightarrow \infty.$$

Thus, on sufficiently long time scales, months or years after an outbreak, the infection inevitably dies out. From a purely stability-oriented viewpoint, this would suggest that there is little of interest to analyze.

In practice, however, *the transient dynamics are everything*. The primary epidemiological concern is not the eventual disappearance of the disease, but rather the magnitude and timing of the outbreak peak. When the basic reproduction number

$$\mathcal{R}_0 = \frac{\beta S_0}{\nu}$$

exceeds one, the number of infectious individuals initially grows, reaches a maximum, and then declines. The height of this peak, $\|I\|_\infty = \max_t I(t)$, determines whether healthcare systems are overwhelmed.

This motivates the widely adopted public-health objective of “flattening the curve,” illustrated schematically in Figure 3, where the goal is to reduce the peak number of infections so that it remains below treatment capacity.

From a control-theoretic perspective, epidemic mitigation acts primarily through modifications of the effective transmission rate β , using non-pharmaceutical interventions (NPIs) such as social distancing, masking, or mobility restrictions. Importantly, changes in β do not influence the system through a single pathway. An increase in β has an immediate positive effect on the growth rate of I , but it also accelerates the depletion of susceptible individuals S , which in turn reduces future infection rates. Conversely, a larger susceptible pool amplifies infection growth.

This interaction gives rise to an *incoherent feedforward (IFF) motif*. Seen in this light, β acts as an input that simultaneously promotes infection directly and, indirectly through its effect on S , contributes to suppressing future infection growth. A larger S increases I , while increased I decreases S . (As discussed later, we understand IFF as referring to the signed feedforward structure of the interaction graph, not to the presence or absence of feedback loops.) This structure is summarized schematically as shown in Figure 3. The resulting non-monotonic behavior of $I(t)$, initial growth followed by decline, is therefore a direct consequence of this

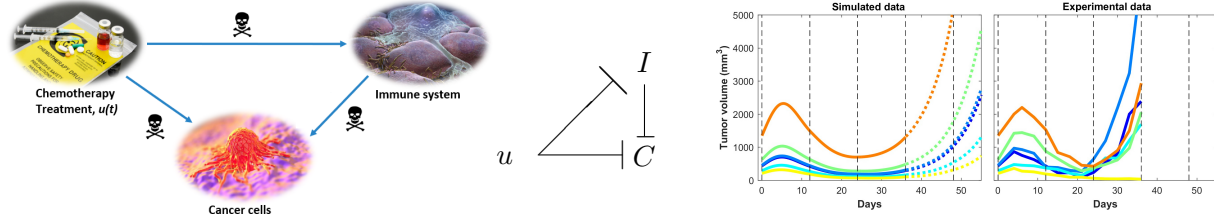


Figure 4: Left: Chemotherapy directly kills cancer cells, but collateral damage (“friendly fire”) also affects certain immune cell populations, thereby weakening immune-mediated regulation of tumor growth. Center: A simplified incoherent feedforward (IFF) representation of these interactions, where u denotes drug concentration, I immune components, and C cancer cells. This schematic is intentionally coarse-grained: chemotherapy can also exert immunostimulatory effects, and tumors actively recruit and modulate immune populations. Right: Representative treatment responses for a metronomic regimen with doses administered every 12 days. Solid curves show model fits [131] to experimental tumor-volume data from six mice reported in [138]. Following an initial reduction, tumor regrowth occurs after a delay, likely reflecting pharmacokinetic and pharmacodynamic effects as well as diminished immunogenic cell death. Independent measurements of immune activity in [138] confirm suppression of immune markers during treatment.

incoherent feedforward interaction. Crucially, this behavior is not an asymptotic property but a transient one. It is precisely this transient overshoot that public health interventions seek to shape.

This example reinforces a broader theme: in many biological and social systems, including epidemics, the most relevant questions concern peak responses, timing, and cumulative burden rather than long-term equilibria. The presence of incoherent feedforward interactions provides a mechanistic explanation for why non-monotonic transients arise naturally and why interventions that modestly alter parameters such as β can have disproportionately large effects on peak outcomes. Incoherent feedforward motifs will arise repeatedly in this article and serve as a central organizing theme.

We do not pursue epidemic modeling further in this paper, and instead refer the reader to the special issues [53–55], which survey a broad range of applications of control-theoretic methods to epidemic mitigation. In particular, the role of intervention timing, such as the scheduling of non-pharmaceutical interventions or “lockdowns” to minimize the peak number of infectious individuals $\max_t I(t)$, is studied, for example, in [120]. Adaptive and feedback-based control strategies aimed at reducing this peak are explored for example in [3].

Transients in response to chemotherapy. Although chemotherapy can induce rapid reductions in tumor burden, these benefits are often short-lived; tumor regrowth frequently follows as resistance develops. The resulting response is therefore non-monotonic and strongly time dependent, making transient dynamics central to therapeutic outcomes (see Figure 4, right). One plausible contributor to this lack of durability is that cytotoxic chemotherapy is not tumor-specific and may damage components of the host immune system, thereby weakening immune surveillance and long-term tumor control. For example, administration of cyclophosphamide (CPA) has been shown to reduce immune activity: experimental data reveal significant decreases in marker gene expression associated with natural killer (NK) cells, dendritic cells (DCs), and macrophages within the tumor microenvironment following CPA treatment [138]. Thus, a therapeutic input can have opposing effects: it may directly reduce tumor burden while simultaneously impairing immune mechanisms that would otherwise contribute to sustained suppression, as illustrated schematically in Figure 4 (left). From a systems-theoretic perspective, this antagonistic interaction is naturally represented by an *incoherent feedforward (IFF) motif*: increasing drug dose enhances direct tumor cell killing while concurrently diminishing immune-mediated clearance (Figure 4, center).

A longstanding paradigm in cancer chemotherapy is the *maximum tolerated dose* (MTD) strategy, in which cytotoxic drugs are administered at the highest doses that can be safely tolerated, with the aim of maximizing immediate tumor cell kill. However, high-dose chemotherapy often damages not only tumor cells but also key components of the immune system. Such immune impairment can substantially weaken immune-mediated tumor control, thereby promoting immunosuppression and increasing the likelihood of tumor relapse and the emergence of drug resistance [131]. These limitations help explain why the benefits of MTD regimens are frequently transient and accompanied by significant side effects. This perspective motivates *metronomic chemotherapy*, an alternative strategy that emphasizes sustained, low-dose, high-frequency drug administration. Rather than maximizing acute cytotoxicity, metronomic regimens aim to balance direct tumor cell killing with preservation, and in some cases enhancement, of anti-tumor immune responses, including immunogenic cell death. Because immune effects are mediated through complex processes within the tumor microenvironment, such as the recruitment of immunosuppressive populations and cytokine signaling, chemotherapy can exert both pro- and anti-immune influences, giving rise to strongly time-dependent and potentially non-monotonic treatment responses. Motivated by these considerations, the work [131] developed a mathematical framework for analyzing metronomic chemotherapy strategies. The resulting phenomenological model aggregates immunostimulatory and immunosuppressive effects into a small number of effective variables, including drug concentration and tumor volume, enabling systematic investigation of dosing schedules and their transient consequences. The model was calibrated using experimental data from [138] on metronomic cyclophosphamide treatment in an implanted GL261 glioma model at a dose of 140 mg/kg. Despite its simplicity, a single parameter set was sufficient to reproduce tumor responses across a wide range of treatment schedules, including non-monotonic transients consistent with an incoherent feed-forward structure. More broadly, this work illustrates how a focus on transient dynamics and network motifs can reveal mechanistic insights that are not apparent from steady-state or conventional dose–response analyses alone.

Transient responses and pseudoprogression in immune checkpoint blockade. The clinical development of immune checkpoint inhibitors, beginning with ipilimumab (anti-CTLA-4), highlighted the importance of transient response dynamics in cancer therapy. In a subset of patients, early radiographic assessments revealed an apparent worsening of disease, characterized by enlargement of existing lesions or the appearance of new lesions, followed later by tumor stabilization or regression. Such patterns were initially unexpected under conventional cytotoxic response paradigms, but are now widely recognized as manifestations of *pseudoprogression*. Mechanistically, this early increase in measured tumor burden is often attributed not to net malignant growth, but to immune-cell infiltration, inflammatory edema, and tissue remodeling triggered by immune activation. As a result, standard response criteria based solely on early changes in lesion size may misclassify effective immunotherapy as treatment failure. This issue is not merely academic: premature discontinuation of therapy or inappropriate removal of patients from clinical trials can occur if transient responses are interpreted using classical criteria alone. These observations motivated the development of immune-adapted response frameworks. The immune-related response criteria (irRC) [137] were among the first to explicitly accommodate atypical patterns of response by incorporating new lesions into an aggregate tumor burden rather than defining progression solely by their appearance. Subsequently, the iRECIST guidelines [104] formalized a two-stage notion of progression, distinguishing between *unconfirmed* immune progression (iUPD) and *confirmed* immune progression (iCPD), thereby allowing continued treatment in clinically stable patients until progression is verified on follow-up imaging.

From a dynamical systems perspective, immune checkpoint blockade illustrates how *transient behavior*, rather than asymptotic or steady-state response, can be the dominant determinant of therapeutic interpretation. Early inflammatory expansion followed by contraction is not an anomaly, but a signature of immune-mediated tumor control. The ipilimumab experience thus provides a paradigmatic example of why time-

resolved, input-driven dynamics must be incorporated into both clinical decision-making and mathematical models of cancer therapy.

At present, it remains difficult to identify which specific mechanisms are primarily responsible for the observed non-monotonic response patterns in immune checkpoint therapies. The immune–tumor interface involves a dense web of interacting pathways, many of which combine activating and inhibitory effects operating on different time scales. In particular, numerous incoherent feedforward (IFF) motifs, as well as classical negative feedback motifs, arise naturally in the regulation of immune activation, immune suppression, and tumor evasion in the context of immune checkpoint blockade. These motifs provide a plausible systems-level explanation for transient worsening, delayed responses, and other non-monotonic behaviors observed clinically. A schematic overview of some of these interactions is shown in Figure 5.

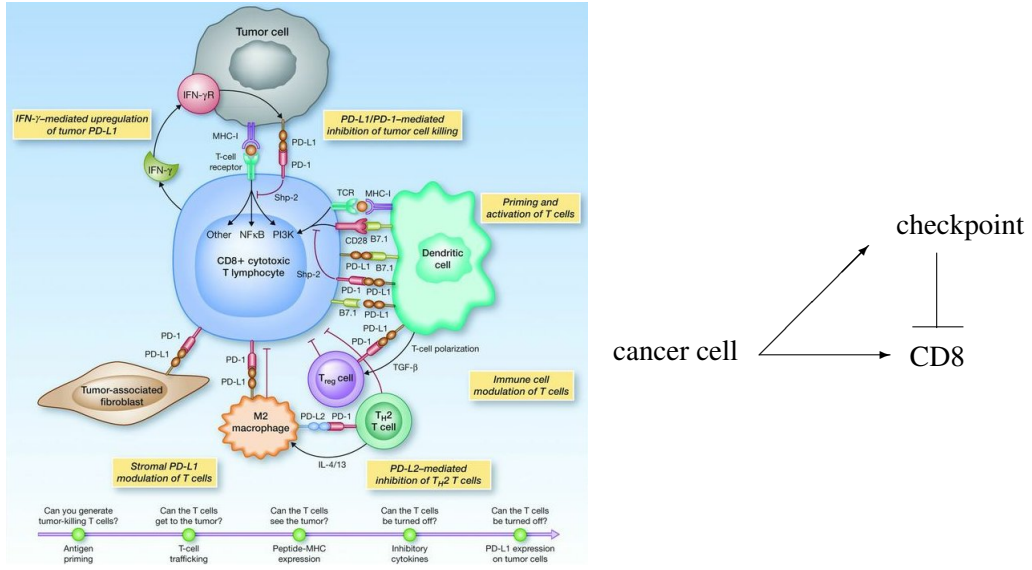


Figure 5: Schematic representation of interactions among immune components and between immune cells and tumor cells in the context of immune checkpoint regulation. Figure reproduced from [140]. Shown are both activating and inhibitory pathways, including the PD-L1/PD-1 inhibitory axis originating from tumor cells, which counterbalances T cell activation mediated by the MHC-I/TCR pathway (diagram on right). The coexistence of such antagonistic pathways naturally gives rise to incoherent feedforward and feedback motifs that can shape transient and non-monotonic response dynamics.

Immune detection of velocity of antigen presentation. In vertebrates, immunity emerges from the co-ordinated action of innate and adaptive components, protecting against pathogens and contributing to tumor immune surveillance. A basic requirement is discrimination: mounting strong responses to dangerous “nonself” cues while maintaining tolerance to self, a theme that traces back to classic self/nonself ideas (e.g., thymic negative selection of T cells) and the foundational proposals of Burnet and Talmage [1, 25, 68, 92, 126].

A purely static self/nonself picture is, however, difficult to reconcile with several well-known observations that point to an essential role for *dynamics*. The immune system stably tolerates commensal microbiota despite continual exposure to foreign molecular patterns; slow-growing tumors can evade detection even when expressing immunogenic antigens; chronic stimulation can drive functional hyporesponsiveness (e.g., reduced NK activation); and repeated exposure to inflammatory triggers can produce tolerance or “reprogramming,” as in endotoxin tolerance in macrophages [48, 92, 93, 136]. Likewise, lymphocyte anergy and

the clinical phenomenology of allergy desensitization suggest that not only antigen identity, but also *how stimulation changes in time*, can determine whether responses persist or shut down [24, 49, 92]. In a different context, Bocharov and colleagues [22] studied the effect of varying exponential rates of growth of Hepatitis B and Hepatitis C viral infections and found non-monotonic responses in immune responses.

Motivated by such phenomena, several authors have argued that immune recognition should incorporate *temporal features*—in effect, sensitivity to rates of change as well as levels. In this view, sustained effector responses are more likely to follow sufficiently rapid increases in stimulation, whereas slowly varying or chronic inputs can induce adaptation and tolerance. Representative formulations include the “tunable activation threshold” proposal of Grossman and Paul [49], along with later related perspectives such as the “discontinuity theory” [93] and growth-threshold ideas [14].

In this spirit, the phenomenological model introduced in [119] uses a simple circuit architecture to support dynamic discrimination of immune challenges. A central ingredient is an incoherent feedforward (IFF) motif. The IFF motif can render the response sensitive to exponential growth-like increases in stimulation—consistent with experimental evidence that rapidly increasing antigenic drive promotes reactivity. This paper suggested a plausible immunological implementation via interactions between effector and regulatory T-cell populations, Figure 6.

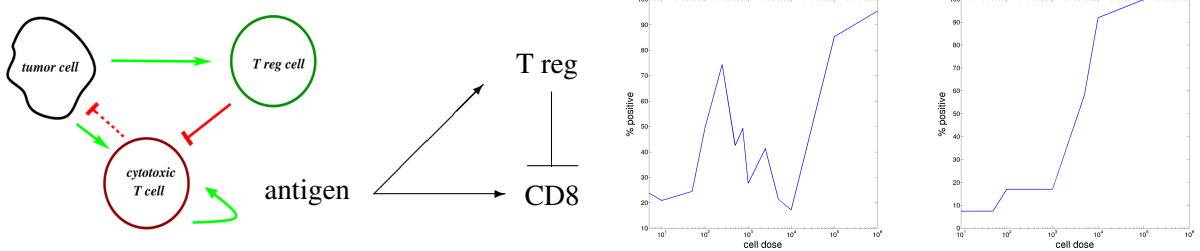


Figure 6: Left: conceptual diagrams showing T cell activation by antigens in tumor cells combined with recruitment of T regulatory cells which in turn repress activation. Self-activation of T cells populations, and a slower negative feedback from immune cells into tumor cells are also included in the mathematical model in [119]. Right: plots showing non-monotonic response in the presence of an inhibitory node, and monotone response when the inhibitory node is removed, using data from [43].

The diagrams in Figure 6 are oversimplifications of a complex network of interactions, and only intended as a cartoon that lets one understand dynamic behavior. The key point is that increasing antigen exposure can promote rapid activation and proliferation of cytotoxic $CD8^+$ T cells while also, through slower and indirect pathways, enhancing the expansion and suppressive function of regulatory T cells (Tregs), which in turn inhibit $CD8^+$ effector activity. An important component of this antagonism arises from competition for shared cytokine resources, particularly interleukin-2 (IL-2), which is produced by activated effector T cells but preferentially consumed by Tregs due to their high constitutive expression of the IL-2 receptor α chain (CD25). This coarse-grained diagram therefore abstracts multiple interacting mechanisms, including antigen presentation by dendritic cells, cytokine-mediated feedback, metabolic and receptor-level competition, and threshold modulation, into an effective feedforward inhibitory structure. Such motifs provide a conceptual framework for understanding non-monotonic and transient immune responses, emphasizing that immune outcomes depend not only on antigen magnitude but also on timing, kinetics, and the balance of shared regulatory resources.

When combined with a positive feedback on T cell activation and inhibitory regulation, the model reproduces a nontrivial dependence of outcome on tumor growth rate, including regimes of elimination and tolerance reminiscent of the experimentally reported “two-zone tumor tolerance” and “sneaking through” phenomena.

The seminal study by Gatenby, Basten, and Creswick [43] had reported a striking non-monotonic relationship between tumor inoculum size and tumor take, a phenomenon they termed sneaking through. Using a syngeneic Meth-A fibrosarcoma model in BALB/c mice, the authors showed that very small numbers of tumor cells were able to establish progressive tumors almost as effectively as very large inocula, whereas intermediate inocula were more frequently rejected. This effect was shown to be strongly T-cell dependent: it disappeared in nude mice and in animals depleted of T cells, reappeared upon T-cell reconstitution, and was abolished by cyclophosphamide treatment, which at the time was known to preferentially eliminate suppressor T-cell populations. See Figure 6 and discussion in [119]. Furthermore, repeated exposure to low doses of irradiated tumor cells induced a state of tumor-specific susceptibility, closely resembling classical low-zone tolerance. Collectively, these observations support the interpretation that early tumor growth can actively induce an immunosuppressive state, allowing tumors to evade immune surveillance during their initial expansion.

A historical remark is in order, as these older papers are hard to interpret in light of contemporary literature, regarding the meaning of the regulatory node. In the immunological framework of the 1970s and 1980s, the immunosuppressive population implicated in sneaking through was referred to as *T suppressor (T_s) cells*. Although the T_s concept later fell out of favor due to difficulties in phenotypic identification and experimental reproducibility, it is now widely accepted that many of the functions attributed to these cells correspond to those of modern *regulatory T cells* (T_{reg}), in particular CD4⁺CD25⁺ FOXP3⁺ T cells. Regulatory T cells mediate peripheral tolerance by actively suppressing effector T-cell responses through mechanisms including the secretion of inhibitory cytokines such as IL-10 and TGF- β , metabolic competition, and inhibitory receptor signaling. These mechanisms are fully consistent with the tumor-specific, cyclophosphamide-sensitive suppression observed in the sneaking-through experiments. From a modern perspective, the results of Gatenby *et al.* can thus be reinterpreted as an early demonstration of tumor-induced regulatory immunity, in which small or slowly growing tumor burdens preferentially recruit or induce regulatory T cells, leading to immune tolerance rather than rejection. This reinterpretation places the sneaking-through phenomenon within contemporary theories of cancer immunoediting and highlights its relevance to current views of dynamic immune regulation in tumor–host interactions.

Are these dynamic effects relevant to therapy? Kündig and collaborators further sharpened the case for a dynamic view of immune recognition by demonstrating that *the temporal profile of antigen exposure alone* can decisively shape immune reactivity [62]. Using both dendritic cell vaccination protocols and controlled *in vitro* stimulation of T cells, they showed that antigen delivery schedules with identical cumulative dose but different kinetics elicited markedly different responses. In particular, antigenic stimulation that increased exponentially over several days induced substantially stronger CD8⁺ T-cell activation and antiviral immunity than either a single bolus dose or repeated equal daily doses. At the cellular level, they found that IL-2 production was minimal under constant stimulation, increased under linearly rising stimulation, and was maximal under exponential stimulation, indicating that T cells are capable of decoding higher-order temporal features of antigen exposure. These results led the authors to conclude that antigen kinetics constitute an independent informational dimension in immune signaling, distinct from antigen identity or total dose. On the basis of this principle, Kündig and coauthors later obtained a patent proposing vaccination strategies based on exponentially increasing antigen presentation to enhance CD8⁺ T-cell responses, explicitly emphasizing that immunogenicity can be amplified in a manner largely independent of absolute antigen dose [70]. Taken together, these findings provide experimental support for models in which immune circuits—often containing incoherent feedforward or autocatalytic structures—are tuned to preferentially amplify rapidly accelerating stimuli, consistent with the broader theme that transient (growth-rate-dependent) signals play a central role in immune decision making.

1.2 Formalism from control theory: I/O systems

Although our discussion will remain informal, referring to the literature for rigorous details and most proofs, we will, for concreteness, frame all results in the setting of finite-dimensional deterministic continuous-time systems with inputs and outputs in the standard sense of control theory, $\dot{x} = f(x, u)$, $y = h(x, u)$ or in coordinates:

$$\begin{aligned}\dot{x}_1 &= \frac{dx_1(t)}{dt} = f_1(x_1(t), \dots, x_n(t), \underbrace{u_1(t), \dots, u_m(t)}_{\text{inputs}}) \\ &\vdots \\ \dot{x}_n &= \frac{dx_n(t)}{dt} = f_n(\underbrace{x_1(t), \dots, x_n(t)}_{\text{states}}, \underbrace{u_1(t), \dots, u_m(t)}_{\text{inputs}}) \\ y_j(t) &= h_j(x(t), u(t)) \quad \leftarrow \text{output variables.}\end{aligned}$$

The functions $f = (f_1, \dots, f_n)^T$ and h describe respectively the dynamics and the read-out map. Here, the forcing function $u = u(t)$ is a generally time-dependent external input (in various biological contexts, one might refer to u as a “stimulus” or an “excitation”), $x(t) = (x_1(t), \dots, x_n(t))$ is an n -dimensional vector of state variables, and $y(t)$ is the output (“response,” “measurement,” or “reporter”) variable such as, for example $y(t) = x_n(t)$, which would simply be a read-out of the value of x_n . In molecular biology, the components x_i of x might represent concentrations of chemical species (proteins, mRNA, metabolites); in epidemiology, they may represent different populations (young/mature/old, immune/susceptible/infected, etc.).

In order to impose constraints such as positivity of variables, we introduce the following additional notations. States, inputs, and outputs are constrained to lie in particular subsets \mathbb{X} , \mathbb{U} , and \mathbb{Y} respectively, of Euclidean spaces $\mathbb{R}^n, \mathbb{R}^m, \mathbb{R}^q$. In order to avoid keeping track of domains of existence of maximal solutions, we will assume that for each piecewise-continuous input $u : [0, \infty) \rightarrow \mathbb{U}$, and each initial state $\xi \in \mathbb{X}$, there is a unique solution $x : [0, \infty) \rightarrow \mathbb{X}$ with initial condition $x(0) = \xi$, which we write as $\varphi(t, \xi, u)$, and we denote the corresponding output $y : [0, \infty) \rightarrow \mathbb{Y}$, given by $h(\varphi(t, \xi, u), u(t))$, as $\psi(t, \xi, u)$. See any textbook, e.g. [113] for precise definitions and elementary properties.

2 Monotonicity

Systems whose dynamics preserve a partial order are called *monotone systems*. Such systems inherit monotone response properties when initialized at steady state: for example, a nondecreasing input can never produce a biphasic (U-shaped or inverted U-shaped) output response. Monotone systems have been studied since at least the 1980s by Hirsch, Matano, Smith, Smale, and many others; see the expositions [58, 111] and the general discussion in [115]. They are dynamically “well-behaved” in several important senses. For instance, if the system has a unique equilibrium, then every bounded trajectory converges to it [33]. When multiple equilibria are present, and under a mild technical assumption of *strong monotonicity*, solutions generically converge to equilibria, as stated in Hirsch’s Generic Convergence Theorem [56, 57]. In particular, such systems cannot exhibit chaotic dynamics nor even stable limit cycles, a fact also proved for the special case of cooperative systems (defined below) in [51]. Many of these results extend to delay-differential systems and to systems governed by partial differential equations.

Traditionally, monotone systems were defined only for autonomous systems (i.e., without inputs or outputs). The paper [9] introduced a natural extension of the concept to systems with inputs and outputs. This

extension enables an interconnection-based framework for verifying monotonicity in large networks and facilitates the analysis of non-monotone feedback loops, as illustrated in an example below.

Suppose given partial orders on the sets \mathbb{X} , \mathbb{U} , and \mathbb{Y} of states, inputs, and outputs. We denote all these orders by the same symbol \preceq , but the meaning will be clear from the context. A monotone system is one for which, for all inputs and initial states,

$$u(t) \preceq v(t) \forall t, x \preceq z \Rightarrow \varphi(t, x, u) \preceq \varphi(t, z, v) \forall t$$

and also the output map h is monotone:

$$x_1 \preceq x_2 \Rightarrow h(x_1) \preceq h(x_2).$$

Typically, the partial order is specified by a convex pointed cone K through the following rule:

$$b \succeq a \Leftrightarrow b - a \in K.$$

A special type of cone is provided by the possible orthants $K_\sigma \subset \mathbb{R}^n$, with $\sigma \in \{1, -1\}^n$, where $x \in K_\sigma$ means that, for each i , $\text{sign}(x_i) = \sigma_i$ or $x_i = 0$. A system that is monotone with respect to cones of the form K_σ is said to be *orthant-monotone*. For example, when $K = K_{(1,1,\dots,1)}$, the main orthant in \mathbb{R}^n , we obtain the *NorthEast (NE) order* for which “ $x \preceq z$ ” means that $x_i \leq z_i$ for each $i = 1, \dots, n$. A system that is monotone with respect to the NE order in the spaces of input, states, and outputs is said to be a *cooperative* system. Under a coordinate change $x_i \mapsto \sigma_i x_i$ (and similar transformations on inputs and output spaces), any orthant monotone system becomes a cooperative system. Cooperative systems are characterized by the property that, for every i , f_i is nondecreasing with respect to each x_j , $j \neq i$ and with respect to all input coordinates, and (if there are outputs) each coordinate $h_j(x)$ is nondecreasing with respect to each coordinate of x . (Figure 7).

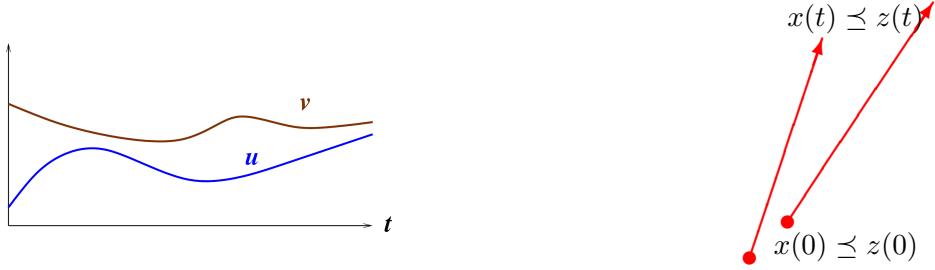


Figure 7: Cooperativity. Suppose that $x(0) \preceq z(0)$, meaning (NE order) that $x_i(0) \leq z_i(0)$ for each coordinate, so that $z(0)$ is to the “NorthEast” of $x(0)$, and that two inputs u, v are given such that $u_j(t) \leq v_j(t)$ for all $t \geq 0$ (illustrated here with scalar inputs). Then $x(t) \preceq z(t)$ for all $t \geq 0$.

Let us illustrate the power of monotonicity through a simple example for the very special case of two-dimensional cooperative systems. We claim that in such a system there cannot exist any periodic orbits. Figure 8 sketches the proof. (In dimensions greater than three, periodic orbits can exist in monotone systems, but they must be unstable.)

2.1 Signed graphs and orthant-monotone systems

We assume here that \mathbb{X} and \mathbb{U} are open subsets of \mathbb{R}^n and \mathbb{R}^m and that the partial derivatives

$$\frac{\partial f_j}{\partial x_i}(x, u) \quad \text{and} \quad \frac{\partial f_j}{\partial u}(x, u)$$

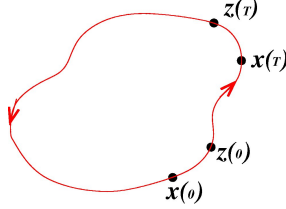


Figure 8: In a cooperative planar system, there cannot exist any periodic solution. A sketch of proof is as follows. Suppose that there is clockwise oriented solution. (The counter-clockwise case is analogous.) Pick two initial states as shown: $x(0) \preceq z(0)$. As time evolves, the solution from $x(0)$ eventually will be at a point $x(T)$ as shown, where T is picked so that the $x_1(T)$ -coordinate is maximized and among such points the $x_2(T)$ coordinate is maximized. Cooperativity would imply that $x(T) \preceq z(T)$, which cannot happen since solutions cannot cross.

have a constant sign (either ≥ 0 or ≤ 0) for all $(x, u) \in \mathbb{X} \times \mathbb{U}$. (For cooperative systems, these are all nonnegative.) For those derivatives that are not identically zero, we write φ_{ij} and γ_i for their signs (± 1):

$$\varphi_{ij} := \text{sign} \frac{\partial f_j}{\partial x_i}(x, u) \quad \text{and} \quad \gamma_i := \text{sign} \frac{\partial f_i}{\partial u}(x, u)$$

and let $\varphi_{ij} = 0$ or $\gamma_i = 0$ if the corresponding derivative is identically zero. The effect of any given variable x_j on the rate of change of a different variable x_i is “activating” or “inhibiting” depending on Jacobian signs:

- x_j activates x_i (“ $x_j \rightarrow x_i$ ”) if $\frac{\partial \dot{x}_i}{\partial x_j} = \frac{\partial f_i}{\partial x_j}(x, u) > 0$
- x_j inhibits x_i (“ $x_j \dashv x_i$ ”) if $\frac{\partial \dot{x}_i}{\partial x_j} = \frac{\partial f_i}{\partial x_j}(x, u) < 0$

and similarly for the effects of inputs u_j ’s on the x_i ’s. (If outputs are of interest, similar terminology and notations are used.) We summarize these effects through a directed signed (edges are labeled by activation or repression arrows, or labeled “+” or “-”) graph; see for example Figure 9.

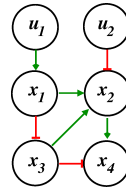


Figure 9: An example of a signed graph associated to a system. Here $\frac{\partial f_1}{\partial u_2} \equiv 0$, $\frac{\partial f_4}{\partial x_2} > 0$, $\frac{\partial f_3}{\partial x_1} < 0$, and so forth.

A (graph) path π from the input u to a node x_j means, by definition, a sequence of k indices $\ell_1, \ell_2, \dots, \ell_k = j$ such that $\gamma_{\ell_1} \neq 0$ and $\varphi_{\ell_i, \ell_{i+1}} \neq 0$ for all $i = 1, \dots, k-1$. We denote by $s(\pi)$ the sign of the path, defined as the product $s(\pi) := \gamma_{\ell_1} \varphi_{\ell_1 \ell_2} \varphi_{\ell_2 \ell_3} \dots \varphi_{\ell_{k-1} \ell_k}$. Similarly, a path from a node x_i to a node x_j means, by definition, a sequence of k indices $\ell_1, \ell_2, \dots, \ell_k = j$ such that $\varphi_{i, \ell_1} \neq 0$ and $\varphi_{\ell_i, \ell_{i+1}} \neq 0$ for all $i = 1, \dots, k-1$. We denote by $s(\pi)$ the sign of the path, defined as the product

$$s(\pi) := \varphi_{i \ell_1} \varphi_{\ell_1 \ell_2} \varphi_{\ell_2 \ell_3} \dots \varphi_{\ell_{k-1} \ell_k}.$$

If there is a path from the input u to a node x_j , we say that x_j is *(graph) reachable*. If there is a path from a node x_i to the output node x_n , we say that the node x_i is *(graph) observable*.

2.2 Connections to spin models (“coherence” or “non-frustration”)

Given a directed graph with edges labeled positive or negative, a *spin assignment* or *switching function* is an assignment of a label to each node v_i , written as a sign [or, in physics, an uparrow or downarrow]:

$$\sigma_i \in \{\pm 1\} \quad [\text{or } \sigma_i \in \{\uparrow, \downarrow\}]$$

and such an assignment is said to be *consistent* if every edge with sign $J_{ij} \in \{\pm\}$ is consistent, meaning that $\sigma_j = J_{ij}\sigma_i$, see Figure 10. The graph said to be *balanced* if there exists at least one consistent assignment among all possible 2^n spin assignments.



Figure 10: Three signed edges and consistent or inconsistent assignments

It is an easy exercise to show that *a graph is balanced if and only if every undirected loop (ignore directions but keep signs) has a positive parity*, that is to say, contains an even number of negative edges. Equivalently, any two (undirected) paths between two nodes have same parity. (We did not define “undirected” paths. These are paths in the graph $G \cup G^\top$ where we include an edge from node j to node i if there is an edge from i to j , and assign the same sign to it. If there was already an edge from j to node i , and it had the opposite sign, the graph is not balanced.)

Yet another equivalent property is also easy to prove, and has been often used in the theory of social interactions, dating at least to a 1954 paper by Harary (see the discussion in [100]). A graph is *balanced* if and only if the vertices can be partitioned into two subsets so that every edge joining vertices within a class is positive and every edge joining vertices in different classes is negative, see Figure 11. In this form, the concept of balancing plays an important role in the study of collective phenomena such as the emergence of consensus or polarization in human societies or social decisions in animal groups, as discussed in [20].

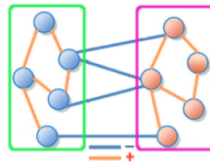


Figure 11: A balanced graph (directions of arrows ignored) partitioned into two sets of consistent nodes. Orange edges are positive and blue edges are negative. Think of nodes as representing individuals: Individuals like others in their own group, but dislike individuals in the other group.

One can prove the following key equivalence: *A system is orthant-monotone if and only if its interaction graph is balanced*.

2.3 Predictability of behavior in balanced networks

With regard to transient dynamics, balanced graphs exhibit highly robust and unambiguous responses to perturbations at specific nodes. Consider the two graphs shown in Figure 12. In the left-hand graph, every path connecting nodes 1 and 4 has a net positive sign, so the graph is balanced. If node 1 is instantaneously perturbed upward, both the path $1 \rightarrow 3 \rightarrow 4$ and the alternative path $1 \dashv 2 \dashv 4$ transmit a net positive effect to node 4: along the second path, the increase in node 1 decreases node 2, thereby reducing repression of node 4 and ultimately causing node 4 to increase. Thus, all paths convey the same qualitative information, and the effect on node 4 is unambiguous.

The situation differs for the graph on the right. The path $1 \rightarrow 3 \rightarrow 4$ remains net positive, but the alternative path $1 \rightarrow 2 \dashv 4$ has a net negative sign. This graph is therefore not balanced. A perturbation at node 1 now yields conflicting qualitative predictions: one path indicates that node 4 should increase, whereas the other predicts a decrease. This “incoherent feedforward” structure makes the effect of the perturbation indeterminate from graph topology alone; it will depend on which path dominates, a feature determined by the specific algebraic form and parameter values of the interactions.

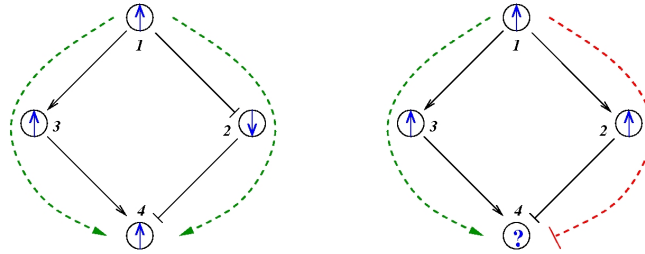


Figure 12: Balanced and unbalanced graphs (dashed lines show net parity along each path). Left graph is balanced; right graph is not.

Intuitively, balancing insures a predictable, unambiguous, global effect of node perturbations. As a concrete example for the second graph, suppose that the equations for the system are as follows:

$$\frac{dx_1}{dt} = 0 \quad \frac{dx_2}{dt} = x_1 \quad \frac{dx_3}{dt} = x_1 \quad \frac{dx_4}{dt} = x_4(k_3x_3 - k_2x_2),$$

where the reaction constants k_2 and k_3 are two positive numbers. The initial conditions are taken to be $x_1(0) = x_4(0) = 1$, and $x_2(0) = x_3(0) = 0$, and we ask how the solution $x_4(t)$ will change when the initial value $x_1(0)$ is perturbed. With $x_1(0) = 1$, the solution is $x_4(t) = \exp \alpha t^2/2$, where $\alpha = k_3 - k_2$. On the other hand, if $x_1(0)$ is perturbed to a larger value, let us say $x_1(0) = 2$, then $x_4(t) = \exp \alpha t^2$. This new value of $x_4(t)$ is larger than the original unperturbed value $\exp \alpha t^2/2$ provided that $\alpha > 0$, but it is smaller than it if, instead, $\alpha < 0$. In other words, the sign of the sensitivity of x_4 to a perturbation on x_1 cannot be predicted from knowledge of the graph alone, but it depends on whether $k_2 < k_3$ or $k_2 > k_3$. Compare this with the balanced case, as the left graph in Figure 12. A concrete example is obtained if we modify the x_2 equation to $dx_2/dt = 1/(1 + x_1)$. Now the solutions are $x_4(t) = \exp \beta_1 t^2$ and $x_4(t) = \exp \beta_2 t^2$ respectively, with $\beta_1 = k_3/2 - k_2/4$ and $\beta_2 = k_3 - k_2/6$, so we are guaranteed that x_4 is larger in the perturbed case, a conclusion that holds true no matter what are the numerical values of the (positive) constants k_i .

2.4 Biological networks, balancing, and monotonicity

Systems molecular biology seeks to understand the behavior of biochemical networks composed of proteins, RNA, DNA, metabolites, and other molecular species. These networks mediate control and signaling in development, regulation, and metabolism by processing environmental cues, coordinating internal events such as gene expression, and generating appropriate cellular responses. Unlike many areas of applied mathematics and engineering, the study of dynamics in biology, and especially in cell biology, must confront the substantial uncertainty inherent in models of intracellular biochemical networks. This uncertainty arises from environmental fluctuations as well as variability among cells of the same type. For instance, concentrations of enzymes, transcription factors, metabolites, mRNAs, and many other molecular components can vary widely both across cells within a single organism and across individuals. Physical factors such as pH, temperature, and other environmental conditions further influence biological processes, while ecological interactions with other individuals introduce additional sources of variability.

Yet, despite these uncertainties, biological behaviors are often remarkably predictable and robust. From a mathematical standpoint, uncertainty manifests as difficulty in measuring key model parameters, such as kinetic constants or cooperativity indices, and therefore makes it impossible to obtain fully specified models. This motivates the development of analytical tools that are robust in the sense that they yield meaningful conclusions based solely on the qualitative features of a network, ideally without relying on precise parameter values or even exact reaction forms. Achieving such robustness is challenging, since dynamical behavior may undergo bifurcations or other phase transitions that depend sensitively on parameter values. Balancing, and more generally monotonicity, provides a degree of predictability and robustness to network responses, as discussed above.

As surveyed in [115], it has long been understood that system behavior depends critically on the network's topology and on the signs (activating or inhibiting) of its feedforward and feedback interconnections. See for example [36, 37, 45, 64, 75, 84–86, 89, 103, 128]. For example, Figures 13(a-c) illustrate the three possible types of feedback loops that involve two interacting chemicals. A mutual activation configuration is shown

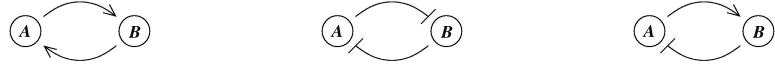


Figure 13: (a) Mutual activation. (b) Mutual inhibition. (c) Activation-inhibition.

in Figure 13(a): a positive change in A results in a positive change in B , and vice versa. Such configurations are associated with signal amplification and the production of switch-like biochemical responses. A mutual inhibition configuration is shown in Figure 13(b): a positive change in A represses B , and repression of B in turn enhances A . These configurations allow systems to exhibit multiple discrete alternative stable steady states and thereby provide a mechanism for biochemical memory. Both Figures 13(a) and 13(b) represent positive-feedback systems[8, 11, 28, 47, 90, 94, 97, 129].

In contrast, activation-inhibition configurations such as that in Figure 13(c) are essential for generating periodic behaviors, including circadian rhythms and cell-cycle oscillations. They may occur alone or in combination with multistable positive-feedback subsystems. These configurations also underlie adaptation, disturbance rejection, and the tight regulation (homeostasis) of physiological variables[10, 37, 45, 52, 67, 86, 91, 96, 105, 113, 127, 133]. Unlike positive-feedback systems, negative-feedback systems are not balanced. In case (c), a positive change in A is counteracted by the feedback loop, resisting the perturbation.

Balancing, or the lack of it, also influences the behavior of graphs that do not contain feedback loops. For example, [82–84] analyze the distinct signal-processing characteristics of balanced (“coherent”) compared to nonbalanced (“incoherent”) feedforward motifs. Thus, balancing can play a central role in understanding the qualitative dynamics of biochemical networks.

Of course, there is no a priori reason for a system to have a balanced interaction graph. Yet we speculate that: (1) systems that are “nearly balanced” may be, statistically, more biologically advantageous than those that are far from monotone, in the sense that they tend to exhibit more regular dynamical behavior; and (2) real biological networks may lie much closer to being balanced than random networks with the same numbers of vertices and the same distribution of positive and negative edges. To the best of our knowledge, there is *no precise mathematical formulation*, let alone a proof, of these conjectures. Nonetheless, several intriguing observations point in this direction, which we briefly review below in the hope of stimulating further research.

2.5 Near-monotonicity in biological networks

Since balanced structure in biological networks may be advantageous, one might conjecture that natural biological networks tend to be more balanced than expected by chance. To explore this hypothesis, we introduced a measure of frustration or imbalance, the consistency deficit (CD) of a graph G , defined as the smallest number of edges that must be removed from G to render the remaining graph balanced. An algorithm for computing this quantity was presented in [34].

We applied this method to the gene regulatory network of the yeast *Saccharomyces cerevisiae*, as compiled in [84] and obtained from [4] (the data in [84] originate from the YPD database [32]). In this network, nodes correspond to genes, and edges are directed from transcription factors, or transcription-factor complexes, to the genes they regulate. The network contains 690 nodes and 1082 edges, of which 221 are negative and 861 are positive. (We treated the single “neutral” edge as positive; the conclusions remain essentially unchanged if it is treated as negative or simply removed.) Using the approximation algorithm of [34], we estimated the CD to be 43. The exact algorithm of [61] subsequently refined this estimate, yielding the precise value CD=41. Thus, *removing only about 4% of the edges suffices to make the network balanced*. Equally striking is the structural effect of these deletions. The original graph has 11 connected components: one large component of size 664, one of size 5, three of size 3, and six of size 2. After deleting the 41 edges, all components remain connected. The deleted edges lie entirely within the largest component and involve a total of 65 nodes from that component.

To assess whether a small CD could arise merely by chance, we also applied the algorithm to random graphs with 690 nodes and 1082 uniformly chosen edges, of which 221 edges were designated as negative (also uniformly). For these random graphs, approximately 12.6% of edges (136.6 ± 5) had to be removed to achieve balance. To examine how this scales with network size, we generated random graphs with N nodes and $1.57N$ edges, of which $0.32N$ were negative. For $N > 10$, roughly $N/5$ edges needed to be removed to obtain a balanced graph, consistent with the value observed for $N = 690$. Thus, the CD of the yeast network lies about *15 standard deviations* below the mean CD for random graphs, an extremely unlikely event by chance alone. Both the network’s *topology* (underlying graph structure) and its *edge signs* contribute to this unusually high degree of balance. To disentangle these effects, we conducted the following numerical experiment. We randomly flipped the signs of 50 positive and 50 negative edges, producing a network with the same topology and the same total number of positive and negative edges as the original, but with 100 edges assigned new, random signs. In this modified network, about 8.2% of edges (88.3 ± 7.1) must be deleted to achieve balance, intermediate between the original yeast network and random graphs. Flipping more signs (100 positives and 100 negatives) yields a still less balanced network, requiring 115.4 ± 4.0 deletions (about 10.7% of edges), although this remains noticeably lower than the value for a fully random network.

Analogous analyses were carried out for an *E. coli* gene regulatory network, a *S. cerevisiae* gene regulatory network, and a signaling network in a CA1 hippocampal neuron. These studies likewise found that all three

intracellular regulatory networks are, in a meaningful sense, far more balanced than would be expected by chance [80]. The three networks examined share several structural features: similar node-to-link ratios, comparable proportions of positive and negative edges, and “small-world” characteristics, including high clustering coefficients and characteristic path lengths close to those of random networks. They also exhibit connectivity distributions that are well fit by power laws, indicating an enrichment of highly connected nodes (hubs). In such networks, certain genes or proteins directly regulate, or are regulated by, many others. By comparing the numbers of positive and negative feedback and feedforward loops in the real networks versus sign-shuffled versions, the study showed that the biological networks contain significantly more positive loops than would be expected in randomized counterparts.

In summary, biological networks appear to be far more balanced than one would expect by chance alone. What are the dynamical implications of this observation? Formulating a precise theorem is challenging, since even systems with only a few feedback loops can exhibit highly complex behavior. Nevertheless, it would be extremely valuable to make this intuition rigorous, for example by showing that in a randomly selected family of systems that are “close” to balanced, one consistently observes some form of regularity in their dynamics. A preliminary computational investigation was carried out in [121], where numerical experiments on discrete-time, discrete-state (Boolean) systems revealed a correlation between a measure of imbalance and the lengths of their periodic orbits.

In [80], we argue that cellular regulatory networks exhibit remarkably stable behavior despite noisy and rapidly changing environments and that a growing body of evidence suggests that this robustness may arise from the fact that intracellular networks are often “close to monotone” in their structure. In particular, real biological networks appear enriched in positive feedback and feedforward loops and depleted in negative “inconsistent” loops, which are known to promote oscillations or other unstable dynamics. Although negative feedback is traditionally viewed as essential for homeostasis, empirical network topologies reveal that such loops are relatively uncommon. Instead, stability in many cellular systems is achieved through constitutive degradation or deactivation processes, for example by broad-specificity phosphatases in signaling pathways, that dampen signals without requiring explicit negative feedback. This structural bias toward sign-consistent interactions provides a plausible mechanism for the stable dynamical behavior observed in cells. Monotone or near-monotone architectures also confer advantages beyond stability, including ordered responses, predictable input-output behavior, and greater modularity under evolutionary pressures. Networks composed primarily of positive feedforward and feedback connections tend to maintain consistent qualitative relationships between distant components: perturbing a node or modifying reaction rates leads to graded changes in downstream activity that may eventually decay due to housekeeping negative regulators. In contrast, networks containing inconsistent loops can exhibit oscillations or even chaotic responses to small parameter changes. Observed biochemical network architectures align with these theoretical expectations. For example, in mammalian signaling pathways the number of protein kinases greatly exceeds that of corresponding phosphatases, and kinases function predominantly as activators while phosphatases act as broadly acting, relatively unregulated negative hubs. This asymmetry naturally favors sign-consistent circuitry and may provide a genetic basis for the prevalence of monotone-like motifs in cellular signaling networks.

2.6 Decompositions or embeddings into monotone systems

Sometimes non-monotone systems can be interpreted as negative feedback interconnections of monotone subsystems. For example, a system with a non-balanced interaction graph, as shown in Figure 14, can be decomposed into two subsystems, each with a balanced graph, although their interconnection destroys the overall balance.

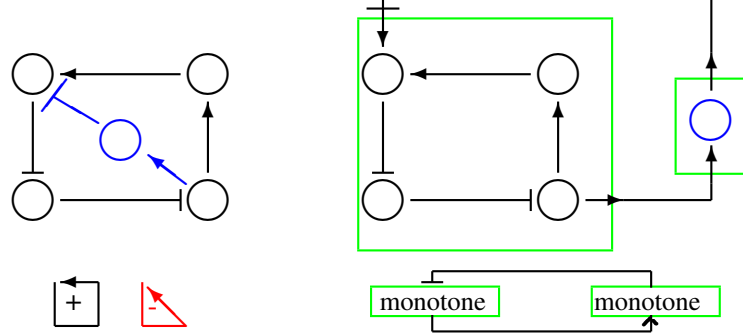


Figure 14: Graph on the left is not balanced (compare black-square positive path and red-triangle negative path) but can be decomposed into two balanced systems, as a negative feedback interconnection of two balanced graphs corresponding to two monotone systems.

Such decompositions do not always exist. However, it is often possible to embed a non-monotone system into a higher-dimensional monotone system, sometimes of roughly twice the original dimension, an idea that can be traced at least to the work of [46]. This idea underlies the introduction of the formalism of monotone systems with inputs and outputs [9], which made it possible to develop a general interconnection theory. The paper [9] established global stability results for monotone systems under negative feedback. That work was undertaken to address a specific question concerning the robustness of stability and dynamical responses in a signaling context involving mitogen-activated protein (MAPK) cascades. MAPK proteins form a family of enzymes that relay signals from the cell surface to the nucleus and regulate essential cellular processes such as proliferation, differentiation, and survival. The MAPK signaling pathway plays critical roles in normal physiology and is also a major contributor to disease states, including cancer, where its dysregulation motivates several therapeutic interventions. The approach was further developed in [7, 39]. The embedding procedure also forms the basis of a widely used method for estimating reachability regions and providing safety guarantees [31] in the framework of mixed monotone systems, as surveyed in [30].

Let us illustrate a typical result in this setting. Suppose we have two systems with scalar inputs and outputs, with $\mathbb{U}_1 = \mathbb{Y}_2 \subseteq \mathbb{R}$ and $\mathbb{U}_2 = \mathbb{Y}_1 \subseteq \mathbb{R}$. Each system is assumed to be monotone and to possess a well-defined *characteristic*, denoted $k_i(u)$, which is an analog of a “DC gain” but understood in the nonlinear monotone-systems sense of a characteristic map. By this we mean that for every constant input u , there exists a unique equilibrium state $x_u \in \mathbb{X}$ and that this equilibrium is globally asymptotically stable for the system $\dot{x} = f(x, u)$ with that fixed input. The characteristic is defined as the function $k(u) := h(x_u)$. Depending on the biological context, such functions k may be referred to as “signal versus input concentration curves,” “dose-response curves,” “receptor activity plots,” or other similar terms. See Figure 15.

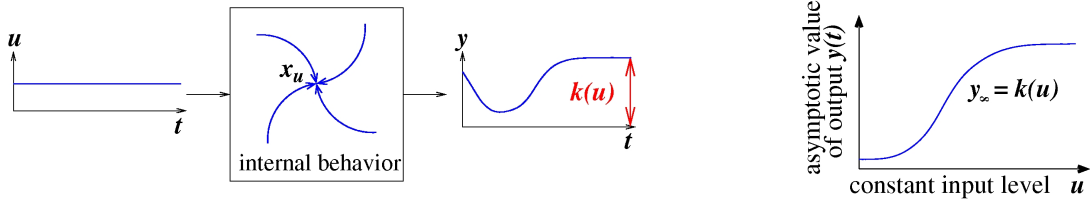


Figure 15: Defining characteristic k , from [9]. For each constant input u , there is a unique steady state x_u , which is GAS, and $k(u) := h(x_u)$. A plot of a typical k is shown, with $\mathbb{U} = \mathbb{Y} = [0, \infty)$ endowed with the usual order from \mathbb{R} .

We will study a *negative feedback* interconnection of two systems, we take the orders on states, inputs, and

outputs of the first system to be the usual order on \mathbb{R} , but for the second system we impose instead the reverse order on outputs. For example, consider a system with $\mathbb{U} = \mathbb{X} = \mathbb{Y} = (0, \infty)$, dynamics $\dot{x} = 1 - x + u$, and output $y = \frac{1}{1+x}$. This system is monotone when the reverse order is used on \mathbb{Y} , because the output function is non-increasing. In general, for monotone systems, the characteristic can be shown to be monotonic with respect to the chosen orders. Thus, k is a non-decreasing function when the usual orders are used, and it is non-increasing when a reversed order is imposed on outputs. We now informally state one of the main theorems from [9]. That paper should be consulted for full details and for the more general formulation that allows arbitrary input and output spaces and arbitrary orders on these spaces. The theorem, illustrated in Figure 16, provides a sufficient condition for global asymptotic stability (GAS) to a unique equilibrium of a negative feedback configuration. We call k the characteristic of the first system and g the characteristic of the second system. We may assume in the theorem that the g characteristic is just a mapping, not necessarily arising from a nontrivial system, which allows one to include static feedback laws. The sufficient condition for GAS is that the discrete one-dimensional “spider-web”iteration:

$$u_{i+1} = (g \circ k)(u_i)$$

should globally converge to a unique fixed point (denoted \bar{u} in the figure). This condition can be interpreted as a contraction-type small-gain theorem for monotone systems. A key ingredient in the proof is a property that is also useful for understanding transient behaviors: in monotone systems, bounded inputs cause trajectories to eventually remain within suitable “safe” multidimensional order intervals in $\mathbb{X} \subset \mathbb{R}^n$, with the size of these intervals determined by the bounds on the input.

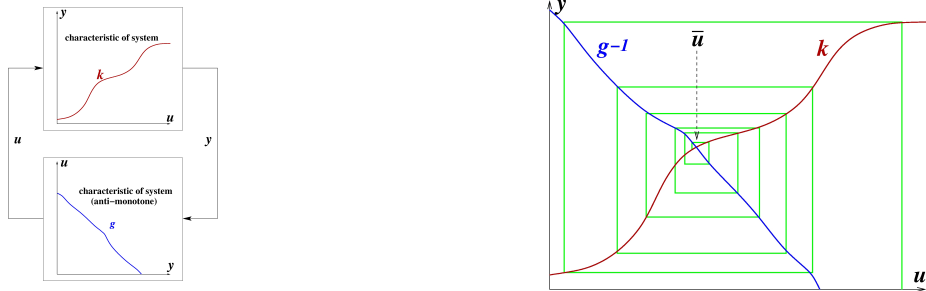


Figure 16: Two systems in a negative feedback configuration, and a convergent one-dimensional iteration.

We remark, and this will be used below in an example, that stability is guaranteed even in the presence of arbitrary delays (even time-varying) in the feedback, so that the overall system becomes a delay-differential system; see [41]. The result can also be generalized to certain partial differential equations that include diffusion effects, as often encountered in biological applications [39].

Example negative feedback interconnection: a testosterone model. Circulating testosterone in healthy adult males exhibits multi-hour rhythmic fluctuations driven by corresponding pulses of luteinizing hormone (LH) from the pituitary and of luteinizing hormone-releasing hormone (LHRH) from the hypothalamus (see [26],[112]). A classical model presented in [86] accounts for these oscillations using a system of delay-differential equations. In this model, LHRH stimulates the production of LH, LH in turn triggers testosterone synthesis in the testes (after a delay τ), and testosterone feeds back to inhibit further release of LHRH. Writing $R(t)$, $L(t)$ for the concentrations of LHRH and LH at time t , and $T(t)$ for the concentration of testosterone at time $t + \tau$, and assuming first-order degradation, the model takes the following negative

feedback form:

$$\begin{aligned}\dot{T} &= \alpha_2 L - \beta_3 T & \text{testosterone} \\ \dot{L} &= \alpha_1 R - \beta_2 L & \text{luteinising hormone} \\ \dot{R} &= u - \beta_1 R & L\text{-releasing hormone}\end{aligned}$$

where $u(t) = g(t - \tau)$ and $\tau > 0$ is a delay. Here, g is the function $g(t) = \frac{A}{K+T(t)}$, thought of as a system with no dynamics. We regard the system as a monotone linear subsystem with input u and output T , whose characteristic is

$$k(u) = \frac{\alpha_1 \alpha_2}{\beta_1 \beta_2 \beta_3} u,$$

placed in feedback with g . The composition $g \circ k$ is a simple fractional map of the form

$$S(u) = \frac{p}{q + u}, \quad p, q > 0.$$

It is straightforward to verify that every map of this type has globally convergent iterates with a unique fixed point. Hence, by the theorem, oscillations cannot occur—regardless of the delay. This contradicts the result in [86], which asserts the existence of oscillations for certain delay values. Somewhat ironically, although monotone systems theory yields the non-oscillation result almost immediately, identifying the flaw in the proof of [86] required substantial effort; see [40].

3 Non-monotone systems: responses, motifs, and model discrimination

A system is monotone with respect to an orthant order precisely when its signed graph has no negative cycles after edge orientations are ignored. In particular, any two directed paths connecting the same pair of distinct nodes, a *feedforward (FF)* motif, must carry the same sign, and every directed cycle, a *feedback (FB)* motif, must have a positive sign. Feedforward motifs are especially common in biological networks, including intracellular systems (metabolic, signaling, and gene-regulatory networks) as well as intercellular interactions; see [5]. We classify FF (respectively, FB) motifs as *coherent* if the two paths share the same sign (respectively, the loop has positive sign), and *incoherent* otherwise. Accordingly, we use the abbreviations CFF and IFF for coherent and incoherent feedforward motifs, and CFB and IFB for coherent and incoherent feedback motifs. (We also use the term “negative feedback loop” instead of “IFB.”) Examples are shown in Figure 17.

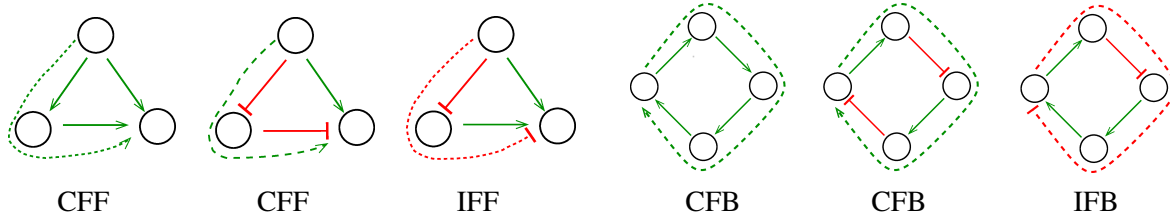


Figure 17: Examples of Coherent and Incoherent FeedForward/FeedBack motifs

The following result is instrumental in helping to invalidate putative biological mechanisms. The proof is based on monotone systems theory, but requires additional considerations because it only talks about directed paths. The precise statement is from [16], and rely heavily upon an earlier version of the result given in [12]. We summarize below (for simplicity, only for scalar inputs and outputs):

Biphasic responses as signatures of IFF's or IFB's. Suppose that all the directed paths from the input node to the output node have a positive (respectively negative) net sign. Consider an input u that is monotonically increasing in time, and an initial state which is an equilibrium state for the input value $u(0)$. Then the output will monotonically increase (respectively), decrease in time. For inputs that are decreasing, the conclusions reverse.

The proof is not easily found in self-contained form, so we provide a sketch in Appendix A.

Another way of stating the conclusion is that a non-monotonic (biphasic, bell-shaped) response to a monotonic input (for example, a step) *requires* a negative feedback and/or an incoherent feedforward motif, see Fig. 18.

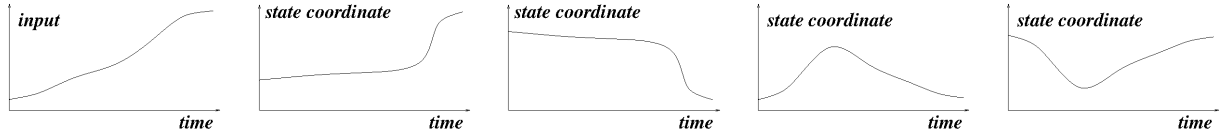


Figure 18: Left to right: monotonic input; two possible state behaviors; two impossible behaviors, as the response is biphasic, unless there is a negative feedback and/or an incoherent feedforward motif in the graph.

Example of IFF providing a biphasic response. A clear illustration of the effect of an incoherent feed-forward (IFF) motif can be drawn from the regulatory architecture studied experimentally by Kaplan *et al.* [63]. See Figure 19. Although several operons in the *gal* regulon share the same underlying regulatory logic, the experiments in that work monitored expression of the *galP* promoter—a gene encoding the galactose permease responsible for importing galactose into *E. coli*. The *galP* promoter is jointly regulated by two transcription factors that respond to cAMP: the activator CRP (complexed with cAMP) and the galactose-responsive repressor GalS. CRP directly activates expression from the *galP* promoter, but it also activates *galS*, whose product represses *galP*. These two paths—one activating and one repressing—form an IFF motif with a built-in delay in the negative branch. (The same architecture also governs the *galETK* operon, but *galP* provides a cleaner and more experimentally robust readout, which is why it appears in the figure.) When galactose is present, GalS is able to act as an effective repressor. Under this condition, a step increase in cAMP produces the characteristic biphasic IFF response: a rapid rise in expression from direct CRP activation, followed by a slower decline mediated by CRP-induced synthesis of GalS (blue curve in Figure 19). The red dashed curve reflects the activating effect of CRP on *galS*, confirming the positive sign of that regulatory edge. To test whether the IFF structure was indeed responsible for the biphasic behavior, the authors examined conditions in which GalS is not functionally active—for example, in the absence of galactose, where the repressive branch becomes ineffective. In this regime, the indirect negative path is removed, leaving only direct CRP activation, and the response becomes monotonic (green curve), exactly as predicted when the IFF motif is disabled.

An example of model invalidation. Regulation by the sigma factor σ^E plays a key role in the hypoxic stress-response pathway of *M. tuberculosis*, and in particular modulates the expression of two central metabolism genes, *icl1* (Rv0467, glyoxylate shunt) and *gltA1* (Rv1131, methylcitrate cycle), both of which contribute to the persistence of tubercle bacilli during infection. Transcription of *icl1* requires σ^B , itself transcribed under σ^E control, as well as the σ^B -dependent transcription factor *lrpI* (Rv0465c), a local regulator of *icl1*. The resulting regulatory architecture (see [35]) forms a coherent feedforward loop, illustrated in the graph shown in Fig. 20. Because this circuit contains neither feedback loops nor incoherent feed-forward branches, a monotone increase in σ^E activity should, in principle, produce a monotone increase

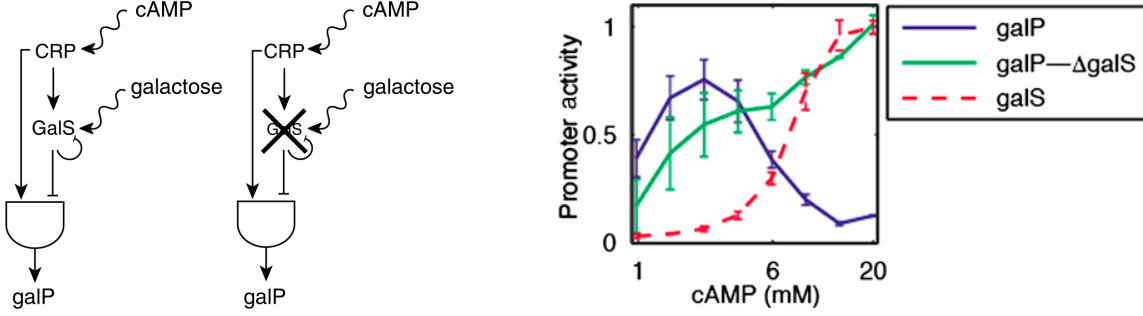


Figure 19: IFF-mediated biphasic response in *galP* in *E. coli*. Figures adapted from [5] and [63].

in *icl1* expression. However, experiments in which oxygen levels are gradually depleted over a three-day period show that *icl1* expression is biphasic, rather than monotone, despite the concomitant monotone rise in σ^E activity (plot in Fig. 20, adapted from [106]). This inconsistency between the predicted and observed behavior motivated the search for alternative regulatory architectures in [16].

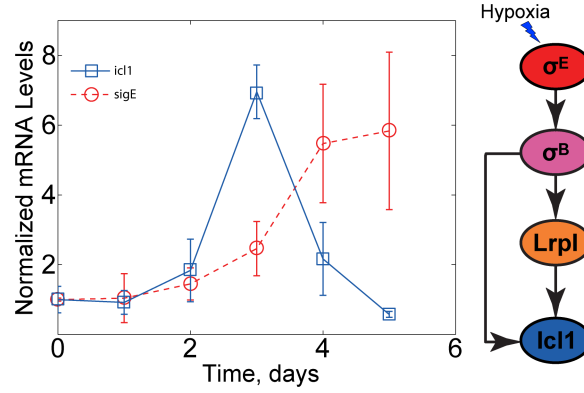


Figure 20: Experimental σ^E and gene expression dynamics from [35] showing biphasic response and therefore inconsistent with network from [106] shown on right.

3.1 Transient responses followed by sensory “perfect adaptation”

An ubiquitous feature of biological sensory and regulatory systems is *(perfect) adaptation*: a sudden increase in an external stimulus elicits a rapid transient response, such as activation of a signaling cascade or induction of a gene, followed by a slower relaxation back toward the original pre-stimulus level. Thus, even under a sustained stimulus, the system ultimately “resets” its output. Adaptation is crucial for maintaining key variables within physiological bounds and for ensuring that cells and organisms remain sensitive to *changes* in their environment rather than being overwhelmed by constant background signals. Mathematically, we mean that, for constant (step) inputs, outputs are not identically zero, but after a transient recover asymptotically to their steady state value; see for example [114] for a precise definition. Since adaptation to a step (thought of as a nondecreasing function that starts at $u = 0$ at time $t = 0$ and then increases, and assuming an equilibrium initial state), this means that we have a non-monotonic response. Thus, we have the following principle:

Adaptation as a signature of IFF’s and IFB’s. An adapting system requires a negative feedback and/or an incoherent feedforward motif.

Perfect adaptation is quite common in biology. In bacterial chemotaxis, *E. coli* receptors transiently signal upon a step increase in attractant, but biochemical modification systems restore the signaling state to baseline. Sensory neurons in vision and olfaction adapt to background light or odor so that new stimuli can still be detected. Hormonal and immune systems similarly employ adaptive responses to prevent chronic overstimulation. Gene-regulatory networks also display adaptive pulse-like dynamics, often arising from characteristic circuit motifs. Figures 21, 22, and 23, show experimental data respectively showing adaptation at many different biological levels, from bacteria, to yeast (a single-cell eukaryote), to human immune cells.

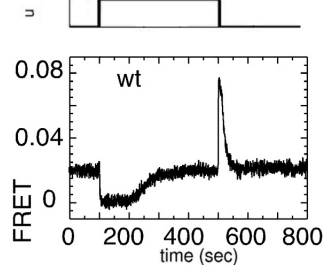


Figure 21: Adaptive response in the *E. coli* chemotaxis pathway, measured *in vivo* by fluorescence resonance energy transfer (FRET). Stepwise addition and subsequent removal of attractant (methyl-aspartate, MeAsp) are applied to cells expressing CFP–FliM and CheY–YFP fusion proteins. CheY is the phosphorylated response regulator that conveys chemotactic signals from the receptor kinase cascade to the flagellar motor by binding to the motor switch protein FliM. YFP and CFP (yellow and cyan fluorescent proteins) serve as the FRET donor and acceptor pair, allowing real-time monitoring of the interaction between CheY~P and FliM *via* energy transfer efficiency. The resulting FRET signal reports the fraction of motor-bound CheY~P. Following each step change in stimulus, the signal exhibits a rapid transient response and then relaxes back toward its prestimulus level despite sustained input, demonstrating near-perfect adaptation of the chemotaxis signaling output. Adapted from Fig. 1B of [123].

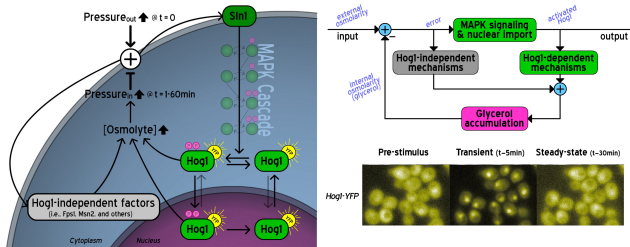


Figure 22: Perfect adaptation in the yeast HOG pathway through an integral-feedback module. Following hyperosmotic shock, the MAP kinase Hog1 rapidly translocates to the nucleus, triggering transcriptional and metabolic responses that promote glycerol production. As osmotic balance is restored, Hog1 returns to its pre-stimulus cytosolic distribution despite sustained elevated external osmolarity, demonstrating near-perfect adaptation. The paper [87] showed that this behavior requires a single internal integrator located downstream of Hog1 and upstream of glycerol accumulation, forming an effective integral-feedback control loop that restores turgor pressure. Figure adapted from [87].

From a control-theoretic perspective, *integral feedback* is a classical and powerful mechanism for achieving perfect adaptation. Widely used in engineering, it ensures that any deviation from a desired baseline level

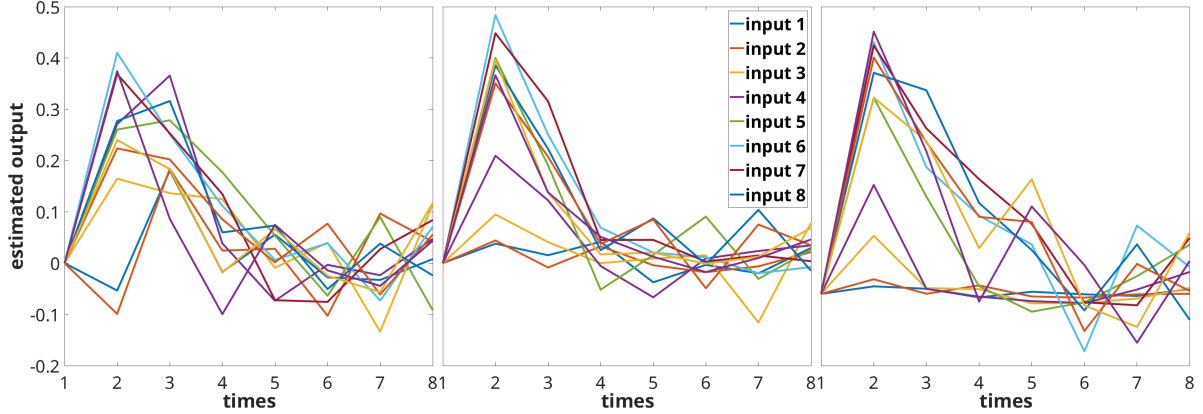


Figure 23: An experimental demonstration of perfect (or near-perfect) adaptation in a mammalian system. Human CD8⁺ T cells were subjected to constant antigen stimulation over many hours. Cytokine production exhibited a transient activation pulse followed by a return to near-baseline levels despite the continued presence of antigen. Shown are three independent experiments, each performed over eight distinct input magnitudes. The figure was generated from data reported in [132], and is discussed in more detail below.

is continuously accumulated and counteracted, eventually driving the steady-state error to zero. Biological circuits such as bacterial chemotaxis and certain homeostatic modules employ integral feedback-like architectures, providing robust and precise restoration to baseline even in the presence of parameter uncertainty or environmental variability [66]. In synthetic biology, biomolecular integral controllers that precisely regulate target gene expression so as to track externally imposed reference levels, even in the presence of disturbances, have been experimentally demonstrated both in living cells and in cell-free *in vitro* systems; see e.g. [2, 13].

A distinct mechanism for adaptation arises from *incoherent feedforward* (IFF) motifs, in which an input activates a target through one pathway while simultaneously activating a second pathway that represses the same target after a delay. This architecture produces an initial activation pulse followed by a return toward baseline and is common in transcriptional networks, allowing rapid and sharply timed responses without an explicit “integrator” component.

Each mechanism has characteristic advantages and limitations. Integral feedback is exceptionally robust and guarantees return to baseline despite fluctuations or uncertainty, though it may respond more slowly and often requires additional molecular components to implement the effective integration. IFF motifs, in contrast, are compact and can generate fast, transient responses, but their adaptation is generally less robust: the degree of return to baseline depends on parameter balances and is not structurally guaranteed. Both strategies are therefore pervasive in biology, reflecting different trade-offs among robustness, speed, metabolic cost, and biochemical simplicity.

Under suitable technical assumptions and for certain classes of systems, the *Internal Model Principle* (IMP) guarantees that any system exhibiting perfect adaptation must incorporate, in some form, an *integral-feedback mechanism*, possibly after an appropriate nonlinear change of coordinates. However, when interpreting biological circuits in terms of *network motifs*, such coordinate transformations generally alter the network structure itself, obscuring the direct correspondence between the abstract IMP guarantee and specific biochemical architectures. As a result, the practical significance of the IMP for motif-based biological analysis is not always clear; see the discussion in [19, 108].

A synthetic biology example of adaptation. Not all negative feedback mechanisms yield perfect adaptation. In linear systems, perfect adaptation to step inputs is equivalent to the presence of an integrator, or, equivalently, a zero at the origin of the transfer function. Purely static (memoryless) negative feedback, even when applied with high gain, cannot generically enforce adaptation. This distinction is illustrated experimentally in [21], which contrasts synthetic gene circuits implementing static negative feedback with incoherent feedforward (IFF) architectures that effectively realize integral control. The motivation in [21] is the need for natural and synthetic biological networks to operate reliably under fluctuations in the stoichiometry of their molecular components, such as variability in gene copy number or expression efficiency. From a control-theoretic perspective, the question is whether the steady-state output can be made insensitive to such constant disturbances. The experiments show that while static negative feedback reshapes the steady-state input–output map, only IFF-based circuits achieve true adaptation, namely steady-state insensitivity of the output to changes in input amplitude.

The negative-feedback genetic circuit studied in [21] is shown in Figure 24 (right), with corresponding interaction and phenomenological diagrams in the middle and left panels. The phenomenological description assumes transcription is fast relative to translation, so that the protein product represses its own production rate. The measured output y (ZsGreen fluorescence) is proportional to the concentration of the self-repressing protein (LacI), while the input u is proportional to plasmid copy number and is reported by DsRed fluorescence.

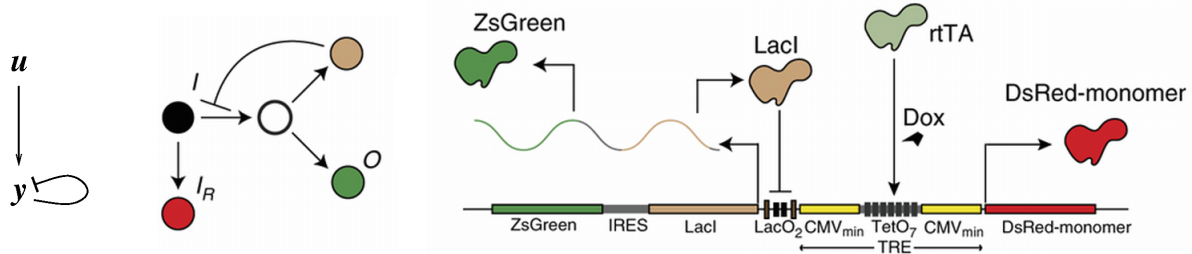


Figure 24: Transcriptional negative autoregulation motif (tAM), adapted from Figure 1D of [21]. Left: phenomenological static feedback representation. Middle: interaction diagram of the genetic circuit (I = input, I_R = input reporter, O = output). Right: genetic implementation; LacI represses its own transcription and that of the cotranslated ZsGreen reporter. The input is reported by a divergently expressed DsRed protein. The transcription factor rtTA is present at constant, non-limiting levels and is not treated as a system input.

A minimal phenomenological model for this circuit is the scalar nonlinear system

$$\dot{y} = \frac{Mu}{1 + Ly} - \delta y,$$

where u denotes the input, y the output, L the static feedback gain, M the efficiency of transcription and translation, and δ the degradation rate constant. While more detailed dynamical models are analyzed in [21], this simple equation already captures the essential steady-state behavior. At equilibrium, y satisfies

$$Ky^2 + dy - u = 0$$

where $d := \delta/M$ and $K := Ld$. For the subsequent analysis, we keep d constant but think of K as a parameter, and write $y = f_K(u)$ for the positive solution of the quadratic. A Taylor expansion for small K yields

$$f_K(u) = \frac{-d + d \left(1 + \frac{2Ku}{d^2} + O(K^2)\right)}{2K} = \frac{u}{d} + O(K).$$

so that in the limit of vanishing feedback strength,

$$\lim_{K \rightarrow 0^+} f_K(u) = \frac{u}{d}.$$

Thus, in the absence of repression, the steady-state input–output map is linear, and no adaptation is present. In the opposite regime of strong static feedback ($K \rightarrow +\infty$), asymptotic expansion gives

$$f_K(u) = \sqrt{\frac{u}{K}} - \frac{d}{2K} + O\left(\frac{1}{K^{3/2}}\right),$$

so that

$$f_K(u) \sim \sqrt{\frac{u}{K}}.$$

Hence, increasing the feedback gain does not eliminate dependence on the input; it merely compresses the static input–output nonlinearity from linear to sublinear (square-root) scaling. From a control perspective, this behavior is characteristic of high-gain static feedback: sensitivity is reduced but cannot be driven to zero. In contrast, integral feedback, as effectively implemented by the IFF architectures in [21], introduces internal state accumulation, enforcing zero steady-state sensitivity to constant disturbances and thereby guaranteeing perfect adaptation, in accordance with the internal model principle.

Equivalently, plotting $\log y$ versus $\log u$, the static-feedback model predicts a slope close to 1 for weak repression and approaching 1/2 for strong repression, but never zero. This prediction is confirmed experimentally in Figure 25, where three repression levels yield slopes ranging from near 1 to near 0.5. About 200,000 cells were measured in each experiment, and the means and standard deviations are shown for each of the three. The key plot is the right one, showing a log–log plot of linear fits. We see that, as predicted, the slopes range from near 1 to near 0.5.

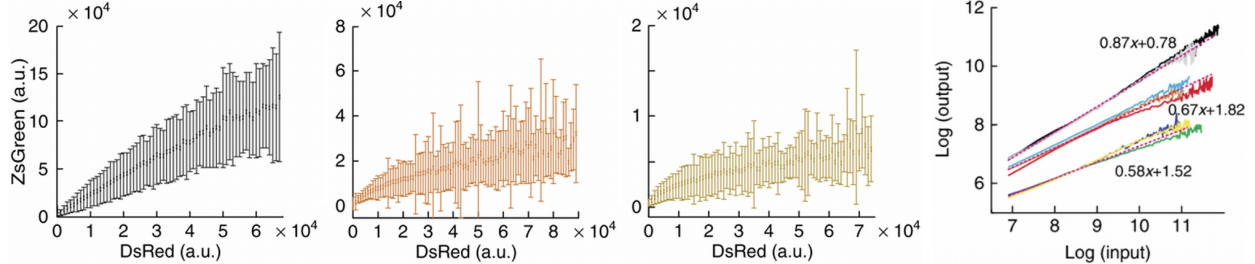


Figure 25: Experimental characterization of transcriptional autoregulatory motifs (tAM), adapted from Figure 5 of [21]. Flow cytometry measurements were obtained from at least 200,000 cells per condition. The first three panels correspond to increasing repression strength (IPTG-interfered LacI binding, single LacO site, and double LacO repeat). Right: log–log plots of mean output versus input, showing slopes decreasing from near 1 to near 0.5 as repression strength increases.

Several IFF genetic circuits were studied in [21]. As an illustrative example, we describe the post-transcriptional type-I incoherent feedforward loop (ptI1-FFL) circuit from that reference, shown in Figure 26. The left panel shows a phenomenological representation, while the second panel depicts the interaction structure among the biological components. The two rightmost panels show the corresponding genetic implementations: the full circuit, followed by a variant in which the regulator (“A” in the interaction diagram, “ x ” in the phenomenological model) does not repress the output (“ O ” or “ y ”).

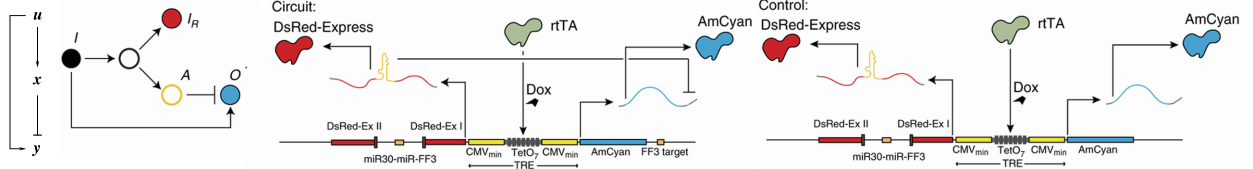


Figure 26: Post-transcriptional type-I incoherent feedforward loop (ptI1-FFL) circuit, adapted from Figure 1B of [21]. Left: phenomenological representation. Middle: interaction diagram of the genetic circuit (I = input, I_R = input reporter, A = auxiliary regulator, O = output). Right: genetic implementations. The regulated output protein is AmCyan. The auxiliary repressor (node x in the phenomenological diagram) is a synthetic microRNA, miR-FF3, which targets a complementary RNA sequence engineered into the 3'-UTR of the AmCyan mRNA, thereby repressing AmCyan expression at the post-transcriptional level. The microRNA miR-FF3 is co-expressed and processed post-splicing from an intron inserted between two exons encoding the fluorescent protein DsRed-Express. DsRed-Express serves as an internal reporter of plasmid copy number and is used as a proxy for the input u . As a biological control to test the necessity of repression, a variant of the circuit omits the miR-FF3 target site in the AmCyan transcript, thereby eliminating RNA-interference-mediated repression. The transcription factor rTA is present at constant, non-limiting levels and is not treated as a system input.

A detailed model is analyzed in [21]. For physiologically relevant plasmid copy numbers, however, a suitable minimal phenomenological description of the conceptual system in Figure 26 is given by the two-dimensional nonlinear system

$$\begin{aligned}\dot{x} &= -\delta x + Mu \\ \dot{y} &= \frac{Nu}{1+Kx} - \varepsilon y,\end{aligned}$$

where the parameters have their natural interpretations. At steady state,

$$y = \frac{Vu}{1+Ku},$$

where $V := N/\varepsilon$ and $K := LM/\delta$. The parameter K thus acts as a proxy for the strength of the repressive regulation of x on y . In the unrepresed case ($K = 0$), the steady-state output y is proportional to the input u . In contrast, in the strongly repressed regime ($K \gg 1$), the output saturates at the constant value $y \approx V/K$ for all but very small inputs. Thus, unlike static negative feedback, the ptI1-FFL architecture achieves effective adaptation by rendering the steady-state output insensitive to input magnitude over a wide dynamic range. These predictions are confirmed experimentally in Figure 27.

3.2 Distinguishing between adaptation topologies: Response to periodic inputs

One challenging question in systems biology is that of comparing different architectures for perfect adaptation. We concluded that a system which perfectly adapts to step inputs must contain at least one incoherent feedforward (IFF) or feedback (IFB) motif. Beyond this, little can be inferred from step-response adaptation alone, which naturally raises the question: how can one distinguish between these two possibilities? One possibility is to use of periodic signals to discriminate between these models. The paper [95] provided the following principle:

Subharmonics as a signature of IFB's. Suppose that the input is T -periodic.

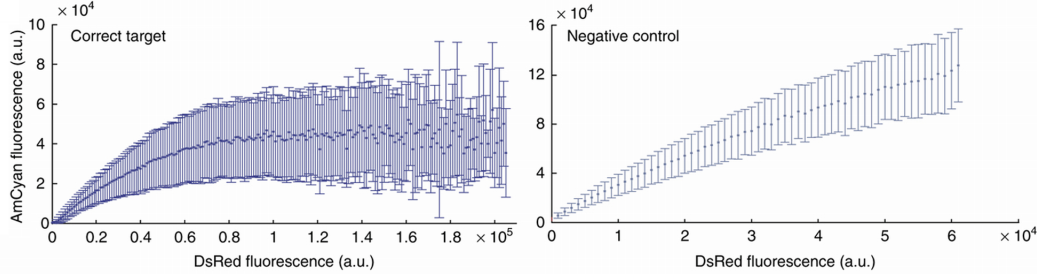


Figure 27: Experimental results obtained with ptI1-FFLI motif. Figures adapted from [21] Figures 4A and 4B. Left: original circuit with repression, exhibiting saturation of the output at moderate input levels. Right: comparison circuit without repression, showing an approximately linear input–output relationship. Flow cytometry measurements, including means and standard deviations, are shown for approximately 200,000 cells in each condition.

- For feedforward systems, solutions are eventually periodic with the same period T (“entrainment”).
- For monotone systems, if the solution starting at an initial state $x(0)$ converges to a periodic solution $z(\cdot)$ of period kT , with k a positive integer and $x(0) \preceq z(t)$ for all t , then necessarily $k = 1$.

We do not state a formal theorem, because there are several technical points to be precise about. For example, feedforward systems are restricted to those that can be written as a cascade of one-dimensional systems with appropriate stability properties similarly to the systems analyzed in [102]. For details, see [95] and Appendix B.

The above principle is often summarized as follows: if a system adapts to constant inputs, but exhibits a *subharmonic response*, that is to say, a response with a frequency that is a submultiple of the forcing frequency, then its underlying network must contain a negative-feedback mechanism. Observe that *subharmonic responses are a strictly nonlinear phenomenon*, since linear (stable) systems always entrain. We conclude that non-entrainment to inputs is one “signature” of a nonlinear negative feedback loop in the system. In other words, *testing with periodic inputs* provides a means to distinguish IFF motifs from incoherent feedback (IFB) architectures, or to be more precise to identify situations in which some negative feedback must be present. It is well known in classical dynamical systems theory that negative feedback can generate subharmonics, period-doubling bifurcations, and even chaotic dynamics, as in the forced van der Pol oscillator. It is perhaps surprising is that analogous phenomena can arise even for very simple periodically forced biochemical networks [88]. In fact, one can even give examples of systems with the property that when the external input is constant, all solutions converge to a steady state, yet with the input $u(t) = \sin t$ solutions become chaotic [116]. It is worth noting that monotone systems (at least under a natural irreducibility assumption) may lead to subharmonics, as it is known (Těšcák’s Theorem) that, when forced by T -periodic inputs, solutions will generically converge to kT -periodic solutions with k possibly > 1 . The additional condition that $x(0) \preceq z(t)$, which is satisfied if for example we start at rest ($x(0) = 0$) and solutions are positive for $t > 0$, rules out such subharmonic solutions.

As an application of this principle, consider the following experiment. The worm *C. elegans* can locate odor sources across a 100,000-fold concentration range, and various sensory and interneurons participate in the recognition pathway, see Fig. 28. The paper [95] discussed how the above theorems can be used to rule out IFF motifs as (solely) responsible for adaptation in a local circuit controlling the AWA sensory neuron, leading to the postulation of a negative feedback model. This is because at high frequencies of inputs, one does not obtain entrainment, see Fig. 28(top right panel and bottom).

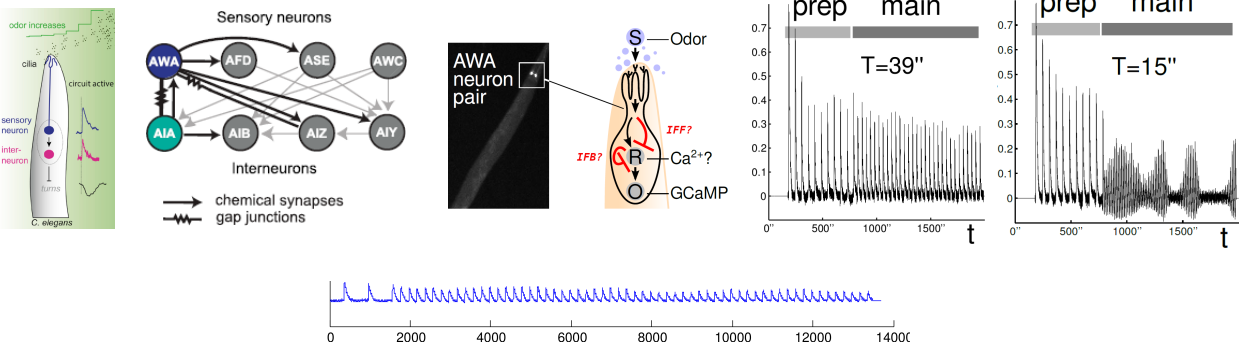


Figure 28: Odor sensing in *C. elegans* and sensory/interneurons. Top, left to right: Location of sensory and interneurons, network connections, and possible IFB or IFF mechanisms, and testing for odor-evoked intracellular Ca^{2+} response signature via periodic on-off pulses of diacetyl, population measurements shows Entrainment at high periodic inputs, on/off steps of duration 10s: low frequency, period $T = 39\text{s}$ shows entrainment but higher frequency, lower period $T = 15\text{s}$ shows subharmonic behavior. Bottom: single-neuron recording with high frequency, period $T = 20$, gives response with period about ~ 200 , indicating that IFF's (or positive feedback systems) cannot be the reason for behavior. Figures adapted from [71] and [95].

4 Weber's Law, scale invariance, and log sensing

In the 1840s, Ernst Weber, a pioneer of psychophysics, investigated the relationship between the physical magnitude of a stimulus and its perceived intensity. He observed that the *just noticeable difference* (JND) in a stimulus variable u is not an absolute quantity but scales proportionally with the stimulus itself, so that perception is sensitive to fractional changes $\Delta u/u$. This empirical observation is now known as *Weber's law*. Gustav Fechner subsequently proposed a mathematical interpretation of Weber's law, arguing that perceived sensation is proportional to the logarithm of stimulus intensity. This led to the classical *Weber–Fechner law*, which may be expressed as a logarithmic relationship between physical and perceived quantities. In effect, *sensory systems respond to changes in $\log u$ rather than to changes in u itself* (“*logarithmic sensing*”). Typical Weber fractions reported in psychophysical experiments include: $\approx 1/40$ for lifted weight discrimination, $\approx 1/10$ for pitch perception, $\approx 1/16$ for light intensity, $\approx 1/4$ for odor intensity, $\approx 1/30$ for pain perception, and $\approx 1/3$ for taste.

Another way to express sensitivity to changes in $\log u$ is to view it as an invariance with respect to multiplicative scaling of the input by positive constants. Consider an input that switches from a value u to a value v , and the system's response to this change. Now suppose that both values are multiplied by a factor $p > 0$, so that the input changes from pu to pv . The corresponding change in the logarithmic scale is

$$\log(pv) - \log(pu) = \log v - \log u,$$

which is identical to the original increment. In other words, sensing on a logarithmic scale makes the response independent of the absolute magnitude of the stimulus and sensitive only to relative changes. This property is therefore referred to as *scale-invariant* sensing. An equivalent formulation is that the system is able to detect at most *fold changes* of the input, since $pv/pu = v/u$. For this reason, the phenomenon is also known as *fold-change detection* (FCD). Scale-invariant sensing is useful because it renders system responses independent of measurement units and provides robustness to multiplicative uncertainties in stimulus intensity. Figure 30(left) illustrates a series connection in which an “upstream” system is subject to multiplicative uncertainty and a “downstream” system has a response that is invariant to scale,



Figure 29: Sensing.

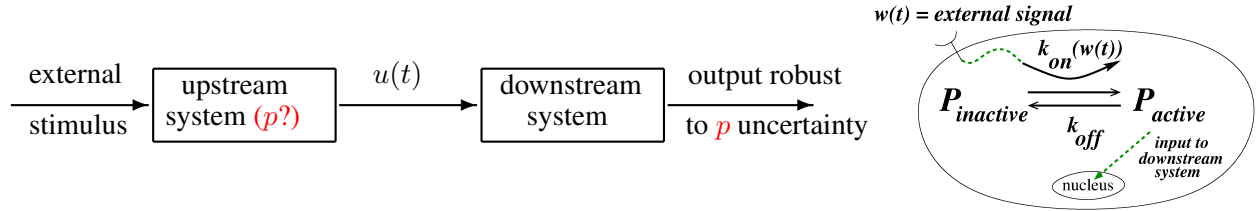


Figure 30: Robustness to multiplicative uncertainty

A typical example from cell signaling is the following. Suppose that a signaling protein can switch between an inactive form P_{inactive} and an active (for example, phosphorylated) form P_{active} . The rate of activation, mediated by kinase action, is denoted

$$a(t) = k_{\text{on}}(w(t)),$$

where $w(t)$ is an external signal. Inactivation occurs with constant rate k_{off} , independent of w . See Figure 30 (right). Assume that the total protein concentration is conserved,

$$P_{\text{inactive}}(t) + P_{\text{active}}(t) = p = P_T.$$

Let

$$u(t) = P_{\text{active}}(t), \quad P_{\text{inactive}}(t) = p - u(t).$$

Then the dynamics of the active form are described by the linear, time-varying system

$$\dot{u}(t) = a(t)(p - u(t)) - k_{\text{off}}u(t), \quad u(0) = 0.$$

This may be viewed as a linear system with constant input p :

$$\dot{u}(t) = -(k_{\text{off}} + a(t))u(t) + a(t)p.$$

Therefore, the solution $u(t)$ scales proportionally with the total protein concentration p . An equivalent way to express this proportionality is in terms of fold changes. Fix two times t_1 and t_2 and consider the ratio $r := u(t_2)/u(t_1)$. If the total protein level is changed from p to \hat{p} , and $\hat{u}(t)$ denotes the corresponding solution of the ODE, then

$$\hat{r} := \frac{\hat{u}(t_2)}{\hat{u}(t_1)} = r.$$

Thus, this model predicts invariance of fold changes with respect to scaling of p . If the initial condition is nonzero, this conclusion requires that $\hat{u}(0)$ be scaled in proportion to p , as would naturally occur when trajectories are initialized at steady state.

The active protein, which typically functions as a transcription factor or signaling intermediate, often serves as the input to a downstream genetic or signaling network. We conclude that the downstream response to $w(t)$ will be robust to uncertainty in the upstream protein abundance $p = P_T$ precisely when the downstream network exhibits *scale-invariant* behavior. In practice, total protein concentrations such as p often vary substantially from cell to cell. Hence, scale invariance of the downstream network is required in order for the overall system response to remain independent of these fluctuations. We summarize this informally:

Robustness to multiplicative uncertainty as a signature of FCD. If a downstream genetic or signaling system exhibits consistent responses to a given external excitation despite variations in upstream protein abundances, then the system likely possesses the scale-invariance property, also known as fold-change detection (FCD).

Recent interest in fold-change detection (FCD) in signaling pathways was largely stimulated by two influential studies published in 2009 [29, 44]. These works reported that signaling outputs may be insensitive to the absolute concentrations of pathway components and instead respond primarily to *relative (fold) changes* in key signaling molecules. Such behavior was demonstrated experimentally in the canonical Wnt/β-catenin pathway [44] and in the EGF-ERK pathway [29]. See Figure 31(left) for the Wnt pathway. Both pathways are highly conserved in eukaryotes and play essential roles in embryonic patterning, stem-cell homeostasis, cell proliferation, and tissue maintenance. Notably, dysregulation of Wnt signaling is strongly linked to multiple cancers, particularly colorectal carcinoma.

In the Wnt study of Goentoro and Kirschner [44], the authors examined how cellular responses depend on nuclear β -catenin (which we think of as $u = P_{active}$), the transcriptional effector of canonical Wnt signaling. Under Wnt stimulation, β -catenin is stabilized through inhibition of the destruction complex, enabling its accumulation and activation of target-gene transcription. To vary absolute protein abundance ($p = P_T$, they applied independent perturbations, including pharmacological inhibition of GSK3 β using BIO or lithium chloride, RNA-mediated overexpression of β -catenin, and manipulation of the degradation machinery via overexpression of the scaffold protein Axin1. These experiments were conducted in *Xenopus* embryos and in cultured RKO colorectal carcinoma cells, with pathway output assessed through developmental phenotyping and quantitative RT-PCR measurements of canonical Wnt target genes including *siamois* and *Xnr3*.

Across an approximate four-fold range of basal β -catenin perturbations, the authors observed substantial variation in *absolute* protein levels, while the Wnt-induced *fold-change* in nuclear β -catenin remained nearly constant. Correspondingly, downstream gene expression and developmental phenotypes remained indistinguishable from wild type whenever fold changes were preserved. For example, embryos treated with lithium or injected with β -catenin RNA exhibited roughly two-fold increases in absolute protein concentration, yet expression of *siamois* and *Xnr3* remained at wild-type levels. In contrast, perturbations that altered the magnitude of the Wnt-induced fold change, such as strong modulation of Axin1 expression affecting β -catenin degradation rates, led to aberrant signaling outputs and abnormal phenotypes. See Figure 31(right). These findings provided compelling experimental support for fold-change detection as a governing principle of Wnt signal transduction.

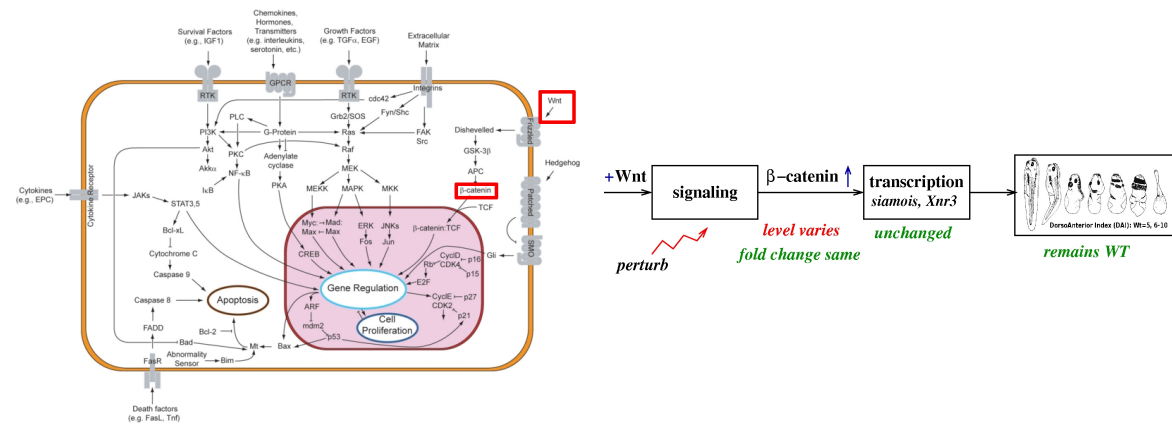


Figure 31: Wnt signaling pathway and Goentoro and Kirschner's experiments. Left figure adapted from Wikipedia. Red rectangles show Wnt external ligand and β -catenin (whose concentration is highly variable).

Formalizing scale-invariance. As illustrated in Figure 32, perfect adaptation requires only that the system output eventually return to its pre-stimulus value after a change in input. The stronger property of *fold-change detection* (FCD) demands more: the entire temporal response, including both amplitude and timing,

must be preserved whenever two inputs differ by a multiplicative constant. Thus, responses depend only on relative changes in the input, not on its absolute magnitude. This distinction is conveniently illustrated using a sequence of step inputs that transition from a baseline value u_i to a new level u_{i+1} . We assume that successive steps are sufficiently separated in time so that the system has effectively reached steady state before each new step occurs. Under perfect adaptation, all responses eventually settle to the same steady value, but the transient dynamics may vary with input magnitude. Under FCD, by contrast, the transient responses are identical up to a time shift, reflecting invariance under input scaling.

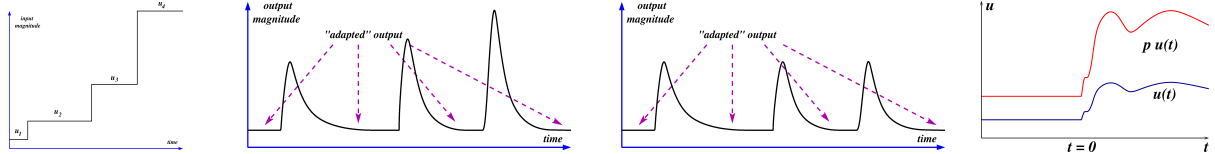


Figure 32: left to Right: Step-wise input with equal fold-changes $\frac{u_{i+1}}{u_i}$. Perfect adaptation requires that the response (eventually) returns to pre-stimulus value, but the transient response amplitude and timing generally depends on input magnitudes (for example, it is proportional to magnitude, for any linear system). Scale-invariance means that the response is exactly the same in amplitude and timing. In other words, at best only fold-change can be detected. More generally, we study responses to non-step functions: response should be the same for u and pu .

We now formalize this notion of scale invariance. The main references for this material are [109] and [108]. More generally, the framework concerns invariance under the action of a group of symmetries acting on inputs; FCD corresponds to the special case in which the symmetry group is the multiplicative group of positive real numbers.

We consider systems of the form

$$\dot{x} = f(x, u), \quad y = h(x, u),$$

where $x \in \mathbb{X} \subset \mathbb{R}^n$, $u \in \mathbb{U}$, and $y \in \mathbb{Y}$. We assume that for each constant input $u(t) \equiv \bar{u}$, there exists a unique steady state $\bar{x} = \sigma(\bar{u})$ satisfying

$$f(\bar{x}, \bar{u}) = 0.$$

In many contexts one further assumes that this equilibrium is globally asymptotically stable (GAS) for the system with constant input \bar{u} , so that

$$\lim_{t \rightarrow \infty} \varphi(t, \xi, u) = \sigma(\bar{u}) \quad \text{for all initial conditions } \xi \in \mathbb{X}.$$

Although this assumption is often natural in applications, it is not required for the results presented here.

If \mathbb{X} is an open subset of \mathbb{R}^n (or the closure of such a set), we say that the system is *analytic* if the functions f and h are real-analytic in x . The system is said to be *irreducible* if it is both accessible and observable. Accessibility means that the accessibility rank condition holds,

$$\mathcal{LA}_{\mathcal{F}}(x) = \mathbb{R}^n \quad \text{for all } x \in \mathbb{X},$$

so that no conservation laws restrict the dynamics to lower-dimensional invariant manifolds. For analytic systems, this is equivalent to the property that the set of states reachable from any given initial condition has nonempty interior; see [113] for details. Observability means that no two distinct states produce identical outputs for all possible inputs, that is,

$$\psi(t, x, u) = \psi(t, \tilde{x}, u) \quad \forall t, u \quad \Rightarrow \quad x = \tilde{x}.$$

For analytic input-affine systems, observability is equivalent to separability of distinct states by the observation space; see [113]. In biomolecular applications, analyticity and irreducibility are typically mild technical assumptions and are often satisfied.

We say that a system *perfectly adapts to constant inputs* if the steady-state output

$$h(\sigma(\bar{u}), \bar{u})$$

is equal to a fixed value $y_0 \in \mathbb{Y}$, independent of the particular constant input value \bar{u} . Thus, perfect adaptation requires invariance of the steady-state output under constant inputs, but places no restriction on transient behavior.

To define scale invariance, let \mathcal{P} be a family of continuous, onto transformations $\pi : \mathbb{U} \rightarrow \mathbb{U}$. For any input $u(t)$ and any $\pi \in \mathcal{P}$, we write πu for the time-dependent input defined by $(\pi u)(t) = \pi(u(t))$. The continuity assumption ensures that piecewise continuous inputs remain so after transformation. Ontoness is assumed mainly to preserve irreducibility; weaker conditions are often sufficient in practice. The prototypical example is *scale invariance*, where $\mathbb{U} = \mathbb{R}_{>0}$ and

$$\mathcal{P} = \{ u \mapsto pu \mid p > 0 \}.$$

In this case, invariance under \mathcal{P} implies that responses depend only on fold changes u_{i+1}/u_i , hence the alternative name *fold-change detection*.

We say that a system is \mathcal{P} -invariant if, for all $t \geq 0$, all constant inputs \bar{u} , all admissible inputs u , and all transformations $\pi \in \mathcal{P}$,

$$\psi(t, \sigma(\bar{u}), u) = \psi(t, \sigma(\pi\bar{u}), \pi u). \quad (1)$$

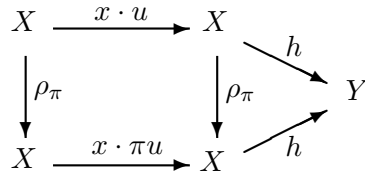
In words, starting from the appropriate steady state, the response to an input u is identical to the response to the transformed input πu .

If the action of \mathcal{P} on \mathbb{U} is transitive, meaning that any two constant inputs can be mapped to one another by some $\pi \in \mathcal{P}$, then \mathcal{P} -invariance implies perfect adaptation. Indeed, the outputs in (1) must coincide at time $t = 0$, and transitivity allows any constant input to be related to any other.

Finally, we introduce the notion of equivariance. A family of differentiable maps

$$\{\rho_\pi : \mathbb{X} \rightarrow \mathbb{X}\}_{\pi \in \mathcal{P}}$$

is called a \mathcal{P} -equivariance family if the coordinate change $x \mapsto \rho_\pi(x)$ maps solutions of the original system with input u to solutions of the transformed system with input πu , while preserving outputs:



where “ $x \cdot u$ ” means the state that results from initial state x and a finite-length input y . Equivalently, for all $x \in \mathbb{X}$, $u \in \mathbb{U}$, and $\pi \in \mathcal{P}$,

$$\begin{aligned} f(\rho_\pi(x), \pi u) &= (\rho_\pi)_*(x) f(x, u), \\ h(\rho_\pi(x), \pi u) &= h(x, u), \end{aligned}$$

where $(\rho_\pi)_*$ denotes the Jacobian of ρ_π . These relations form a system of first-order quasilinear partial differential equations that may, in principle, be solved by the method of characteristics. Importantly, verification of equivariance does not require explicit computation of system trajectories.

The main result of [108] provides a complete characterization of scale invariance, a necessary and sufficient ‘‘certificate’’ as follows.

Theorem. *An analytic and irreducible system is \mathcal{P} -invariant if and only if there exists a \mathcal{P} -equivariance family.*

Three typical adaptation motifs: two IFF’s (one SI) & a nonlinear IFB. Scale invariance provides a powerful criterion for distinguishing between network motifs that may appear equivalent at first glance. Consider the two incoherent feedforward (IFF) motifs shown in Figure 33(b,c). In both cases, the input activates the intermediate variable x and the output y , while x represses y . Despite this superficial similarity, the dynamical behaviors of the two motifs differ fundamentally. The first motif admits no nontrivial equivariance and therefore cannot exhibit scale invariance. By contrast, the second motif is scale invariant: scaling the input by a factor p results in a corresponding scaling of the intermediate variable, while leaving the output trajectory unchanged (that is, if $u(t)$ is replaced by $pu(t)$, then $(px(t), y(t))$ satisfies the same equations with input $pu(t)$). These two feedforward architectures will be revisited later in this article. A third motif that naturally arises in the context of scale invariance is the *nonlinear integral feedback* structure shown in Figure 33(d). This motif is likewise scale invariant, by an argument analogous to that used for the second IFF motif. All three motifs are analyzed in [50, 108], where proofs of global asymptotic stability for each constant input u are also provided. It is also interesting to note that linearizing IFF1 and IFF2 at equilibria corresponding for any given constant input results in feedforward linear systems in which an exact cancellation occurs, giving a washout filter (DC gain zero), no matter what are the values of the parameters $\alpha, \beta, \gamma, \delta$. In that sense, adaptation is robust.

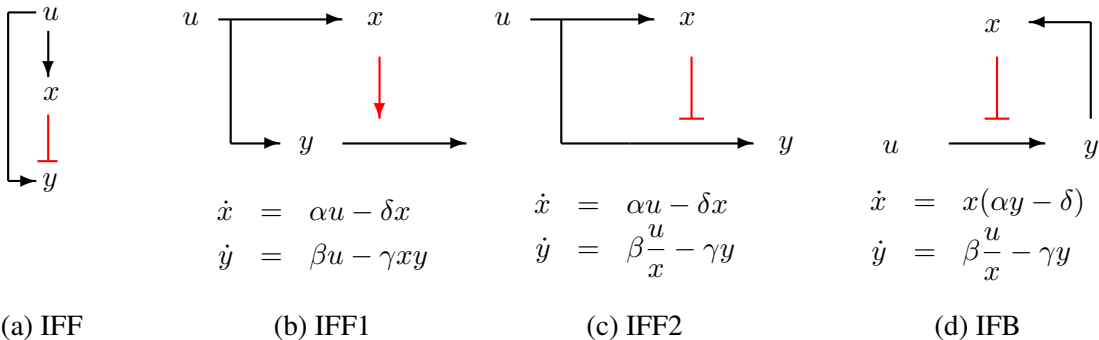


Figure 33: Two IFF and one IFB motifs (top) and respective two-dimensional models of dynamics (bottom). In every case, u is the input and y is the output. Variables are assumed positive; constants $\alpha, \beta, \gamma, \delta$ are positive. (a) An IFF conceptual motif. (b) One interpretation of x repression of y : intermediate variable x enhances degradation of y . (c) Different interpretation: intermediate variable x inhibits production of y . (d) IFB (integral feedback).

Scale-invariance and stochastic searches. SI theory has an application to stochastic spatial search. Consider a vehicle moving in space which continuously senses a space dependent input $u = u(r, t)$, where r

is the space variable. Suppose for concreteness that the input represents a diffusive chemical being emitted from a point source,

$$u(r, t) = \frac{u_s}{(4\pi Dt)^{3/2}} e^{-\frac{(r-r_0)^2}{4Dt}}$$

in three dimensions. For example, in chemotaxis, discussed below, $u(r, t)$ represents a diffusive chemoattractant field that scales with source intensity. Since the field $u(\cdot, t)$ at time t scales with the source intensity u_s , *positional information about the source is encoded in the shape of field, and not in its amplitude*. Thus SI sensing should result in statistically the “same” stochastic search (independent of strength u_s). One way to formalize this is as follows. We consider a Jump-Markov process for $c(t, s, v, x)$, the probability density at time t , location s , internal state x , and velocity v . We assume that individuals performing the search have internal dynamics $\dot{x} = f(x, u)$ and that stochastic steering depends only on a measured variable $y = h(x)$. (In the *E. coli* chemotaxis application to be discussed below, x is a vector of concentrations of proteins in several modified methylated/phosphorylated forms, and y picks the phosphorylated form of a protein called CheY.) Reorientations (jumps in velocities) are guided by a Poisson process with intensity $\lambda(y)$, according to the kernel

$$T_y(v, v') = \text{Prob}\{v' \rightsquigarrow v \mid \text{input is } y\}.$$

The density c satisfies the transport (Fokker-Planck, forward Kolmogorov, Smoluchowski) equation

$$\frac{\partial c}{\partial t} + \nabla_s \cdot cv + \nabla_x \cdot cf = -\lambda(y)c + \int_V \lambda(y)T_y(v, v')c(t, s, v', x)dv'$$

The input at location s and time t is $U(t, s)$, and it appears in these equations through the vector field f . The SI property implies the invariance of marginal distributions for time and position, defined as:

$$n(t, s) = \int_{\mathbb{X}} \int_V c(t, s, v, x) d\mu_{\mathbb{X}}(x) d\mu_V(v).$$

This is proved in [118], using an equivariance provided by the necessary part of the theorem, and showing that then the density with respect to the transformed field πU is

$$\tilde{c}(t, s, v, x) = c(t, s, v, \rho^{-1}(x)) \det [\rho_*^{-1}(z)].$$

Scale invariance in chemotaxis. Chemotaxis refers to the directed movement of organisms in response to chemical cues. Chemical stimuli, or chemoeffectors, may function as attractants or repellents, giving rise to chemoattraction or chemorepulsion, respectively. These cues can be environmental nutrients or toxins, or they may be signaling molecules secreted by organisms to coordinate long-range interactions within a population.

Chemotaxis plays a role in behavior across many biological scales, from bacteria and single cells in multi-cellular organisms to amoebae and social insects [15]. It underlies a wide range of biological phenomena, including nutrient foraging by *E. coli*, aggregation in slime molds, morphogenesis and tissue organization during embryonic development, tumor angiogenesis, wound healing, and numerous human diseases. The mathematical study of chemotaxis has therefore been an active and expansive area of research; see, for example, [130] for a survey of bacterial chemotaxis models, or [38] for an application to Alzheimer’s disease based on chemotactic mechanisms. Although our focus here is on single-cell movement, it is worth noting that a complementary and equally important branch of chemotaxis research concerns pattern formation in spatially distributed systems, such as the emergence of fruiting bodies or animal coat patterns. This line of work was initiated in large part by the seminal Keller–Segel model [65].

Among known signal transduction pathways, the chemotaxis network of *E. coli* is arguably the most thoroughly studied. This system enables bacteria to navigate gradients of chemical attractants or repellents by sensing *temporal* changes in chemoeffector concentrations rather than spatial differences. Motile chemotactic bacteria alternate between relatively straight swimming episodes (*runs*) and brief reorientation events (*tumbles*). These behaviors correspond to counterclockwise (CCW) and clockwise (CW) rotation of the flagellar motors, respectively. While tumbles lead to random reorientation, motion in favorable directions suppresses tumbling and results in extended runs, thereby biasing the random walk toward regions of higher attractant concentration [17]. See Figure 34.

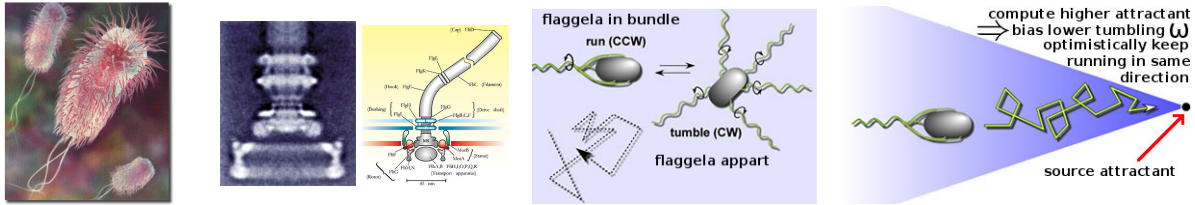


Figure 34: *Escherichia coli* is a single-celled bacterium with a typical length of approximately $2\ \mu\text{m}$. (Photo in Public Domain from [134].) It swims using several helical flagella driven by a proton-powered rotary motor, illustrated here by a micrograph and a schematic. (Photo and diagram from [18].) Chemotaxis in *E. coli* implements a biased stochastic search in a nutrient concentration field. When the flagellar motors rotate clockwise, the flagella disrupt their bundle and the cell undergoes a reorientation (*tumble*); when the motors rotate counterclockwise, the flagella form a coherent bundle and the cell moves approximately straight (*run*). If the bacterium senses an increase in attractant concentration along its trajectory, the tumbling rate is reduced, prolonging runs in favorable directions; otherwise, tumbling resumes, allowing the cell to reorient and sample new directions. (Diagrams from [135].)

E. coli can detect a wide range of chemical cues, including amino acids, sugars, and dipeptides, as well as physical stimuli such as pH, temperature, and redox state. The most abundant chemoreceptors, present in thousands of copies per cell, are Tar and Tsr, which primarily sense aspartate and serine, respectively. Additional lower-abundance receptors detect dipeptides (Tap) and sugars such as ribose and galactose (Trg) [122]. The chemotaxis system exhibits remarkably high sensitivity, responding over several orders of magnitude in ambient concentration to small relative changes in attractant or repellent levels [23].

A major advantage of the *E. coli* chemotaxis pathway as a model signal-transduction system is its relative insulation from other cellular processes, such as metabolism, allowing it to be treated as a largely autonomous functional module [69]. Most biochemical rate constants and average protein concentrations in this pathway have been measured experimentally [77]. The core signaling network is well characterized: chemoreceptors assemble with the adaptor protein CheW and the histidine kinase CheA into large clusters at the cell poles. Attractant binding inhibits CheA autophosphorylation, whereas repellent binding enhances it. Activated CheA transfers phosphoryl groups to the diffusible response regulator CheY, which in turn biases flagellar motor rotation toward clockwise (CW) rotation and tumbling. CheY is rapidly dephosphorylated by the phosphatase CheZ, enabling fast responses to changes in input signals.

The dynamics of the chemotaxis network have been characterized using two main experimental approaches. Phenotypic assays measure the fraction of time tethered cells spend in CW versus counterclockwise (CCW) rotation in response to step changes in chemoeffector concentration [72]. Complementary biochemical assays employ fluorescence resonance energy transfer (FRET) to monitor CheY phosphorylation levels *in vivo* [123]. In particular, FRET between CheY–YFP and CheZ–CFP provides a quantitative readout of CheA kinase activity, since the FRET signal is proportional to the concentration of the CheY-P–CheZ complex and thus reflects the steady-state balance between CheY phosphorylation and dephosphorylation [107].

Figure 35 schematically summarizes the principal components of the *E. coli* chemotaxis signaling network.

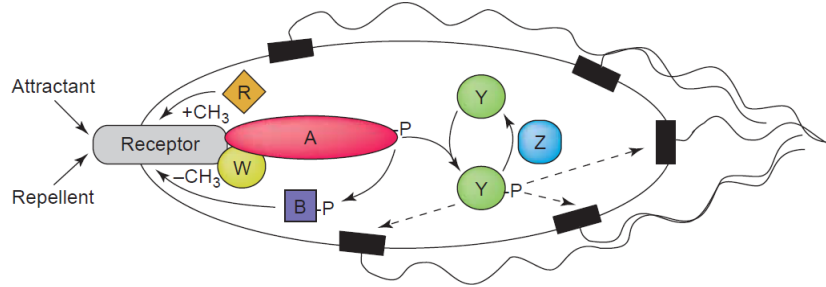


Figure 35: Schematic of *E. coli* chemotaxis biochemistry, from [122]

A defining feature of the chemotaxis network is *adaptation*: following a sustained change in chemoeffector concentration, tumbling activity returns to its pre-stimulus level. Adaptation is mediated by receptor methylation and demethylation, catalyzed by the enzymes CheR and CheB, respectively, at multiple modification sites on each receptor. This methylation system provides a molecular memory that effectively compares past and present inputs. Integral feedback arises through the phosphorylation of CheB by CheA, which couples pathway output to the adaptation machinery [6, 139]. Mathematically, the intracellular biochemistry of the chemotaxis signaling network is well described by a systems of ordinary differential equations which capture the temporal evolution of the relevant protein concentrations and modification states. A representative reduced model is

$$\begin{aligned}\dot{m} &= V_R r \frac{1-a}{1-a+K_R} - V_B b_p \frac{a}{a+K_B} \\ \dot{b} &= k_4 a (B-b) - k_5 b \\ \dot{y} &= k_1 a (Y-y) - k_2 y z - k_3 y,\end{aligned}$$

where:

- m is the receptor methylation level,
- b is the concentration of phosphorylated CheB (CheB-P),
- y is the concentration of phosphorylated CheY (CheY-P), which serves as the pathway output,
- B and Y are the total concentrations of CheB and CheY,
- r and z denote the concentrations (or effective activities) of CheR (methyltransferase) and CheZ (phosphatase), respectively.

The kinase activity a is given by the Monod–Wyman–Changeux model of allosteric regulation

$$a(m, u) = \left(1 + c e^{-\gamma N m} \left(\frac{1+u/K_I}{1+u/K_A} \right)^N \right)^{-1},$$

where u is the external ligand concentration, N is the number of receptor homodimers in a functional signaling complex, and $V_R, V_B, K_R, K_B, k_i, c, \gamma, K_I, K_A$ are positive constants. The parameter values are typically chosen to represent the Tar receptor responding to α -methyl-DL-aspartate (MeAsp).

The resulting cell motion can be modeled separately as a stochastic process: tumbles occur at random times according to a Poisson process whose instantaneous rate depends on the concentration of phosphorylated CheY (CheY-P). In this way, the deterministic signaling dynamics modulate the statistics of the run-and-tumble motion. Figure 36 shows the wiring diagram of this system.

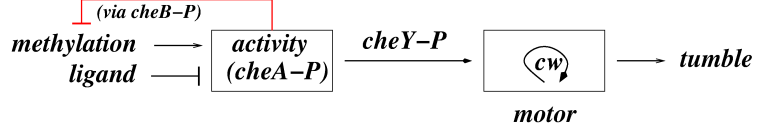


Figure 36: Phenomenology of *E. coli* adaptation circuit

The paper [109] carried out this analysis, and pointed out that for inputs u (ligand level) in the experimental range $18\mu M \approx 0.006K_A \approx K_I \ll u \ll K_A$, one has the simplified form

$$a(m, u) \approx F(ue^{-\gamma m})$$

for some function F . Then equivariance given by

$$u \mapsto pu, \quad y \mapsto y, \quad b \mapsto b, \quad m \mapsto m + \frac{1}{\gamma} \ln p$$

establishes that *E. coli* chemotaxis should have scale-invariant behavior. Thus, recalling the discussion about scale-invariant searches, the stochastic search algorithm as performed by bacteria should result in equivalent stochastic search processes, independently of the strength u_s of a diffusive field. The paper [109] predicted this spatial behavior as well.

Experimental verification of scale-invariance for *E. coli* chemotaxis. To test the scale-invariance predictions from [109], the authors of [73] carried out fluorescence resonance energy transfer (FRET) experiments on tethered cells and microfluidic experiments on freely swimming cells. In the FRET experiments, the bacteria were adapted to a given concentration of MeAsp, u_0 , and then exposed to a smoothly varying temporal waveform of stimulus, $u(t)$. The FRET response, $\Delta FRET(t)$, was recorded continuously throughout many such experiments in which u_0 was varied over a broad range, while keeping constant the ratio $u(t)/u_0$. Comparisons of the temporal response profiles over a > 10 fold range of u_0 (Fig. 37) show that both the amplitude and waveform of response are invariant. The concentration range over which this invariance is observed is consistent with expectations from the FCD analysis in [109], i.e. between the two dissociation constants, K_I and K_A , of the Tu-Shimizu-Berg model. The waveform of MeAsp concentration in the FRET experiments was $u(t) = u_0 \exp(Ae^{-\beta^2(t-t_c)^2} \sin 2\pi\nu t)$, a function whose logarithm is a baseline $\ln(u_0)$ plus a sinusoidal waveform.

Experimental verification of scale-invariant spatial search for *E. coli* chemotaxis. An experimental confirmation of invariance of search statistics was also provided in [73]. If the chemotaxis signaling pathway exhibits invariance under simultaneous rescaling of temporal stimulus gradients and background ligand levels, then an individual swimming *E. coli* cell should be equally effective at ascending spatial gradients that differ only by an overall multiplicative factor. Although tracking the trajectory of a single bacterium over long time intervals is experimentally challenging, the collective behavior of a large population can be monitored reliably over extended periods. One thinks of each bacterium's motion as an independent realizations of the same stochastic process. If fold-change detection persists at the behavioral level, one

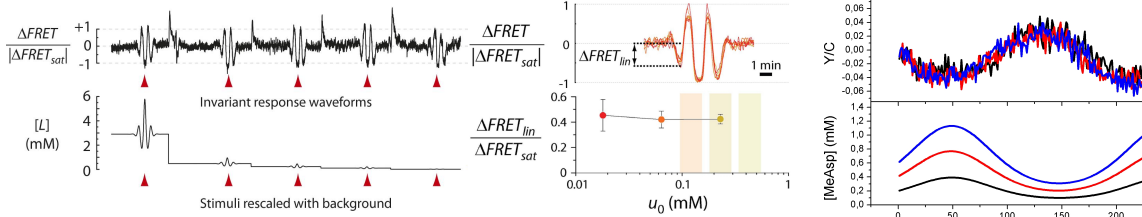


Figure 37: Demonstration of FCD in *E. coli*'s chemotaxis network [73], shown by invariance of FRET response waveforms and amplitudes upon rescaling of background concentration, using tethered cells. Left: responses to time-varying ligand with means in range 0.018-2.9 mM. Center: Overlapped time series of FRET responses to the stimulus waveform. Each curve shows the deviation, $\Delta FRET$, from the adapted state FRET signal, normalized by the deviation upon a saturating stimulus, $|\Delta FRET_{sat}|$; lower panel shows FRET response amplitudes $|\Delta FRET_{lin}|$ of the waveforms shown in the upper panel, computed from the small-amplitude peak within the linear regime of the response. Right: Another experiment, overlapped FRET traces with different signal (personal communication from T. Shimizu). The label Y/C represents the change in the ratio CheY-P to total CheY, and is roughly proportional to $\Delta FRET(t)/|\Delta FRET_{sat}|$ (see [73]).

expects that the spatial evolution of bacterial populations will be indistinguishable across appropriately rescaled chemoeffector gradients, provided that the cells are initially adapted to background concentrations scaled in the same proportion as the gradient magnitude. This hypothesis was tested experimentally in [73], which examined population-level migration in controlled spatial gradients of the attractant MeAsp using a microfluidic setup.

In these experiments, a linear concentration gradient was generated by flowing buffer solutions with different MeAsp concentrations through two parallel side channels, referred to as the source and sink channels, with higher and lower concentrations, respectively (see Figure 38). Diffusive exchange across a thin agarose layer established a corresponding gradient within the central observation channel on a rapid time scale. The motion of bacterial populations within this channel was recorded using video microscopy. Initially, cells were distributed approximately uniformly, but over time they preferentially accumulated toward the side adjacent to the source channel. Quantitative analysis of the recorded image sequences yielded the spatial cell density profile $B(x)$ along the gradient direction. The concentration profile $B(x)$ of bacteria along the linear gradient shown in Figure 38 shows a clear chemotactic response, evident as an accumulation towards higher concentrations (i.e. $x = 0$). The nearly identical response despite the large variation in input stimuli supports FCD.

An application to model invalidation. The paper [124] examined adaptive signaling in a eukaryotic chemotaxis pathway by exposing *Dictyostelium discoideum* cells to controlled temporal profiles of the chemoattractant cyclic adenosine monophosphate (cAMP) using a microfluidic device. Pathway activity was monitored via activated Ras (Ras-GTP), reported by RBD-GFP, a fluorescent probe based on the Ras-binding domain of human Raf1. The experiments revealed near-perfect adaptation of Ras activity over a broad range of cAMP concentrations, from 10^{-2} nM to 1 μ M. To account for these observations, the authors compared several mechanistic models and identified an incoherent feedforward architecture as providing the best fit. The resulting model consists of six coupled ordinary differential equations describing receptor activation, Ras regulation through RasGEF and RasGAP, and reporter dynamics. Two receptor populations with distinct affinities for cAMP contribute additively to a pooled upstream signal, which drives both Ras activation and inactivation.

In [110], we revisited this model from the perspective of fold-change detection, in a regime where the

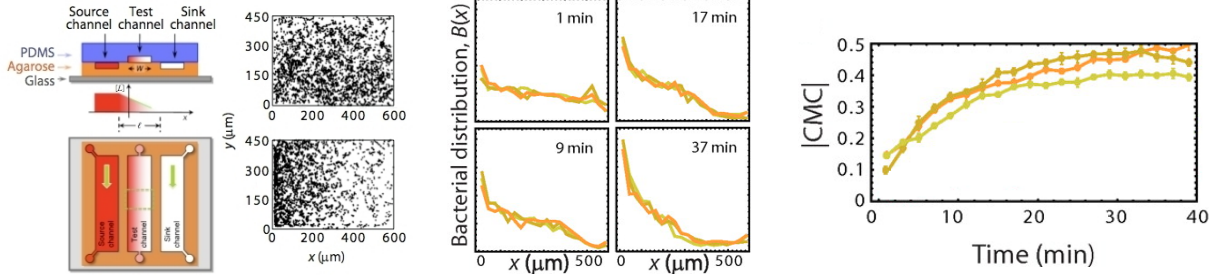


Figure 38: Free-swimming cells in a linear microfluidic gradient, supporting scale search invariance. Left: Microfluidics setup and representative microscopy images, showing spatial distribution of cells at the start of an experiment (upper) and 19 min after establishment of a 0.15 mM/mm gradient along the space dimension (lower), demonstrating chemotaxis. Center: Three superimposed histograms with $(\nabla u)/(u)$ fixed at $2/3 \text{ mm}^{-1}$ and midchannel concentrations: $0.018/0.064/0.23 \text{ mM}$. Right: chemotactic migration coefficient (CMC) measuring the mean displacement of the population from the center of the channel, showing scale invariance.

levels of constitutive activation of the two types of receptors are much lower than the cAMP input level. In this regime, the receptor dynamics reduce to approximately linear filters, so that the pooled signal $u(t)$ is proportional to the external cAMP concentration. The downstream subsystem governing RasGEF, RasGAP, and Ras–GTP is therefore effectively driven by an input $u(t)$ (see [110] for details). The fitted parameters exhibit a clear separation of time scales, with Ras activation and deactivation occurring much faster than the dynamics of RasGEF and RasGAP. Exploiting this separation yields a reduced system in which the slow variables satisfy linear dynamics driven by $u(t)$, and the Ras–GTP level is given by a rational function of these slow variables:

$$\begin{aligned}\dot{x}_1 &= -a_1 x_1 + b_1 u, \\ \dot{x}_2 &= -a_2 x_2 + b_2 u, \\ y &= \frac{K b_3 x_1}{a_3 x_2 + b_3 x_1},\end{aligned}$$

where $x_1 = \text{GEF}$, $x_2 = \text{GAP}$, and y represents the quasi-steady-state level of Ras–GTP. The constants a_i , b_i , and K are determined by the original kinetic parameters. This reduced system is equivariant under the scaling transformation $x_i \mapsto p x_i$, implying scale invariance and hence fold-change detection. Simulations of the full six-dimensional model confirm this prediction: responses to cAMP step inputs differing by a constant factor (for example, $1 \rightarrow 2 \text{ nM}$ versus $2 \rightarrow 4 \text{ nM}$) collapse onto essentially identical trajectories, see Fig. 39. However, this behavior appears to be inconsistent with experimental observations. According to a personal communication from the authors of [124], experimentally doubling the cAMP input in the relevant ranges produced responses that were not fold-invariant.

This discrepancy is instructive. It suggests that the published model, or at least the fitted parameter regime, does not fully capture the input-scaling properties of the biological system. More broadly, it illustrates how fold-change detection can serve as a stringent *dynamic phenotype*: a simple test comparing responses to inputs related by a constant factor can strongly constrain admissible network structures and parameter values, without requiring direct access to internal molecular states.

5 Another transient phenotype: cumulative dose responses

In many areas of pharmacology and biomedical research, outcomes depend not only on instantaneous concentrations but on the *time-integrated exposure* to a substance. A standard way to quantify such exposure

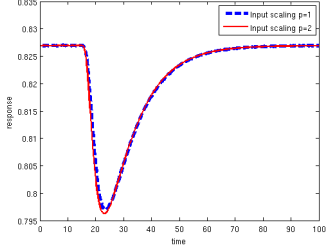


Figure 39: Scale-invariance for model from [124]: responses to steps 1→2 and 2→4 coincide. Figure reproduced from [110].

is through the area under the concentration–time curve (AUC), which captures the cumulative abundance of a molecule over a specified interval. In [50] we introduced the term *cumulative dose response* (cDR) to emphasize this perspective in a dynamical-systems context. Measurements of this type arise naturally across a wide range of experimental and clinical settings, illustrating the broad relevance of cDR-based analysis.

One prominent class of examples is provided by *cytokine release assays*, which quantify the total amount of cytokines secreted by immune cells in response to drugs, pathogens, or other stimuli. Cytokines are key regulators of immune and inflammatory processes, as well as cell growth, differentiation, and tissue repair. Commonly measured species include pro-inflammatory cytokines such as IL-6, IL-1 β , TNF- α , and IFN- γ ; anti-inflammatory cytokines such as IL-10 and IL-4; and growth factors including GM-CSF and VEGF. Experimental techniques such as ELISA and multiplex immunoassays (for example, Luminex[®]) are routinely used to quantify cumulative cytokine secretion. As an illustration, [42] describes an *in vivo* immunosensing approach in which an antibody-coated optical fiber is implanted in the rodent brain to capture cytokines released over time within a localized region; the accumulated cytokine load is then quantified by ELISA. In a clinical context, cumulative cytokine measurements are also central to the assessment of cytokine release syndrome (CRS), a potentially severe adverse effect of T-cell bispecific antibody therapies. The study [74], for instance, employed Luminex[®]-based assays and AUC analyses of cytokine profiles to compare strategies aimed at mitigating CRS.

A second major application of cumulative measurements arises in the study of *drug metabolism and clearance*. Following administration of a drug or prodrug, plasma concentrations are typically sampled over time, and the resulting concentration–time curve is integrated to obtain the AUC [27]. This quantity provides a compact summary of systemic drug exposure and plays a central role in pharmacokinetic modeling, dose selection, and safety assessment, including the evaluation of hepatic and renal clearance. A comprehensive discussion of cumulative drug excretion measures and their clinical relevance is given in [76], which highlights the use of AUC-based metrics in dosing and toxicity studies.

Finally, a familiar example from routine clinical practice is the *HbA1c (A1c) blood test*, widely used in the diagnosis and management of diabetes. The A1c value reflects the average blood glucose level over the preceding two to three months and can be interpreted as being proportional to the time integral of glucose concentration over that interval. This effective integration arises from the relatively long lifespan of red blood cells and the irreversible binding of glucose to hemoglobin, which smooths short-term fluctuations and yields a cumulative measure of glycemic exposure.

5.1 Dose response and cumulative dose response

Throughout this section we restrict attention to constant inputs $u(t) \equiv u$, and we write $y_u(t)$ to emphasize the dependence of the output on both the input value and time. Typical temporal responses to several input

levels are illustrated in the left panel of Figure 40, where, for simplicity, the notation $y_i(t)$ is used in place of $y_{u_i}(t)$. Dependence on initial conditions will not be made explicit; unless otherwise stated, all responses are assumed to start from a fixed reference state.

A system is said to exhibit *perfect adaptation* to constant inputs if the long-time output converges to a common value, independent of the particular input level. That is, there exists a constant \hat{y} such that

$$\lim_{t \rightarrow \infty} y_u(t) = \hat{y} \quad \text{for all } u.$$

This asymptotic value represents a habituated or baseline state, as in sensory systems that adapt to constant background stimuli such as steady illumination or noise. From an engineering viewpoint, such systems behave as high-pass filters, responding primarily to changes in the input rather than to its sustained level. By its very nature, adaptation is an asymptotic notion and does not constrain the behavior of the system at finite times.

In many applications, however, the transient response is of primary interest. For a fixed observation time T , one may ask how the output $y_u(T)$ varies with the input level u . Examples include the drug concentration in a tumor microenvironment at a prescribed time after administration, tumor size at a given stage of therapy, or the number of infected individuals at a specified time during an epidemic. We refer to the mapping

$$u \mapsto y_u(T)$$

as the *dose response* of the system at time T , and denote it by $\text{DR}(u, T)$. Experimentally, this curve is obtained by applying different constant input levels and recording the corresponding output at the chosen time point. The center panel of Figure 40 illustrates dose-response curves derived from the time courses shown on the left.

On the other hand, *transient* behaviors, particularly how $y_u(T)$ varies with u at a fixed time T , are often of interest. (What is the concentration of a drug in a tumor microenvironment, after 1hr, as a function of the drug dose? What is the size of a tumor after 60 days of the start of therapy, as function of the drug dose? How many infected individuals are there two months after the start of an epidemic, as a function of transmission parameters?)

In many biological and pharmacological settings, the output variable turns over slowly or accumulates in a compartment such as tissue or bloodstream. In such cases, the experimentally accessible quantity, and often the relevant phenotypic response, depends not on the instantaneous output but on its time integral. This motivates the definition of the *cumulative dose response*

$$\text{cDR}(u, T) := \int_0^T y_u(t) dt,$$

that is, the area under the output curve up to time T . The right panel of Figure 40 shows cumulative dose-response curves corresponding to the same set of temporal responses. Unlike perfect adaptation, which constrains only steady-state behavior, dose response and cumulative dose response capture distinct aspects of finite-time dynamics that are often central to experimental observation and interpretation.

Motivation: T cell recognition. As discussed earlier, cumulative dose responses (cDRs) arise naturally in many biological contexts. The specific motivation for the study in [50], however, originated in experimental work on T cell signaling, particularly the measurements reported in [132]. We briefly summarize that biological setting and its implications here.

Adaptation is a fundamental requirement of the immune system. T cells must mount strong responses to pathogens and malignant cells while at the same time maintaining tolerance to self-antigens in order

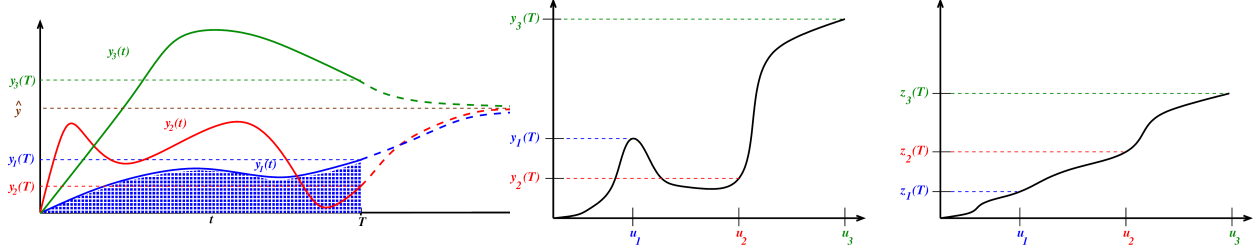


Figure 40: **Left:** Time courses of the system output $y(t)$. Three representative responses $y_1(t)$, $y_2(t)$, and $y_3(t)$ are shown, corresponding to constant input levels u_1 , u_2 , and u_3 , respectively. The values of the responses at a prescribed observation time T define their dose–response (DR) values, indicated on the vertical axis. In an adaptive system, all responses converge to the same steady-state value \hat{y} as $t \rightarrow \infty$, independently of the input magnitude. Solid curves depict the responses up to time T , while dashed curves indicate their continuation to steady state. The shaded region illustrates the integral $z_1(T) = \int_0^T y_1(t) dt$, which underlies the definition of the cumulative dose response (cDR). **Center:** Dose response (DR) at time T , obtained from the temporal responses shown in the left panel. The vertical axis represents the output evaluated at $t = T$, now plotted as a function of the input level u . In this example, the DR is nonmonotonic; for instance, $u_1 < u_2$ while $y_1(T) > y_2(T)$. **Right:** Cumulative dose response (cDR) at time T . The vertical axis now shows the integrated output $z(T) = \int_0^T y(t) dt$, plotted against the input u . The value $z_1(T)$ corresponds to the shaded area in the left panel. In this example, the cDR is monotonic: although $y_2(T) < y_1(T)$, the area under $y_2(t)$ exceeds that under $y_1(t)$, leading to $z_1(T) < z_2(T) < z_3(T)$ for $u_1 < u_2 < u_3$.

to avoid autoimmunity. T cell activation is initiated when T cell receptors (TCRs) bind to peptide major histocompatibility complex (pMHC) molecules displayed on antigen-presenting cells (see Figure 41). This recognition event triggers intracellular signaling cascades that ultimately lead to the secretion of cytokines, which coordinate downstream immune responses by recruiting and activating additional immune cells.

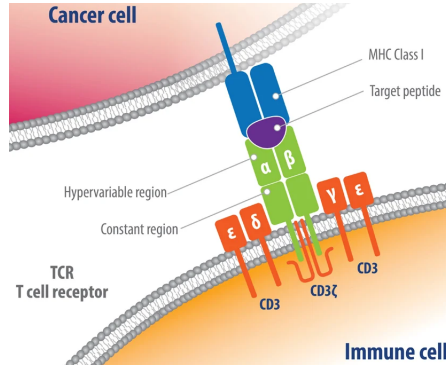


Figure 41: Cancer cell interacting with a T cell. T cell activation is triggered by the binding of T cell receptors (TCRs) to peptide major-histocompatibility complex (pMHC) antigens. Figure reproduced from [78].

The experiments reported in [132] investigated how primary human CD8⁺ T cells respond to sustained antigen stimulation. Specifically, CD8⁺ T cells expressing the c58c61 TCR were stimulated with recombinant pMHC ligand (the cancer-associated peptide 9V) immobilized on plates, providing a controlled and constant antigen input u over a wide range of concentrations. This antigen is commonly used in studies of T cell binding and antigen discrimination. The measured output was the cumulative amount of secreted

TNF- α , denoted by

$$z(t) = \int_0^t y(s) ds,$$

where $y(t)$ represents the instantaneous cytokine secretion rate. Figure 42 displays the experimentally measured cumulative TNF- α levels as functions of antigen concentration, evaluated at multiple time points ranging from one to eight hours. These cumulative dose responses exhibit strikingly non-monotonic and, in some cases, oscillatory behavior.

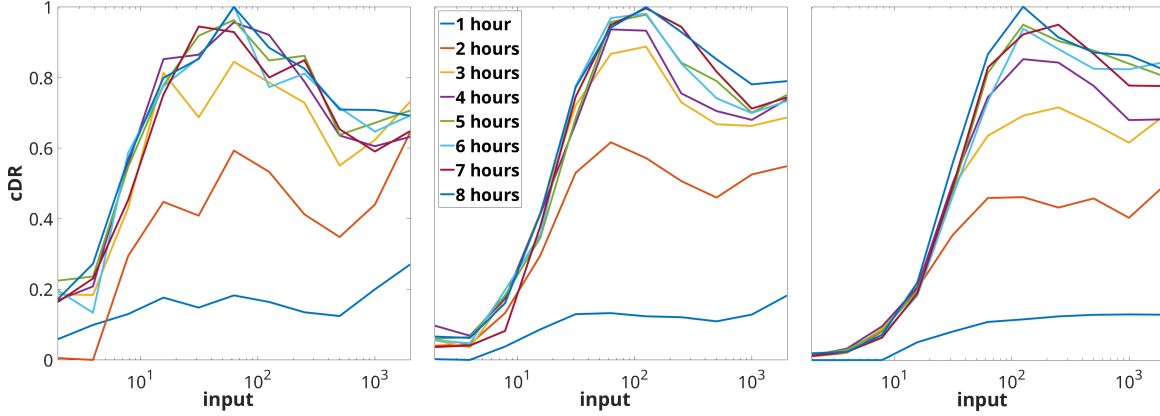


Figure 42: Experimental cumulative dose responses in T cell activation, plotted for various times ($t = 1$ to 8 hours), with separate plots from each experiment. Plots done from data used to generate Figure 1 in the SI of [132]. Horizontal axis denotes concentrations of the input (in units of ligand in ng/well).

Despite the fact that only the integrated output $z(t)$ was directly measured, the data also provide strong evidence for adaptation. In particular, for sufficiently large times, the secretion rate $y_u(t)$ appears to become independent of the antigen concentration u . To make this point more explicit, one may form rough estimates of $y(t)$ by numerically differentiating the measured $z(t)$ data using finite differences and imposing the initial condition $y(0) = 0$. Applying this procedure to the experimental replicates shown in Figure 42 yields the approximate time courses displayed in Figure 23. While these estimates are necessarily coarse, due to the one-hour sampling interval and experimental noise, they are consistent with the conclusion that the system adapts in the sense that $y_u(t)$ approaches a common value (here effectively zero) at long times, regardless of the antigen dose. Apparent negative values of $y(t)$ at isolated time points are likely artifacts of numerical differentiation or reflect baseline cytokine levels unrelated to antigen stimulation.

Beyond adaptation, the experimental data suggest an additional and stronger property. Over a substantial range of antigen concentrations (pMHC ligand levels from approximately 1.95 to 2000 ng/well; see Figure 2 of [132]), the cumulative responses exhibit a form of scale invariance: for sufficiently large inputs, the transient responses collapse onto similar trajectories. This behavior is consistent with fold-change detection (FCD) at the level of the output and resembles the dynamics produced by certain incoherent feedforward architectures (specifically IFF2) or nonlinear integral feedback mechanisms discussed earlier.

These observations motivate a natural theoretical question: which network motifs are capable, for appropriate parameter regimes, of simultaneously exhibiting perfect adaptation and producing the non-monotonic cumulative dose responses observed in T cell activation? A non-monotonic cDR immediately rules out linear systems, which necessarily yield linear and hence monotonic dose responses, as well as monotone nonlinear systems, whose dose responses are likewise monotonic. Based on numerical explorations, it was suggested in [132] that incoherent feedforward loops alone are insufficient to generate non-monotonic cDR

behavior without the addition of explicit thresholding mechanisms, leaving open the search for alternative or augmented network architectures capable of explaining these experimental findings. The work [50] set out to investigate this question for the three prototypical motifs used in adaptation and FCD theory, and established the following result:

Theorem. *IFF1 and IFF2 motifs in Figure 33 always have (for all parameters and all times) a monotonic cDR. On the other hand, the IFB motif in Figure 33 may have a non-monotonic cDR.*

Thus, the two common types feedforward motifs can never exhibit such behaviors, because their cDR's are always monotonic. This is especially surprising for one of them (IFF1) because for such systems the DR itself can be non-monotonic, yet the cDR is monotonic, in behavior reminiscent of the cartoon illustrations in Figure 40. This result was complemented by the new finding that, on the other hand, the standard nonlinear integral feedback for adaptation is indeed capable of showing non-monotonic cDR, and thus is potentially a mechanism that is consistent with the experimentally observed non-monotonic cDR. In summary:

As an example, consider the following system of two differential equations, which is a particular example of the IFF1 model.

$$\begin{aligned}\dot{x} &= -x + u \\ \dot{y} &= -10xy + u.\end{aligned}$$

This is an adapting system: for any given constant input $u > 0$, the steady states are $\bar{x} = u$ and $\bar{y} = 1/10$, which is independent of u , so that the steady state output $\hat{y} = 1/10$ is independent of u . Figure 43 shows plots of the DR (non-monotonic) and the cDR (monotonic). For an example of IFB, consider the following system of two differential equations:

$$\begin{aligned}\dot{x} &= x(y - 6) \\ \dot{y} &= \frac{u}{x} - y.\end{aligned}$$

This is also an adapting system: for any given constant input $u > 0$, the steady states are $\bar{x} = u/6$ and $\bar{y} = 6$, so that the steady state output $\hat{y} = 6$ is independent of u . The right panel of Figure 43 shows plots of the (non-monotonic) cDR.

To show the IFF1 statement in the theorem, one must show that the map

$$u \mapsto \int_0^T y_u(t) dt$$

is nondecreasing (for any fixed $T > 0$), and in turn, analyzing the variational system along any given trajectory, one must show that

$$\int_0^T \partial_u y_u(t) dt \geq 0$$

for all T, u , which is done by a careful balancing of $+/ -$ contributions to the integral.

The proof for IFF2, on the other hand, can be understood conceptually as follows. Let us consider a larger class of systems:

$$\begin{aligned}\dot{x} &= \alpha u - \delta x \\ \dot{y} &= \beta \frac{u}{K + x} - \gamma y\end{aligned}$$

(so that IFF2 is the special case $K = 0$).

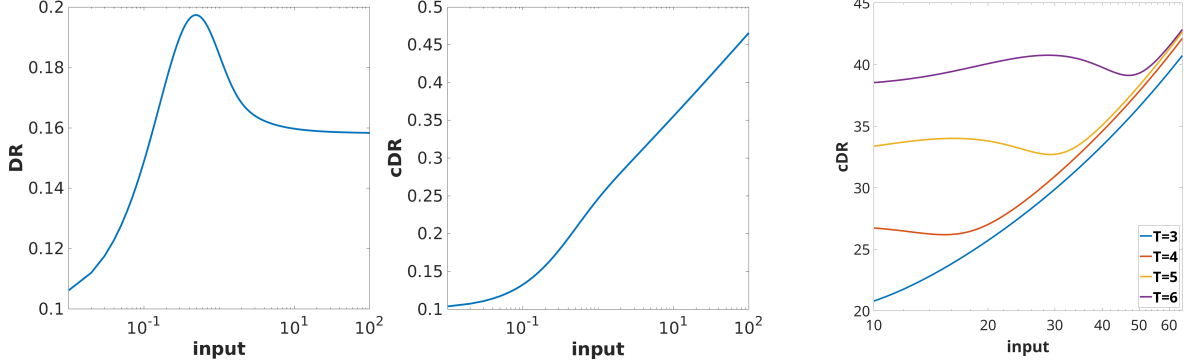


Figure 43: Left and center: Plots of DR ($y(t)$) and cDR ($\int_0^T y(t)dt$) for the example $\dot{x} = -x + u$, $\dot{y} = -10xy + u$. The initial conditions are $x(0) = 0$, $y(0) = 1/10$, and the time horizon is $T = 1.5$. Using logarithmic scale on inputs, for comparison with experimental plots. Observe that the DR is non-monotonic, yet, surprisingly, the cDR is monotonic. Right: Plot of cDR ($\int_0^T y(t)dt$) for the integral feedback example $\dot{x} = x(y - 6)$, $\dot{y} = \frac{u}{x} - y$. The initial conditions are $x(0) = 0.1$, $y(0) = 6$, and time horizons shown are $T = 3, 4, 5, 6$. Observe that, just as with the experimental data plotted in Figure 42, the cDR is more monotonic (on the shown ranges, at least) for smaller time horizons T . Using logarithmic scale on inputs, for comparison with experimental plots.

Now, when $K = 0$, one has the equivariance (one-parameter Lie group of symmetries) $(u, x, y) \mapsto (pu, px, y)$ and this suggests using a new variable $p := u/(K + x)$ to map to what turns out to be a monotone system:

$$\begin{aligned}\dot{x} &= \alpha u - \delta x \\ \dot{p} &= p \left(\frac{\delta x}{K + x} - \alpha p \right) \\ \dot{y} &= \beta p - \gamma y.\end{aligned}$$

In this system, solutions depend monotonically on initial states, and in particular on $p(0)$, and thus also (for a fixed initial state $x(0)$) monotonically on the (constant) input u . Note that the original system is not monotone, but the transformed system is.

6 Concluding remarks and outlook

This article has argued that many biologically relevant questions about network function are answered not by steady states alone, but by the qualitative structure of *transient* and *input-driven* behaviors. We used the term *dynamic phenotypes* to emphasize experimentally accessible response features, such as overshoots, biphasic transients, pulse trains, subharmonics, fold-change invariance, and cumulative-exposure effects, that emerge under rich classes of probing inputs beyond step stimuli. In this perspective, dynamic responses become a source of *structural information*: by observing which qualitative phenotypes are possible (or impossible), one can rule out entire classes of network interconnection patterns even when parameters are uncertain and mechanistic detail is incomplete.

A recurring theme throughout the vignettes has been that *sign structure* and *feedback organization* place sharp constraints on what transients can look like. In particular, monotone (balanced) architectures support strong qualitative predictions: when initialized at steady state, monotone input/output systems cannot produce certain transient signatures (for instance, a nondecreasing input cannot yield a biphasic output), and the influence of perturbations propagates in an unambiguous way through the network. When such signatures

are observed, the explanation often points to specific violations of monotonicity, most prominently incoherent feedforward (IFF) motifs and antagonistic multi-path influences operating on distinct time scales. The IFF viewpoint provides a unifying systems-level explanation for why non-monotonic and delayed responses are so common across biological scales, from intracellular regulation to population dynamics, and why modest interventions can have disproportionately large effects on peak outcomes.

Beyond transients induced by steps, the paper emphasized that *probing inputs* can be used as a discriminatory lens. Periodic and pulsed stimuli can expose dynamical regimes that are invisible in static dose-response curves, and can separate mechanistic alternatives that share identical steady-state input/output maps. Likewise, fold-change detection (scale invariance) and Weber-like behavior highlight the role of symmetries and invariances as organizing principles: when a network responds to *relative* changes rather than absolute levels, that property strongly constrains admissible model classes. Finally, cumulative dose and related integral-type readouts provide an additional experimentally tractable phenotype that can distinguish between fast adaptive suppression and true integration of exposure.

Several broader methodological messages emerge.

Dynamic phenotypes as “model class tests.” In settings where parameter identification is ill-posed, it is often more productive to ask which *qualitative* behaviors a model class can or cannot generate. Dynamic phenotypes can therefore be used as falsification criteria: a single carefully chosen input family (e.g., ramps of varying slope, periodic forcing across frequencies, paired pulses with variable spacing) may exclude large regions of model space even when data are limited.

Interconnection logic before detailed kinetics. Many conclusions can be drawn from the directed signed graph, time-scale separation, and the presence or absence of particular motifs (IFF, negative feedback, positive feedback, sequestration/competition). This supports a workflow in which coarse-grained interconnection hypotheses are tested and refined prior to committing to detailed biochemical kinetics.

Control-theoretic tools as a lingua franca. Casting biological circuits in the language of input/output systems allows one to import concepts such as monotonicity, incremental order preservation, invariance, and frequency response, not as literal engineering analogies, but as precise mathematical structures that cut across domains.

The viewpoint advocated here suggests several directions for future work.

- **Design of discriminating experiments.** A natural next step is to formalize, for broad model classes, which families of inputs are *maximally informative* for separating motifs that are indistinguishable under steps. This includes principled choices of frequencies, pulse patterns, and ramp rates, and quantitative notions of identifiability at the level of *network structure* rather than parameters.
- **Robustness of qualitative inference.** While sign-structure arguments are inherently robust to parametric uncertainty, measurements are noisy and often indirect. Developing theory that connects qualitative constraints (e.g., impossibility of biphasic responses under monotonicity assumptions) to finite-data statistical tests is an important open problem.
- **Near-monotone networks and “distance to monotonicity.”** Biological networks often appear close to being monotone/balanced, yet small violations can create qualitatively new behaviors. Understanding how dynamic phenotypes degrade as one moves away from monotonicity, and how to quantify

this “distance” in ways that predict dynamical complexity, remains a rich area for both theory and computation.

- **Bridging levels of description.** Many of the most compelling biological examples involve multi-scale effects (molecular regulation → cellular decisions → population dynamics). A systematic theory of how dynamic phenotypes compose across scales, and how coarse-grained motifs emerge from fine-grained interactions, would significantly strengthen the use of these ideas in practice.

In summary, transient behaviors and input-driven response patterns should be viewed as objects of study in systems biology: they encode function, they reveal mechanism, and they provide a route to model discrimination that is often more realistic than full parameter identification. By emphasizing dynamic phenotypes and the structural constraints imposed by interconnection logic, the paper aims to contribute to a toolkit for reasoning about complex biological networks in a manner that is both mathematically principled and experimentally actionable.

7 Acknowledgment

This work was supported in part by grants AFOSR FA9550-21-1-0289 and FA9550-22-1-0316.

Appendices

A Sketch of proof of monotone-response theorem

We start by “pruning” those state variables x_j which do not lie in any path from the input node to the output node x_n . We now formalize this construction, which is analogous to the “Kalman decomposition” reduction to minimal systems in linear control theory [113]. We start by splitting the set of variables X into four disjoint subsets of variables $x = (x, y, z, w)$, as follows:

1. the output node x_n is a component of the vector x ,
2. the components of x are reachable and observable,
3. the components of y are observable but not reachable,
4. the components of z are reachable but not observable, and
5. the components of w are neither reachable nor observable.

We assume without loss of generality that the output node x_n is in the first set of variables, x , since otherwise there would be no path from the input to the output, and the output is then constant when starting from a steady state. It is clear that, with this partition, the equations look as follows:

$$\begin{aligned}\dot{x} &= f(x, y, u) \\ \dot{y} &= g(y) \\ \dot{z} &= h(x, y, z, w, u) \\ \dot{w} &= k(y, w)\end{aligned}$$

(for example, there cannot be a z nor w dependence in f and in g , since otherwise the z and/or w variables would be observable).

To prove the Theorem, we need to show, for the original system $\dot{x} = f(x, u)$, that if we start from a steady state $f(x_0, u_0) = 0$ and if $u(t)$ is monotonic in time, with $u(0) = u_0$, then x_n will be also monotonic in time (with the same, or opposite, monotonic behavior depending on parity). Write $x_0 = (x_0, y_0, z_0, w_0)$, so $f(x_0, u_0) = 0$ means that $f(x_0, y_0, u_0) = g(y_0) = h(x_0, y_0, z_0, w_0, u_0) = k(y_0, w_0) = 0$.

The assumption that all directed paths from the input node u to the output node x_n have the same parity applies also to the subsystem given by the variables in x in which the y variables are set to y_0 :

$$\dot{x} = \hat{f}(x, u) = f(x, y_0, u) \tag{2}$$

with initial state $x(0) = x_0$, because partial derivatives of \hat{f} with respect to x and u are also partial derivatives of the original f .

Suppose that we have already proved the theorem for this subsystem in which all variables are reachable and observable. We claim next that the same is then true for the original system. Consider the solution $x(t)$ of (2) with input $u = u(t)$ and $x(0) = x_0$. Consider also the solution of the full system $\dot{x} = f(x, u)$ with $x(0) = x_0$ and the same input u , and write it in the corresponding block form

$$x(t) = (\xi(t), \psi(t), \zeta(t), \omega(t)).$$

We want to prove that $\xi(t) = x(t)$ for all $t \geq 0$, from which the claim will follow. But this just follows because $g(y_0) = 0$ implies that $y(t) \equiv y_0$. (Note that the variables $\zeta(t)$ and $\omega(t)$ do not affect the output variable, which is a component of $\xi(t)$.)

We now prove the theorem for the x -subsystem, for which all variables are reachable and observable. For ease of notation, we will write \hat{f} simply as f , use n for the size of x , and assume that the output node is x_n . Pick any index $i \in \{1, \dots, n\}$. By reachability, there is at least one path π from the input to x_i and, if $i < n$, then by observability there is at least one path θ from x_i to the output node x_n . We claim that every other path π' from the input to x_i has the same parity as π . Suppose without loss of generality that the parity of π is $+1$. We need to see that every other path π' from the input to x_i also has parity $+1$. If $i = n$, this is true by assumption (all paths from input to output have the same parity). So assume $i < n$. Suppose that π' has parity -1 . Then, the path $\pi\theta$ obtained by first following π and then following θ has parity $(+1) * \rho = \rho$, where ρ is the parity of θ , and the path $\pi'\theta$ obtained by first following π' and then following θ has parity $(-1) * \rho = -\rho$. So we have two paths from input to output with different parity, which contradicts the assumption of the Theorem. In conclusion, every two paths from the input to any given node have the same parity.

We assign a label with values “ $+1$ or -1 ” σ_u and σ_i , $i = 1, \dots, n$, to the nodes u and each node x_1, \dots, x_n respectively, as follows: $\sigma_u := +1$, $\sigma_i :=$ sign of any path from u to x_i . A key observation is that, if $\varphi_{ij} = +1$ then $\sigma_i = \sigma_j$, and if $\gamma_i = +1$ then $\sigma_u = \sigma_i$. Indeed, if we have a path π from the input to x_i , then a path π' can be obtained, from the input to x_j , by simply adjoining the edge from i to j , which has parity equal to the parity of π . Since σ_j is the sign of any path from the input to x_j , it follows that $\sigma_i = \sigma_j$, as claimed. The statement for $\gamma_i = +1$ is simply (since we defined $\sigma_u := +1$) that $\sigma_i = +1$ if the one-step path from the input to node x_i has parity 1, which means that all paths have this parity. Similarly, if $\varphi_{ij} = -1$ then $\sigma_i = -\sigma_j$, and if $\gamma_i = -1$ then $\sigma_u = -\sigma_i$.

Now make the change of variables $x_i \mapsto \sigma_i x_i$ (i.e., reverse the sign of variables with a “ -1 ” label). Writing the system in the new variables, we have now that

$$\frac{\partial f_i}{\partial u}(x, u) \geq 0 \quad \text{and} \quad \frac{\partial f_j}{\partial x_i}(x, u) \geq 0$$

for all $i = 1, \dots, n$ and all $i, j = 1, \dots, n$ respectively. Thus in the new variables we have what is called a *cooperative system* [111].

We must prove that, if $u = u(t)$ is a monotonically increasing input for a cooperative system, and if $x(0) = x_0$ is a steady state $f(x_0, u_0) = 0$, then every coordinate $x_i(t)$ of $x(t)$ (and, in particular, the output node) is monotonically increasing as well. (In the original coordinates, before sign reversals, $x_i(t)$ will decrease if $\sigma_i = -1$.) Similarly if $u = u(t)$ is a monotonically decreasing input for a cooperative system, and if $x(0) = x_0$ is a steady state $f(x_0, u_0) = 0$, then every coordinate $x_i(t)$ of $x(t)$ (and, in particular, the output node) is monotonically decreasing as well. We prove the increasing statement, since the second statement is proved analogously. From now on, for any two vectors $a, b \in \mathbb{R}^n$, we write simply $a \leq b$ to mean that $a_i \leq b_i$ for each $i = 1, \dots, n$.

We let $\varphi(t, x_0, v)$ denote the solution of $\dot{x} = f(x, u)$ at time $t > 0$ with initial condition $x(0) = x_0$ and input signal $v = v(t)$. *Kamke's Comparison Theorem* (see [111] for systems without inputs, and [9] for an extension to systems with inputs), asserts as follows: Let $y(t)$ and $z(t)$ be two solutions of the system $\dot{x} = f(x, u)$ corresponding, respectively, to an input $v(t)$ and an input $w(t)$. Suppose that $y(0) \leq z(0)$ and that $v(t) \leq w(t)$ for all $t \geq 0$. Then, $y(t) \leq z(t)$ for all $t \geq 0$.

Now pick an input v that is non-decreasing in time and an initial state x_0 that is a steady state with respect to $v_0 = v(0)$, that is, $f(x_0, v_0) = 0$. Since $v(t)$ is non-decreasing, we have that $v(t) \geq v(0)$ so that, by

comparison with the input that is identically equal to $v(0)$, we know that

$$\varphi(h, x_0, v) \geq \varphi(h, x_0, v_0)$$

for all $h \geq 0$, where, by a slight abuse of notation, “ v_0 ” is the function that has the constant value v_0 . We used the comparison theorem with respect to inputs and with the same initial state. The assumption that the system starts at a steady state gives that $\varphi(h, x_0, v_0) = x_0$ for all $h \geq 0$. Therefore:

$$x(h) \geq x(0) \quad \text{for all } h \geq 0. \quad (3)$$

Next, we consider any two times $t \leq t + h$. We wish to show that $x(t) \leq x(t + h)$. Using (3) and the comparison theorem now applied with respect to initial states and the same input, we have that:

$$x(t + h) = \varphi(t, x(t), v_h) \geq \varphi(t, x(0), v_h),$$

where v_h is the “tail” of v , defined by: $v_h(s) = v(s + h)$. On the other hand, since the function v is non-decreasing, it holds that $v_h \leq v$, in the sense that the inputs are ordered: $v_h(t) \leq v(t)$ for all $t \geq 0$. Therefore, using once again the comparison theorem with respect to inputs and with the same initial state, we have that

$$\varphi(t, x(0), v_h) \geq \varphi(t, x(0), v) = x(t)$$

and thus we proved that $x(t + h) \geq x(t)$. So x is a non-decreasing function. This concludes the proof.

Sometimes we only care about conditional monotonicity, depending on monotonic behavior of a particular node, even if the input is not monotonic. The following theorem from [16] is useful in that context.

Theorem. If the system is initially in steady state, the response of the output $x_n(t)$ will monotonically increase or decrease in time in response to changes in the input $u(t)$ if all the directed paths from the input nodes to the output node pass through an internal node $x_i(t)$ with monotonically increasing or decreasing dynamics and all the directed paths from input node $x_i(t)$ to the output node $x_n(t)$ have the same parity. Furthermore, monotonically increasing (decreasing) $x_i(t)$ will trigger monotonic increase (respectively, decrease) of $x_n(t)$ if parity is positive or will trigger monotonic decrease (respectively, increase) if parity is negative.

A proof is as follows. The assumption that all directed paths from the input node u to the output node x_n must pass through the internal node x_i can be formalized by splitting the set of nodes x into three subsets, $x = (x, y, z)$, where the components of x are those nodes x_j , $j \neq i$, for which there is at least one path from the input node u to x_j which does not pass through node x_i , $y = x_i$, and the components of z are all remaining nodes, including x_n . For this partition, the equations look as follows:

$$\begin{aligned} \dot{x} &= f(x, y, z, u) \\ \dot{y} &= g(x, y, z, u) \\ \dot{z} &= h(z, y) \end{aligned}$$

because, if there were any dependence of h on some coordinate x_j , then there would be a path from the input to some component of z (follow a path to x_j and concatenate it with an edge from x_j to this component).

The condition that all the directed paths from $y = x_i$ to the output node x_n have the same parity means that in the system $\dot{z} = h(z, v)$ (where we now view $y(t)$ as an input, which we write as “ $v(t)$ ” to avoid confusion) all paths from the input to the output have the same parity, as in the hypothesis of the Theorem. Suppose that we consider an input u , starting from a steady state (x_0, y_0, z_0) . Think of $v(t) = y(t)$ as an input. Since we started from a steady state, we know that $h(v(0), z_0) = 0$. Thus, if $v(t)$ is monotonic, the

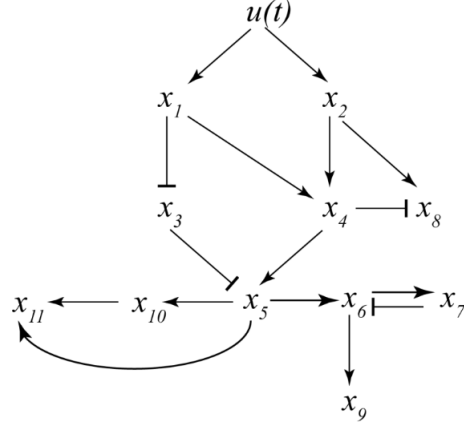


Figure 44: Example to illustrate monotone dependence results, from [16].

previous theorem gives us that the output is monotonic, increasing or decreasing depending on parity and on the increasing or decreasing character of the input.

For example, on the system shown in Fig. 44, the first theorem allows us to conclude that monotonically increasing input $u(t)$ will ensure monotonic increase of $x_1, x_2, x_4, x_5, x_{10}, x_{11}$ (since all directed paths from u to the respective node have positive parity), and monotonic decrease is ensured for x_3 , but monotonicity cannot be guaranteed for x_6, x_7, x_8, x_9 . On the other hand, if we do not know whether input signal $u(t)$ is monotonic or in case an additional negative path in the network from $u(t)$ to x_5 is added, we may still use the second formulation to conclude that if $x_5(t)$ is monotonic so will be x_{10} and x_{11} . Indeed, all the paths to x_{10} and x_{11} from input $u(t)$ pass through x_5 and all the paths from x_5 to x_{10} and x_{11} have positive parity. The argument does not work for x_9 due to a negative feedback loop between x_6 and x_7 (a directed path that goes around this loop will have the opposite parity from the path that does not).

B Sketch of proofs of entrainment

Feedforward systems. Consider first purely feedforward systems, meaning that the state variables x_i , $i = 1, \dots, n$, satisfy the property that if x_i influences x_j , then x_j does not influence x_i . One can always re-label variables in such a way that no element x_i influences any element x_j with $j < i$. In this form the system has a cascade structure, that is to say the Jacobian ($J_{ij} = \partial f_i / \partial x_j$) is lower triangular. Let us make the following mild (and reasonable for biological systems) assumptions on trajectories, given an input u : (i) solutions are bounded ($x_i(t) \leq c_i$ for some $c_i > 0$) for all t ; (ii) the diagonal elements of J are negative ($\partial f_i / \partial x_i < 0$), which means biologically that every species is degraded, typically in a concentration-dependent manner such as a linear degradation term like $-k_i x_i$ or a Michaelis-Menten term like $-k_i x_i^M / (1 + x_i^M / x_{i0}^M)$, where M is a Hill coefficient; (iii) the off-diagonal elements of J are bounded, i.e., all $|J_{ij}| \leq p_{\max}$ for some $p_{\max} > 0$. Similar conditions are imposed in [102] for analyzing cascades of enzymatic and gene transcription networks.

Suppose from now on that the input u is T -periodic. Then the system has a unique periodic solution with period T (same as stimulus), to which every other solution converges. The proof consists of choosing a diagonal matrix P with $P_{ii} = 1/p^i$, so as to make the off-diagonal elements of PJP^{-1} arbitrarily close to zero, the larger that $p \gg p_{\max}$ is. Then, the matrix measures μ_1, μ_2 , or μ_{∞} , associated with the L^1, L^2 , or L^{∞} -norms, respectively, of PJP^{-1} are all approximately equal to the largest (i.e. least negative) diagonal element. Thus, the system is infinitesimally contracting and, by results of [79] (see also proofs in Theorem

2 in [102] or [117]), we conclude that all $x_i(t)$ are T -periodic, as claimed.

Cooperative systems. For systems that are not feedforward, there are entrainment results as well, as long as all loops are positive. We now sketch the case of monotone systems and equilibrium initial states. We refer the reader to [95] for a sketch of proof that cascades of monotone and feedforward systems preserve entrainment.

An important result for periodically forced monotone systems $\dot{x} = f(x(t), u(t))$ is given as Theorem 5.26 in [60], which credits the unpublished 1997 Ph.D. thesis by I. Těšćak. This result applies to systems that are irreducible, meaning that all its Jacobian matrices are irreducible (that is, every variable can indirectly affect every other variable, possibly through an arbitrary number of intermediates; see also [59]). The result states that, assuming bounded trajectories, $x(t)$ converges to a solution with period kT , where $k \geq 1$ is an integer, for almost all initial conditions if the stimulus $u(t)$ is periodic with period T ($u(t) = u(t + T)$) and if the system is dissipative (trajectories are ultimately bounded). It is important to note that, generally, there may be stable periodic solutions with period kT and $k > 1$, as shown in [125]. Thus, if we are interested in entrainment (global convergence to period- T trajectories), we need to find additional conditions which rule out $k > 1$. The simplest condition, which is enough for many applications, covers systems evolving on the nonnegative orthant (all variables are nonnegative) and starting from zero initial conditions. Since it seems difficult to find a reference, we state and prove a simple result.

We assume given a closed, convex, pointed cone $K \subset \mathbb{R}^n$, and define the partial order $x \leq_K y \Leftrightarrow y - x \in K$. Let us write $f(t, x)$ for the time-varying vector field $f(x, u(t))$, in which a periodic input has been specified. Thus, we more generally consider a nonautonomous system

$$\dot{x} = f(t, x), \quad (4)$$

where $f : \mathbb{R} \times \mathbb{R}^n \rightarrow \mathbb{R}^n$ is continuous in (t, x) and locally Lipschitz in x , is T -periodic in time: $f(t + T, x) = f(t, x)$, and the flow $\varphi(t, s, x)$ of (4) is monotone with respect to \leq_K , i.e.,

$$x_1 \leq_K x_2 \Rightarrow \varphi(t, s, x_1) \leq_K \varphi(t, s, x_2) \quad \forall t \geq s.$$

Theorem. Let $x(t) = \varphi(t, 0, x_0)$ be a solution of (4) that is bounded for $t \geq 0$ and satisfies

$$x_0 \leq_K x(t) \quad \text{for all } t \geq 0.$$

Then $x(t)$ converges to a T -periodic solution of (4).

We reduce the proof to a discrete-time convergence lemma as follows:

Lemma. Let $F : \mathbb{R}^n \rightarrow \mathbb{R}^n$ be continuous and monotone with respect to \leq_K . Suppose that a bounded sequence

$$x_{k+1} = F(x_k), \quad k = 0, 1, 2, \dots$$

satisfies $x_k \leq_K x_{k+1}$ for all k . Then $\{x_k\}$ converges to some $\bar{x} \in \mathbb{R}^n$, and \bar{x} is a fixed point of F .

We prove this next. Boundedness implies precompactness in \mathbb{R}^n , so $\{x_k\}$ has convergent subsequences. Let

$$x_{k_j} \rightarrow a, \quad x_{\ell_j} \rightarrow b$$

be two convergent subsequences. Since both index sequences tend to infinity, we may pass to further subsequences (without relabeling) such that $k_j \leq \ell_j$ for all j . Monotonicity of the sequence gives

$$x_{k_j} \leq_K x_{\ell_j} \quad \text{for all } j.$$

Because K is closed, taking limits yields $a \leq_K b$. Reversing the roles of the subsequences gives $b \leq_K a$. Since K is pointed, we conclude $a = b$. Hence all convergent subsequences have the same limit, and therefore $x_k \rightarrow \bar{x}$ for some \bar{x} . Finally, continuity of F and the relation $x_{k+1} = F(x_k)$ imply

$$\bar{x} = \lim_{k \rightarrow \infty} x_{k+1} = \lim_{k \rightarrow \infty} F(x_k) = F(\bar{x}),$$

so \bar{x} is a fixed point of F . This completes the proof of the lemma.

To prove the theorem, we start by sampling the trajectory. Define $x_k := \varphi(kT, 0, x_0)$ for $k = 0, 1, 2, \dots$, and note that the semigroup property of the flow says that

$$x_{k+1} = \varphi((k+1)T, kT, x_k).$$

Next we define the time- T map (also called the period or stroboscopic map) associated with the periodic system,

$$F(\xi) := \varphi(T, 0, \xi).$$

Since

$$\varphi((k+1)T, kT, \xi) = \varphi(T, 0, \xi) \quad \forall \xi \in \mathbb{R}^n, \forall k,$$

it follows that $x_{k+1} = F(x_k)$ for all k . Monotonicity of the flow implies that F is monotone with respect to \leq_K , and continuity of the flow implies that F is continuous. The assumption $x_0 \leq_K x(t)$ for all $t \geq 0$ implies $x_k \leq_K x_{k+1}$ for all k . Boundedness of $x(t)$ implies boundedness of $\{x_k\}$. Thus the lemma can be applied, and we know that $x_k \rightarrow \bar{x}$ for some $\bar{x} \in \mathbb{R}^n$, and $F(\bar{x}) = \bar{x}$. Define $\bar{x}(t) := \varphi(t, 0, \bar{x})$. Using time periodicity,

$$\varphi(t + T, 0, \bar{x}) = \varphi(t, 0, \varphi(T, 0, \bar{x})) = \varphi(t, 0, \bar{x}),$$

so $\bar{x}(t)$ is T -periodic.

We must still show convergence of the full trajectory. Now, for any $t \in [0, T]$, $x(kT + t) = \varphi(t, 0, x_k)$. Continuity of the flow with respect to initial conditions and $x_k \rightarrow \bar{x}$ thus imply

$$x(kT + t) \rightarrow \bar{x}(t) \quad \text{as } k \rightarrow \infty.$$

Hence $x(t)$ converges to the T -periodic solution $\bar{x}(t)$.

We remark that periodicity of the vector field is essential for identifying the discrete dynamics with iterations of a single map F . Without periodicity, the step map $\varphi((k+1)T, kT, \cdot)$ would depend on k , and the Lemma would not apply.

References

- [1] A. K. Abbas, A. H. H. Lichtman, and S. Pillai. *Basic Immunology: Functions and Disorders of the Immune System, 5th Edition*. Elsevier, St. Louis, 2016.
- [2] D.K. Agrawal, R. Marshall, V. Noireaux, and E.D. Sontag. In vitro implementation of robust gene regulation in a synthetic biomolecular integral controller. *Nature Communications*, 10:1–12, 2019.
- [3] M.A. Al-Radhawi, M. Sadeghi, and E.D. Sontag. Long-term regulation of prolonged epidemic outbreaks in large populations via adaptive control: a singular perturbation approach. *IEEE Control Systems Letters*, 6:578–583, 2022.
- [4] U. Alon. Yeastnet. <http://www.weizmann.ac.il/mcb/UriAlon/Papers/networkMotifs/yeastData.mat>, 2002.
- [5] U. Alon. *An Introduction to Systems Biology: Design Principles of Biological Circuits*. Chapman & Hall, 2006.
- [6] U. Alon, M. G. Surette, N. Barkai, and S. Leibler. Robustness in bacterial chemotaxis. *Nature*, 397:168–171, 1999.
- [7] D. Angeli, G.A. Enciso, and E.D. Sontag. A small-gain result for orthant-monotone systems under mixed feedback. *Systems and Control Letters*, 68:9–19, 2014.
- [8] D. Angeli, J. E. Ferrell, and E.D. Sontag. Detection of multistability, bifurcations, and hysteresis in a large class of biological positive-feedback systems. *Proc Natl Acad Sci USA*, 101(7):1822–1827, 2004. A revision of Suppl. Fig. 7(b) is here: <http://sontaglab.org/FTPDIR/nullclines-f-g-REV.jpg>; and typos can be found here: <http://sontaglab.org/FTPDIR/angeli-ferrell-sontag-pnas04-errata.txt>.
- [9] D. Angeli and E.D. Sontag. Monotone control systems. *IEEE Trans. Automat. Control*, 48(10):1684–1698, 2003. Errata are here: <http://sontaglab.org/FTPDIR/angeli-sontag-monotone-TAC03-typos.txt>.
- [10] D. Angeli and E.D. Sontag. Interconnections of monotone systems with steady-state characteristics. In *Optimal control, stabilization and nonsmooth analysis*, volume 301 of *Lecture Notes in Control and Inform. Sci.*, pages 135–154. Springer, Berlin, 2004.
- [11] D. Angeli and E.D. Sontag. Multi-stability in monotone input/output systems. *Systems Control Lett.*, 51(3-4):185–202, 2004.
- [12] D. Angeli and E.D. Sontag. Remarks on the invalidation of biological models using monotone systems theory. In *Proc. IEEE Conf. Decision and Control, Maui, Dec. 2012*, 2012. Paper TuC09.3.
- [13] S. K. Aoki, G. Lillacci, A. Gupta, A. Baumschlager, D. Schweingruber, and M. Khammash. A universal biomolecular integral feedback controller for robust perfect adaptation. *Nature*, 570(7762):533–537, 2019.
- [14] C. F. Arias, M. A. Herrero, J. A. Cuesta, F. J. Acosta, and C. Fernandez-Arias. The growth threshold conjecture: a theoretical framework for understanding T-cell tolerance. *R Soc Open Sci*, 2(7):150016, 2015.
- [15] J. P. Armitage and J. M. Lackie. *Biology of the Chemotactic Response (Edited Book)*. Cambridge University Press, Cambridge, UK, 1990.

- [16] J.A. Ascensao, P. Datta, B. Hancioglu, E.D. Sontag, M.L. Gennaro, and O.A. Igoshin. Non-monotonic response dynamics of glyoxylate shunt genes in mycobacterium tuberculosis. *PLoS Computational Biology*, 12:e1004741, 2016.
- [17] H. C. Berg and D. A. Brown. Chemotaxis in *Escherichia coli* analysed by three-dimensional tracking. *Nature*, 239:500–504, 1972.
- [18] Howard C. Berg. Motile behavior of bacteria. *Physics Today*, 53(1):24–29, January 2000.
- [19] M. Bin, J. Huang, A. Isidori, L. Marconi, M. Mischiati, and E. D. Sontag. Internal models in control, bioengineering, and neuroscience. *Annual Review of Control, Robotics, and Autonomous Systems*, 5:20.1–20.25, 2022.
- [20] A. Bizyaeva, A. Franci, and N.E. Leonard. Multitopic belief formation through bifurcations over signed social networks. *IEEE Transactions on Automatic Control*, 70(8):5082–5097, 2025.
- [21] L. Bleris, Z. Xie, D. Glass, A. Adadevoh, E.D. Sontag, and Y. Benenson. Synthetic incoherent feed-forward circuits show adaptation to the amount of their genetic template. *Molecular Systems Biology*, 7:519–, 2011.
- [22] G. Bocharov, B. Ludewig, A. Bertoletti, P. Klenerman, T. Junt, P. Krebs, T. Luzyanina, C. Fraser, and R. M. Anderson. Underwhelming the immune response: effect of slow virus growth on CD8+T-lymphocyte responses. *J. Virol.*, 78(5):2247–2254, Mar 2004.
- [23] D. Bray. Bacterial chemotaxis and the question of gain. *Proc. Natl. Acad. Sci. U.S.A.*, 99:7–9, 2002.
- [24] A. W. Burks, S. M. Jones, R. A. Wood, D. M. Fleischer, S. H. Sicherer, R. W. Lindblad, D. Stablein, A. K. Henning, B. P. Vickery, A. H. Liu, A. M. Scurlock, W. G. Shreffler, M. Plaut, and H. A. Sampson. Oral immunotherapy for treatment of egg allergy in children. *N. Engl. J. Med.*, 367(3):233–243, Jul 2012.
- [25] F.M Burnet. A modification of jerne's theory of antibody production using the concept of clonal selection. *Aust J Sci.*, 20:67–69, 1957.
- [26] M. Cartwright and M.A. Husain. A model for the control of testosterone secretion. *J. Theor. Biol.*, 123:239–250, 1986.
- [27] S. Cho and Y.-R. Yoon. Understanding the pharmacokinetics of prodrug and metabolite. *Translational and Clinical Pharmacology*, 26(1):1–5, 2018.
- [28] O. Cinquin and J. Demongeot. Positive and negative feedback: striking a balance between necessary antagonists. *J. Theor. Biol.*, 216:229–241, 2002.
- [29] C. Cohen-Saidon, A. A. Cohen, A. Sigal, Y. Liron, and U. Alon. Dynamics and variability of ERK2 response to EGF in individual living cells. *Molecular Cell*, pages 885–893, 2009.
- [30] S. Coogan. Mixed monotonicity for reachability and safety in dynamical systems. In *2020 59th IEEE Conference on Decision and Control (CDC)*, pages 5074–5085, 2020.
- [31] S. Coogan and M. Arcak. Efficient finite abstraction of mixed monotone systems. In *Proceedings of the 18th International Conference on Hybrid Systems: Computation and Control*, HSCC '15, page 58–67, New York, NY, USA, 2015. Association for Computing Machinery.

[32] M. C. Costanzo, M. E. Crawford, J. E. Hirschman, J. E. Kranz, P. Olsen, L. S. Robertson, M. S. Skrypek, B. R. Braun, K. L. Hopkins, P. Kondu, C. Lengieza, J. E. Lew-Smith, M. Tillberg, and J. I. Garrels. YPDTM, PombePDTM and WormPDTM: model organism volumes of the BioKnowledgeTM Library, an integrated resource for protein information. *Nucl. Acids Res.*, 29(1):75–79, 2001.

[33] E.N. Dancer. Some remarks on a boundedness assumption for monotone dynamical systems. *Proc. of the AMS*, 126:801–807, 1998.

[34] B. DasGupta, G.A. Enciso, E.D. Sontag, and Y. Zhang. Algorithmic and complexity aspects of decompositions of biological networks into monotone subsystems. *BioSystems*, 90:161–178, 2007.

[35] P. Datta, L. Shi, N. Bibi, G. Balazsi, and M. L. Gennaro. Regulation of central metabolism genes of *Mycobacterium tuberculosis* by parallel feed-forward loops controlled by sigma factor E (σ (E)). *J. Bacteriol.*, 193(5):1154–1160, Mar 2011.

[36] D.L. DeAngelis, W.M. Post, and C.C. Travis. *Positive Feedback in Natural Systems*. Springer-Verlag, New York, 1986.

[37] L. Edelstein-Keshet. *Mathematical Models in Biology*. SIAM, Philadelphia, 2005.

[38] L. Edelstein-Keshet and A. Spiros. Exploring the formation of alzheimer’s disease senile plaques in silico. *Journal of Theoretical Biology*, 216(3):301 – 326, 2002.

[39] G.A. Enciso, H.L. Smith, and E.D. Sontag. Non-monotone systems decomposable into monotone systems with negative feedback. *J. of Differential Equations*, 224:205–227, 2006.

[40] G.A. Enciso and E.D. Sontag. On the stability of a model of testosterone dynamics. *J. Math. Biol.*, 49(6):627–634, 2004.

[41] G.A. Enciso and E.D. Sontag. Global attractivity, I/O monotone small-gain theorems, and biological delay systems. *Discrete Contin. Dyn. Syst.*, 14(3):549–578, 2006.

[42] M. G. Frank and M. V. Baratta. Use of an immunocapture device to detect cytokine release in discrete brain regions. *Neural Regen Res.*, 19:703–704, 2024. doi: 10.4103/1673-5374.382237.

[43] P. A. Gatenby, A. Basten, and P. Creswick. Sneaking through: a T-cell-dependent phenomenon. *Br. J. Cancer*, 44(5):753–756, 1981.

[44] L. Goentoro and M. W. Kirschner. Evidence that fold-change, and not absolute level, of β -catenin dictates Wnt signaling. *Molecular Cell*, 36:872–884, 2009.

[45] A. Goldbeter. *Biochemical Oscillations and Cellular Rhythms*. Cambridge University Press, Cambridge, 1996.

[46] J.-L. Gouze and K. P. Hadeler. Monotone flows and order intervals. *Nonlinear World*, 1:23–34, 1994.

[47] J.L. Gouze. Positive and negative circuits in dynamical systems. *J. Biol. Sys.*, 6:11–15, 1998.

[48] Z. Grossman and G. Berke. Tumor escape from immune elimination. *J. Theor. Biol.*, 83(2):267–296, Mar 1980.

[49] Z. Grossman and W. E. Paul. Adaptive cellular interactions in the immune system: the tunable activation threshold and the significance of subthreshold responses. *Proc. Natl. Acad. Sci. U.S.A.*, 89(21):10365–10369, 1992.

[50] A. Gupta and E. D. Sontag. Cumulative dose responses for adapting biological systems. *Royal Society Interface*, 22:20240877, 2025.

[51] K. Hadeler and D. Glas. Quasimonotone systems and convergence to equilibrium in a population genetics model. *J. Math. Anal. Appl.*, 95:297–303, 1983.

[52] S. Hastings, J. Tyson, and D. Webster. Existence of periodic solutions for negative feedback cellular control systems. *J. Diff. Eqs.*, 25:39–64, 1977.

[53] E. A. Hernandez-Vargas, G. Giordano, E.D. Sontag, J. G. Chase, H. Chang, and A. Astolfi. First special section on systems and control research efforts against covid-19 and future pandemics. *Annual Reviews in Control*, 50:343–344, 2020.

[54] E. A. Hernandez-Vargas, G. Giordano, E.D. Sontag, J. G. Chase, H. Chang, and A. Astolfi. Second special section on systems and control research efforts against covid-19 and future pandemics. *Annual Reviews in Control*, 51:424–425, 2021.

[55] E. A. Hernandez-Vargas, G. Giordano, E.D. Sontag, J. G. Chase, H. Chang, and A. Astolfi. Third special section on systems and control research efforts against covid-19 and future pandemics. *Annual Reviews in Control*, 52:446–447, 2021.

[56] M. Hirsch. Differential equations and convergence almost everywhere in strongly monotone flows. *Contemporary Mathematics*, 17:267–285, 1983.

[57] M. Hirsch. Systems of differential equations that are competitive or cooperative ii: Convergence almost everywhere. *SIAM J. Mathematical Analysis*, 16:423–439, 1985.

[58] M. Hirsch and H.L. Smith. Monotone dynamical systems. In *Handbook of Differential Equations, Ordinary Differential Equations (second volume)*. Elsevier, Amsterdam, 2005.

[59] M. W. Hirsch and H. Smith. *Competitive and Cooperative Systems: A Mini-review*, pages 183–190. Springer Berlin Heidelberg, Berlin, Heidelberg, 2003.

[60] M. W. Hirsch and H. Smith. *Monotone dynamical systems*, page 239–357. Elsevier B. V., Amsterdam, 2005.

[61] F. Hüffner, N. Betzler, and R. Niedermeier. Optimal edge deletions for signed graph balancing. In *Proceedings of the 6th Workshop on Experimental Algorithms (WEA07), June 6-8, 2007, Rome*. Springer-Verlag, 2007.

[62] P. Johansen, T. Storni, L. Rettig, Z. Qiu, A. Der-Sarkissian, K. A. Smith, V. Manolova, K. S. Lang, G. Senti, B. Mullhaupt, T. Gerlach, R. F. Speck, A. Bot, and T. M. Kundig. Antigen kinetics determines immune reactivity. *Proc. Natl. Acad. Sci. U.S.A.*, 105(13):5189–5194, Apr 2008.

[63] S. Kaplan, A. Bren, E. Dekel, and U. Alon. The incoherent feed-forward loop can generate non-monotonic input functions for genes. *Molecular Systems Biology*, 4:203, 2008.

[64] J.P. Keener and J. Sneyd. *Mathematical Physiology*. Springer-Verlag, New York, 1998.

[65] E. F. Keller and L. A. Segel. Initiation of slime mold aggregation viewed as an instability. *J. Theor. Biol.*, 26:399–415, 1970.

[66] M.H. Khammash. Perfect adaptation in biology. *Cell Systems*, 12(6):509–521, 2021.

[67] B.N. Kholodenko. Negative feedback and ultrasensitivity can bring about oscillations in the mitogen-activated protein kinase cascades. *Eur. J. Biochem*, 267:1583–1588, 2000.

[68] T.J. Kindt, R.A. Goldsby, B.A. Osborne, and J. Kuby. *Kuby Immunology*, 7th ed. W.H. Freeman and Company, New York, 2013.

[69] M. Kollmann, L. Lovdok, K. Bartholome, J. Timmer, and V. Sourjik. Design principles of a bacterial signalling network. *Nature*, 438:504–507, 2005.

[70] T. Kundig, A. Bot, K.A. Smith, and Z. Qiu. A method for enhancing T cell response, August 21 2008. CA Patent App. CA 2,678,353.

[71] J. Larsch, S. W. Flavell, Q. Liu, A. Gordus, D. R. Albrecht, and C. I. Bargmann. A circuit for gradient climbing in *C. elegans* chemotaxis. *Cell Rep.*, 12(11):1748–1760, 2015.

[72] S. H. Larsen, R. W. Reader, E. N. Kort, W. W. Tso, and J. Adler. Change in direction of flagellar rotation is the basis of the chemotactic response in *Escherichia coli*. *Nature*, 249:74–77, 1974.

[73] M. D. Lazova, T. Ahmed, D. Bellomo, R. Stocker, and T. S. Shimizu. Response-rescaling in bacterial chemotaxis. *Proc Natl Acad Sci U.S.A.*, 108:13870–13875, 2011.

[74] G. Leclercq-Cohen, N. Steinhoff, L. Albertí Servera, S. Nassiri, S. Danilin, E. Piccione, E. Yángüez, T. Hüsser, S. Herter, S. Schmeing, P. Gerber, P. Schwalie, J. Sam, S. Briner, S. Jenni, R. Bianchi, M. Biehl, F. Cremasco, K. Apostolopoulou, H. Haegel, C. Klein, P. Umaña, and M. Bacac. Dissecting the mechanisms underlying the cytokine release syndrome (CRS) mediated by T-cell bispecific antibodies. *Clinical Cancer Research*, 29(21):4449–4463, 2023.

[75] J. Lewis, J.M. Slack, and L. Wolpert. Thresholds in development. *J. Theor. Biol.*, 65:579–590, 1977.

[76] L. Li, X. Li, L. Xu, Y. Sheng, and J. Huang. Systematic evaluation of dose accumulation studies in clinical pharmacokinetics. *Current Drug Metabolism*, 14(5):507–513, 2013.

[77] M. Li and G. L. Hazelbauer. Cellular stoichiometry of the components of the chemotaxis signaling complex. *J. Bacteriol.*, 186:3687–3694, 2004.

[78] Ann E. Lin. Recognizing and profiling t cell receptors. Crown Bioscience Blog, March 2019. Accessed: 2025-12-24.

[79] W. Lohmiller and J. J. E. Slotine. On contraction analysis for non-linear systems. *Automatica*, 34:683–696, 1998.

[80] A. Maayan, R. Iyengar, and E.D. Sontag. Intracellular regulatory networks are close to monotone systems. *IET Systems Biology*, 2:103–112, 2008.

[81] S. Magi, K. Iwamoto, and M. Okada-Hatakeyama. Current status of mathematical modeling of cancer – from the viewpoint of cancer hallmarks. *Current Opinion in Systems Biology*, 2:39 – 48, 2017.

[82] S. Mangan and U. Alon. Structure and function of the feed-forward loop network motif. *Proc. Natl. Acad. Sci. USA*, 110:11980–11985, 2003.

[83] S. Mangan, A. Zaslaver, and U. Alon. The coherent feedforward loop serves as a sign-sensitive delay element in transcription networks. *J. Molec. Bio.*, 334:197–204, 2003.

[84] R. Milo, S. Shen-Orr, S. Itzkovitz, N. Kashtan, D. Chklovskii, and U. Alon. Network motifs: Simple building blocks of complex networks. *Science*, 298:824–827, 2002.

[85] J. Monod and F. Jacob. Teleonomic mechanisms in cellular metabolism, growth and differentiation,. *Cold Spring Harb. Symp. Quant. Biol.*, 26:389–401, 1961.

[86] J.D. Murray. *Mathematical Biology, I, II: An introduction*. Springer-Verlag, New York, 2002.

[87] D. Muzzey, C. A. Gómez-Uribe, J.T. Mettetal, and A. van Oudenaarden. A systems-level analysis of perfect adaptation in yeast osmoregulation. *Cell*, 138(1):160–171, 2009.

[88] E.V. Nikolaev, S.J. Rahi, and E.D. Sontag. Chaos in simple periodically-forced biological models. *Biophysical Journal*, 114:1232–1240, 2018.

[89] A. Novic and M. Weiner. Enzyme induction as an all-or-none phenomenon. *Proc. Natl. Acad. Sci. U.S.A.*, 43:553–566, 1957.

[90] E. Plahte, T. Mestl, and W.S. Omholt. Feedback circuits, stability and multistationarity in dynamical systems. *J. Biol. Sys.*, 3:409–413, 1995.

[91] J. R. Pomerening, E.D. Sontag, and J. E. Ferrell. Building a cell cycle oscillator: hysteresis and bistability in the activation of cdc2. *Nature Cell Biology*, 5(4):346–351, 2003. Supplementary materials 2-4 are here: <http://sontaglab.org/FTPDIR/pomerening-sontag-ferrell-additional.pdf>.

[92] T. Pradeu. *The Limits of the Self. Immunology and Biological Identity*. Oxford University Press, 2012.

[93] T. Pradeu, S. Jaeger, and E. Vivier. The speed of change: towards a discontinuity theory of immunity? *Nat. Rev. Immunol.*, 13(10):764–769, 2013.

[94] M. Ptashne. *A Genetic Switch: Phage λ and Higher Organisms*. Cell Press and Blackwell Scientific Publications, Cambridge MA, 1992.

[95] S. J. Rahi, J. Larsch, K. Pecani, N. Mansouri, A. Y. Katsov, K. Tsaneva-Atanasova, E. D. Sontag, and F. R. Cross. Oscillatory stimuli differentiate adapting circuit topologies. *Nature Methods*, 14:1010–1016, 2017.

[96] P.E. Rapp. A theoretical investigation of a large class of biochemical oscillations. *Math Biosciences*, 25:165–188, 1975.

[97] E. Remy, B. Mosse, C. Chaouiya, and D. Thieffry. A description of dynamical graphs associated to elementary regulatory circuits. *Bioinformatics*, 19 (Suppl 2):ii172ii178, 2003.

[98] T. Riley, E.D. Sontag, P. Chen, and A. Levine. The transcriptional regulation of human p53-regulated genes. *Nature Reviews Molecular Cell Biology*, 9:402–412, 2008.

[99] T. Riley, X. Yu, E.D. Sontag, and A. Levine. The P53HMM algorithm: using novel profile Hidden Markov Models to detect p53-responsive genes. *BMC Bioinformatics*, 10:111, 2009.

[100] F. S. Roberts. *Graph Theory and Its Applications to Problems of Society*, volume 29 of *CBMS-NSF Regional Conference Series in Applied Mathematics*. Society for Industrial and Applied Mathematics (SIAM), Philadelphia, 1977.

[101] S. Roberts, K. Quealy, and M. Sanger-Katz. Flattening the coronavirus curve: one chart explains why slowing the spread is nearly as important as stopping it. The New York Times, 2020. Accessed: 2025-12-26.

[102] G. Russo, M. di Bernardo, and E.D. Sontag. Global entrainment of transcriptional systems to periodic inputs. *PLoS Computational Biology*, 6:e1000739, 2010.

[103] L.A. Segel. *Modeling dynamic phenomena in molecular and cellular biology*. Cambridge University Press, Cambridge, 1984.

[104] L. Seymour, J. Bogaerts, A. Perrone, R. Ford, L. H. Schwartz, S. Mandrekar, N. U. Lin, S. Litière, J. Dancey, A. Chen, F. S. Hodi, P. Therasse, O. S. Hoekstra, L. K. Shankar, and J. D. Wolchok. irecist: guidelines for response criteria for use in trials testing immunotherapeutics. *The Lancet Oncology*, 18(3):e143–e152, 2017.

[105] W. Sha, J. Moore, K. Chen, A.D. Lassaletta, C.S. Yi, J.J. Tyson, and J.C. Sible. Hysteresis drives cell-cycle transitions in *xenopus laevis* egg extracts. *Proc. Natl. Acad. Sci. USA*, 100:975–980, 2003.

[106] L. Shi, Y. J. Jung, S. Tyagi, M. L. Gennaro, and R. J. North. Expression of Th1-mediated immunity in mouse lungs induces a *Mycobacterium tuberculosis* transcription pattern characteristic of nonreplicating persistence. *Proc. Natl. Acad. Sci. U.S.A.*, 100(1):241–246, Jan 2003.

[107] T. S. Shimizu, Y. Tu, and H. C. Berg. A modular gradient-sensing network for chemotaxis in *Escherichia coli* revealed by responses to time-varying stimuli. *Mol. Syst. Biol.*, 6:382, 2010.

[108] O. Shoval, U. Alon, and E.D. Sontag. Symmetry invariance for adapting biological systems. *SIAM Journal on Applied Dynamical Systems*, 10:857–886, 2011. (See here for a small typo: <http://www.sontaglab.org/FTPDIR/shoval.alon.sontag.erratum.pdf>).

[109] O. Shoval, L. Goentoro, Y. Hart, A. Mayo, E.D. Sontag, and U. Alon. Fold change detection and scalar symmetry of sensory input fields. *Proc Natl Acad Sci USA*, 107:15995–16000, 2010.

[110] M. Skataric and E.D. Sontag. A characterization of scale invariant responses in enzymatic networks. *PLoS Computational Biology*, 8:e1002748, 2012.

[111] H. Smith. *Monotone Dynamical Systems: An Introduction to the Theory of Competitive and Cooperative Systems, Mathematical Surveys and Monographs*, vol. 41. AMS, Providence, RI, 1995.

[112] W.R. Smith. Hypothalamic regulation of pituitary secretion of luteinizing hormone. II. Feedback control of gonadotropin secretion. *Bull Math. Biol.*, 42:57–78, 1980.

[113] E.D. Sontag. *Mathematical Control Theory. Deterministic Finite-Dimensional Systems*, volume 6 of *Texts in Applied Mathematics*. Springer-Verlag, New York, second edition, 1998.

[114] E.D. Sontag. Adaptation and regulation with signal detection implies internal model. *Systems Control Lett.*, 50(2):119–126, 2003.

[115] E.D. Sontag. Monotone and near-monotone biochemical networks. *Systems and Synthetic Biology*, 1:59–87, 2007.

[116] E.D. Sontag. An observation regarding systems which converge to steady states for all constant inputs, yet become chaotic with periodic inputs. Technical report, arxiv 0906.2166, 2009.

[117] E.D. Sontag. Contractive systems with inputs. In Jan Willems, Shinji Hara, Yoshito Ohta, and Hisaya Fujioka, editors, *Perspectives in Mathematical System Theory, Control, and Signal Processing*, pages 217–228. Springer-verlag, 2010.

[118] E.D. Sontag. Remarks on invariance of population distributions for systems with equivariant internal dynamics, 2011.

[119] E.D. Sontag. A dynamical model of immune responses to antigen presentation predicts different regions of tumor or pathogen elimination. *Cell Systems*, 4:231–241, 2017.

[120] E.D. Sontag. An explicit formula for minimizing the infected peak in an SIR epidemic model when using a fixed number of complete lockdowns. *International Journal of Robust and Nonlinear Control, Special Issue on Control-Theoretic Approaches for Systems in the Life Sciences*, pages 1–24, 2021.

[121] E.D. Sontag, A. Veliz-Cuba, R. Laubenbacher, and A.S. Jarrah. The effect of negative feedback loops on the dynamics of boolean networks. *Biophysical Journal*, 95:518–526, 2008.

[122] V. Sourjik. Receptor clustering and signal processing in *E. coli* chemotaxis. *Trends in Microbiology*, 12(12):569 – 576, 2004.

[123] V. Sourjik and H. C. Berg. Binding of the *Escherichia coli* response regulator CheY to its target measured *in vivo* by fluorescence resonance energy transfer. *Proceedings of the National Academy of Sciences*, 99(20):12669–12674, 2002.

[124] K. Takeda, D. Shao, M. Adler, P.G. Charest, W.F. Loomis, H. Levine, A. Groisman, W-J. Rappel, and R.A. Firtel. Incoherent feedforward control governs adaptation of activated Ras in a eukaryotic chemotaxis pathway. *Sci Signal*, 5(205):ra2, 2012.

[125] P. Takáč. Linearly stable subharmonic orbits in strongly monotone time-periodic dynamical systems. *Proceedings of the American Mathematical Society*, 115(3):691–698, 1992.

[126] D. W. Talmage. Allergy and immunology. *Annu. Rev. Med.*, 8:239–256, 1957.

[127] R. Thomas. On the relation between the logical structure of systems and their ability to generate multiple steady states or sustained oscillations. *Springer Ser. Synergetics*, 9:180–193, 1981.

[128] R. Thomas and R. D’ari. *Biological feedback*. CRC Press, Boca Raton, 1990.

[129] R. Thomas and M. Kaufman. Multistationarity, the basis of cell differentiation and memory. i. structural conditions of multistationarity and other nontrivial behavior. *Chaos*, 11:170–179, 2001.

[130] M. J. Tindall, S. L. Porter, P. K. Maini, G. Gaglia, and J. P. Armitage. Overview of mathematical approaches used to model bacterial chemotaxis I: the single cell. *Bull. Math. Biol.*, 70:1525–1569, 2008.

[131] A.P. Tran, M.A. Al-Radhawi, I. Kareva, J. Wu, D.J. Waxman, and E.D. Sontag. Delicate balances in cancer chemotherapy: Modeling immune recruitment and emergence of systemic drug resistance. *Frontiers in Immunology*, 11:1376–, 2020.

[132] N. Trendel, P. Kruger, S. Gaglione, J. Nguyen, J. Pettmann, E.D. Sontag, and O. Dushek. Perfect adaptation of CD8+ T cell responses to constant antigen input over a wide range of affinity is overcome by costimulation. *Science Signaling*, 14:eaay9363, 2021.

[133] J. Tyson and H.G. Othmer. The dynamics of feedback control circuits in biochemical pathways. *Progr. Theor. Biol.*, 5:1–60, 1978.

[134] U.S. Geological Survey. *Escherichia coli* bacteria. Image, accessed 2025-03-08.

- [135] K. J. Watts, A. Vaknin, C. Fuqua, and B. I. Kazmierczak. New twists and turns in bacterial locomotion and signal transduction. *Journal of Bacteriology*, 201(20):10.1128/jb.00439-19, 2019.
- [136] M. A. West and W. Heagy. Endotoxin tolerance: A review. *Crit. Care Med*, 30:S64–S73., 2002.
- [137] J. D. Wolchok, A. Hoos, S. O'Day, J. S. Weber, O. Hamid, C. Lebbé, M. Maio, M. Binder, O. Bohnsack, G. Nichol, R. Humphrey, and F. S. Hodi. Guidelines for the evaluation of immune therapy activity in solid tumors: immune-related response criteria. *Clinical Cancer Research*, 15(23):7412–7420, 2009.
- [138] J. Wu and D.J Waxman. Metronomic cyclophosphamide schedule-dependence of innate immune cell recruitment and tumor regression in an implanted glioma model. *Cancer Letters*, 353(2):272–280, 2014.
- [139] T. M. Yi, Y. Huang, M. I. Simon, and J. Doyle. Robust perfect adaptation in bacterial chemotaxis through integral feedback control. *Proc. Natl. Acad. Sci. U.S.A.*, 97:4649–4653, 2000.
- [140] X. Zhang, J. Zhang, P. Liu, J. Wang, K. Zhao, Z. Zhu, K. Gu, and W. Zhao. Immunotherapy progress and clinical strategy of unresectable locally advanced non-small cell lung cancer. *Frontiers in Oncology*, 13, 2023.